Characterisation and growth of polar MgO(111) thin films prepared by Molecular Beam Epitaxy

Daniel Jon Pingstone

PhD

University of York

Physics

August 2018

Abstract

Magnesium oxide MgO has developed research interest for its use in electronic and spin electronic device applications. Examples of these devices are power MOSFETs and spinFETs. Power MOSFET devices have been developed with silica gates on SiC substrates, however dielectric properties of silica and extreme operating and processing conditions of SiC based devices present problems with electrical properties of such devices. The dielectric properties of MgO make it an ideal replacement for silica in power MOSFET devices with Silicon Carbide. These properties in combination with high tunneling magneto resistances recorded for magnetic tunneling junctions using MgO suggest that MgO/SiC hetero-junctions could also be applicable to the field of semiconductor spintronics and spinFET devices.

The polar structure of MgO has been of research interest for many years. The aims of this work are to understand the electronic structure at the interface for prospective device applications and to understand the impact of the polar structure on MBE grown MgO(111) thin films.

The results presented in this work show successful growth of polar MgO(111) thin films prepared by MBE confirmed by analysis of the thin films using surface electron diffraction, XPS, TEM and STEM techniques. Preparation of flat 6h-SiC(0001) by hydrogen cleaning in UHV is demonstrated herein, resulting in a clean template for subsequent MgO(111) growth.

Successful growth of MgO(111) films as thin as a few nanometres has also been demonstrated. Structural characterisation of these films has been performed using RHEED and STEM and the electronic band alignment at the interface of MgO thin films with 6h-SiC(0001) has also been measured by XPS. This work also resolves discrepancies in the valence band offset reported in the literature, which have been clarified using STEM and CASTEP simulations.

Contents

List of Tables

List of Figures

Acknowledgements

I would like to thank my supervisors Dr Vlado Lazarov and Dr Steve Tear for their guidance and support throughout my PhD research. Without their belief in me I may not have reached this point. I am grateful for the opportunity to work with them both.

Further acknowledgment and thanks go to the research staff and postdocs that have helped me along on my PhD journey. I am grateful to Dr Andy Vick, Dr Barat Kuerbanjiang and Dave Coulthard for supporting me with maintaining the vacuum systems, Dr Leonardo Lari, Dr Jon Barnard and Ian Wright for maintaining the microscopes and assisting me with experiments. You were all a pleasure to work with and I learned a lot from each of you.

I would also like to thank the other PhD candidates that I have shared my journey with, particularly Dr Dan Gilks, Dr Arsham Ghasemi, Dr Zlatko Nedelkoski, Genadi Naydenov and Adam Kerrigan of RG Vlado, and Phillip Bentley and Jason Zhang for your enthusiasm and assistance. Furthermore I would like to thank the many friends that I have made during my PhD research and wish you all the best for the future.

Finally I would like to thank and dedicate this thesis to both my family and my partner Saskia, for their love and support. Without them who knows where I would be in life.

Author's Declaration

I declare that the work presented in this thesis is based purely on my own research, unless otherwise stated, and has not been previously submitted for a degree in this or any other university. All sources acknowledged as references.

Chapter 1

Introduction and Motivation

The development of high power electronics has seen a rise in research interest for wide band gap semiconductors such as SiC and GaN [1–4]. This has come about from the development of electric vehicles and electronics in extreme conditions i.e. sensors on oil drill heads and control of high voltage electronics. While developments have been made with native oxide SiO_x/SiC devices, SiO_x cannot reliably withstand processing and operating conditions of SiC devices, leading to leakage currents and electronic states available in the band gap at the SiO_x/SiC interface [5, 6].

This has lead to a call for novel oxide-semiconductor hetero-structures to develop high power electronics. Research has been conducted into crystalline thin film oxides but the lattice mismatch between the film and substrate can lead to strong strain induced electric fields at the interface, compromising device properties, again resulting in electronic states within the band gap at the interface.

Considering these factors, this thesis discusses the hetero-epitaxial system of MgO/SiC, with MgO as a candidate gate oxide material for power MOSFET applications. The high dielectric constant of MgO [7] and only 3% lattice mismatch with SiC are key indicators that the MgO/SiC hetero-structure is a promising material system for power electronics.

In addition, MgO is used as a crystalline tunneling barrier in magnetic recording media and as such, MgO has gained interest as a material for magnetic tunneling junctions in the developing field of spin-electronics (spintronics) [8, 9]. Therefore the MgO/SiC heterojunction may be applicable in spintronic devices.

1.1 A Brief History of Semiconductor Electronics

This section considers the modern applications of semiconductors in electronics from the development of the p-n junction and subsequently the bipolar transistor in the 1940's.

Russel Ohl's findings on doped Si systems, in what is known as the p-n junction, in 1940 [10] have been crucial for the development of LED's, photo-voltaics and solid-state rectifiers. Until that time, computers relied on bulky vacuum tubes for the binary switches. These were glass chambers, evacuated with an anode and cathode inside separated by a grid. Heating up the cathode with an electric current permits thermionic emission of electrons from the cathode to the anode through the vacuum. By charging the grid, the current flow can be stopped, therefore using the device as a binary switch.

The use of doped semiconductors drastically improved the scalability and energy consumption of computers using the bipolar transistor junction and started the modern age of computing. This was acknowledged when Schockley, Bardeen and Brattain won the 1956 Nobel Prize in Physics for their work in developing the bipolar transistor and transistor junction [11]. Within the same decade, the bipolar transistor was developed into integrated circuits, the progression of which has since been measured with Moore's Law, wherein the density of transistors doubles approximately every two years.

The pn-junction works by doping a semiconductor with acceptor atoms to provide holes, p-type, on one side and doping the semiconductor with donor atoms to provide electrons, n-type, on the other side. Where the two sides meet, creates a junction where a portion of the electrons and holes combine and neutralise the charge across the junction, creating a depletion layer. In forward bias, the electrons and holes are repelled by the external electric potential applied to the system and migrate towards the junction, reducing the depletion region to the point where the charges can conduct across the junction. In reverse bias, the charges are drawn away from the junction by the external electric potential, increasing the width of the depletion layer so that there is no conduction of charge across the interface.

The pn-junction started development of photo-voltaics from the ability to generate charge from light. Light with wavelength smaller than that of the band gap energy, incident on the depletion zone can create an electron-hole pair, wherein an

electron from the valence band is excited into the conduction band, leaving a positive charge, a hole, in the valence band. By broadening the depletion zone of the pn-junction in reverse bias operation, a larger area is created for light to interact with and generate more charge current. This is the principle behind photo-voltaic operation.

The bipolar junction transistor (BJT) is comprised of two pn-junctions, typically in a *npn* configuration as emitter, base and collector respectively. To control the transistor there are two junctions that are controlled by an emitter-base circuit and base-collector circuit. Similar to the pn junction, when no external electric potential is applied to the system then there is no continuity of charge through the structure due to the depletion layers at junctions j_1 and j_2, where j_1 and j_2 are the *np* and *pn* junctions within the bipolar transistor respectively. Biasing the whole structure will narrow the depletion layer at j_1 but widen the depletion layer at j_2 so by applying an electric potential at the base between the two junctions, the conductivity of the whole system can be controlled, allowing amplification and binary switching properties for which transistors are used.

Progress in the development of semiconductor electronics then brought about development of Field Effect Transistors (FET). The type of FET of interest in this thesis is the metal-oxide-semiconductor field effect transistor (MOSFET). The advantages of the MOSFET over the bipolar junction transistor are lower noise; due to the higher *off* resistance, better thermal stability and reduced power consumption, which has further improved the scalability of transistors because heat dissipation is less of a consideration with MOSFET integrated circuits than with BJT circuits.

The semiconductor based MOSFET was invented in 1959 at Bell Labs [12] although the principles behind the operation of a FET were originally patented by J.E. Lilienfeld in 1927 [13]. The MOSFET comprises source, gate and drain electrodes. For the n-type MOSFET (NMOS) the source is a highly doped n-type semiconductor region that is in contact with a lightly doped p-type region, on the opposite side of which is is another highly doped n-type semiconductor region for the drain, and vice versa for the p-type MOSFET (PMOS).

The gate is constructed from a metal electrode on top of an insulating dielectric material referred to from this point as the gate dielectric. By using Si as the doped semiconductor substrate, the native oxide SiO_2 has been used as a gate dielectric.

The purpose of the dielectric is to create a capacitor structure, called a metal-oxide-semiconductor (MOS) capacitor, that under bias will accumulate charge at the interface between the p-type region of the semiconductor and the gate dielectric. The charge accumulated becomes a channel for majority charge carriers, electrons in the NMOS case, to conduct from the source through the p-type region to the drain. When operated at saturation, the transistor behaves as a switch for logic circuitry, while operating below saturation generates amplification applications.

MOSFET technology in integrated circuits later improved with the introduction of complimentary metal oxide semiconductor (CMOS) technology, patented in 1967 by F. M. Wanlass [14]. This has become the standard technology for logic devices. CMOS uses two transistors in series, one NMOS type (n^+pn) and the other PMOS type (p^+np). In this configuration, one of the pair of transistors will always be off, requiring less energy as static power consumption will be reduced compared to all NMOS technology for example. Thus reducing heating effects in the device and the largest energy cost will only come when switching.

Fabrication of devices using the CMOS configuration has been extremely successful, through which the transistor density has increased with Moore's Law, however in the last two decades the miniaturisation of the SiO_2 gated MOSFET has reached operational limits. Geometric alterations were made to the MOSFET design and the FinFET or double-gate transistor design was adopted along with changes to the gate dielectric material in favour of $HfSi_xO_y$ and $Ta2O_5$ [15–17]. Now drastic changes to device structures are required for the progression of CMOS technology below 10nm gate widths. [1]

[1] At the time of writing this thesis, production of 10nm gate width technology has been achieved in commercial devices.

1.2 MOSFETs for Power and Spin Electronics

Moving forward, the application of the MOSFET to power electronics and spin electronics, referred to from herein as spintronics, has developed research interest from industry into high-κ dielectrics for power electronics and semiconductor spintronics. SiC and GaN are examples of wide band gap semiconductors that have gathered research interest for power electronic applications.

A power MOSFET has a different structure to the MOSFET design in logic devices but the operating principles are similar. Figure 1.1 describes the structure of the power MOSFET. In order to operate reliably at high output voltages, the source and drain are positioned on opposite sides of the device. The source is then connected to a n^+ doped emitter region inside a p-type doped body or base region. This p-type region separates the source from an n^- doped collector region also known as the drift layer. The drain is then connected to the device by another n^+ doped region connected to the drift layer. Doping concentration in the drift layer is important for resistance of the collector region that is responsible for the switching characteristics and voltage handling capacity of the device [18, 19].

The principle switching operation of the power FET is the same as that of transistors used in CMOS logic technologies, where a potential is applied across the source and drain, termed the the output voltage, but no current can pass through the transistor until a channel is created by applying a voltage between the gate and source to create an inversion region wherein a channel is induced for charge to conduct between the n^+ and n^- regions.

The power MOSFET has the advantage of higher switching speeds and improved efficiency at lower voltages. Si based power FETs are capable of switching up to $\approx$100,000 Hz, however devices utilising wide band gap semiconductors could achieve switching speeds of over 1MHz. This makes the MOSFET an excellent choice for applications such as electronic speed controllers, for use with electric motors, rectifiers and step down converters.

Si power MOSFET devices suffer from conduction losses due to high on-state resistances that, coupled with the high voltages and currents being controlled and converted, lead to heating, making devices inefficient, limiting MOSFET applications to 600V [20]. As a result, wide band gap semiconductors are being employed to improve power MOSFET devices. A material of particular interest for such applications

is SiC. Manufacture and processing of synthetic SiC has improved in quality in order to remove defects such as micropipe dislocations. SiC has lower intrinsic charge carrier concentration but higher electric breakdown field, higher thermal conductivity and larger saturated electron drift velocity than Si, however p-type doping SiC is difficult and hole mobility is lower than in Si, therefore SiC has not been adopted into CMOS technology. The band gap energy of the 4h- and 6h-SiC polytypes is 3.0 eV. This larger band gap energy and higher thermal conductivity means that SiC devices can operate at higher temperatures and at higher switching frequencies.

SiC has over 250 polytypes but there are two types of interest for wide band gap semiconductor devices. These are 4h-SiC and 6h-SiC polytypes. The latter has a stacking sequence along the c-axis of the wurtzite crystal structure presented in figure 1.2. The entire c-axis unit cell height is 15Å and for any miscut angle of a 6h-SiC wafer, steps form with step height of one c-axis length. 4h-SiC has generated more interest than 4h- because has higher electron and hole mobilities than 6h- [21], however there a more steps for an equivalent miscut angle on 4h- than on 6h-SiC, potentially resulting in larger defect densities in thin films prepared on 4h-SiC. Such

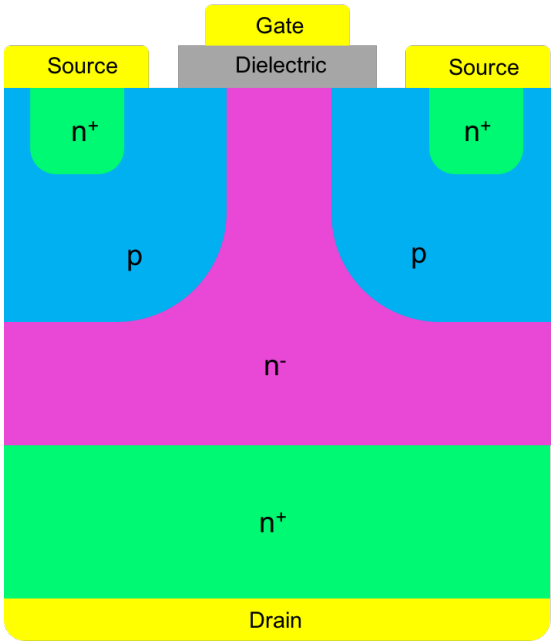

Figure 1.1: A schematic of the power MOSFET device structure. The n^+-type emitter and p-type base region are shorted in order to negate the effect of the parasitic bipolar transistor across the npn regions. Doping in the n^--type collector region dictates switching characteristics and voltage handling capacity of a device.

defect may contribute to unwanted energy states within the energy band gap.

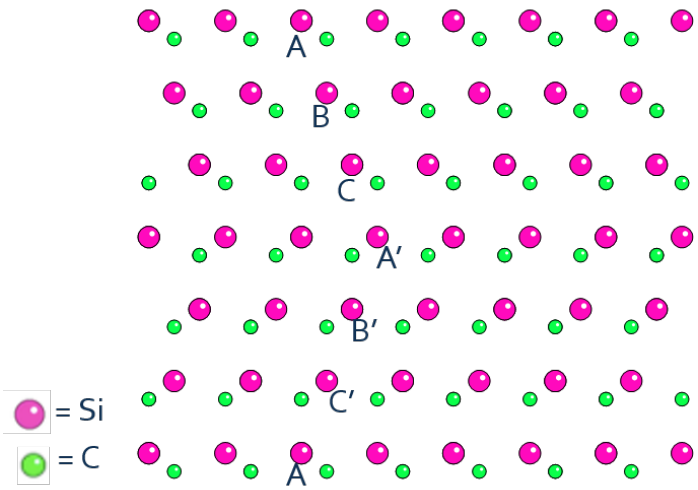

Figure 1.2: A model of the 6h-SiC stacking sequence. The sequence is labelled ABCA'B'C'A changing the angle of stacking every 3 planes of SiC pairs. The atoms stacking sequence is formed along the (0001) crystallographic direction. Si atoms in the model are pink, whereas C atoms in the model are green

SiC devices have been developed using SiO_x gated FETs. The SiO_x gate can be developed natively on SiC just as it can on Si, however for controlling high voltages and currents SiO_x does not perform well as a dielectric material and is the weak point for electric breakdown in devices [5]. This has created research interest into materials with improved dielectric properties [22, 23] but the material requires low lattice mismatch with SiC in order to alleviate strain induced electric fields and defects at the interface between crystalline materials.

The search for a material with high dielectric constant and epitaxial compatibility with SiC has found that MgO would be a suitable oxide for a gate dielectric to replace SiO_x. MgO is an insulator with a band gap energy of 7.8eV has a dielectric constant of $\approx$10, which is greater than that of SiO_2 at 3.8, and MgO has low lattice mismatch with SiC at just 3% for the MgO(111)/SiC(0001) interface. The advantage of using a material with improved dielectric properties is that the material has a higher breakdown voltage for the same thickness. This is important for power transistors where high switching frequencies and output voltages can breakdown across the gate. Although the power FET is used for applications up to around 200V, with a high-κ gate dielectric on a wide band gap semiconductor base this could be increased to kV potentials.

MgO is also used as an effective tunneling barrier, particularly in magnetic recording and in the novel research field of spintronics [24, 25]. An example of MgO in spintronics is a variation of a spin valve, known as a magnetic tunnelling junction (MTJ) described in figure 1.3a where a $\leq$2nm thin MgO barrier separates two ferromagnetic (FM) materials, which are capable of polarising the spin of electrons in the d-orbitals of atoms in the material. Polarisation of a FM material is governed by Hund's rule that states that electrons will occupy all orbitals singly before adding further electrons as pairs in atomic orbitals, and the electrons in the singly occupied orbitals will have the same spin quantum number s, either all $s = \frac{1}{2}$ or all $s = -\frac{1}{2}$ [26].

The use of MgO improves the spin filtering by several orders of magnitude over non-magnetic barriers and other oxide barriers [27–30]. Operation of the spin valve requires that the magnetisation of one of the FM layers be fixed by an adjacent pinning anti-ferromagnetic layer; a pinned layer, while the other can have the magnetisation direction changed; a free layer. This introduces the phenomenon of Tunneling Magneto-Resistance (TMR). When the MgO layer is sufficiently thin, when the two FM layers have their magnetisation parallel to each other then when a bias is applied across the system, electrons can tunnel across the barrier and the resistance of the system drops. However, if the magnetisation directions are anti-parallel then the spin quantum number of the electrons will be opposite in each layer and tunneling cannot occur. This increases the resistance of the system. This spin orientation dependent resistance is known as Magneto-Resistance. Hence the spin-valve acts as a switch but because the response in resistance is so high and the current flow is very low, the energy consumption and losses in a spin valve are low making spin-valves more energy efficient than saturated transistor switches.

This is one area of motivation behind spintronic device research. The other aspect of spintronics that is of interest is the dual control of electric current and spin current with a single device structure. The spinFET is designed to control both the flow of both charge and spin current through a transistor independently. As a single channel device, controlling spin current is more energy efficient than charge current. How the spin current conducts through the device brings forward the research area semiconductor spintronics. For successful development of the spinFET, spin transport in semiconductors needs to be efficient enough to influence and detect the spin signal. The scattering of electrons in a semiconductor reduces the spin polarisation and as a

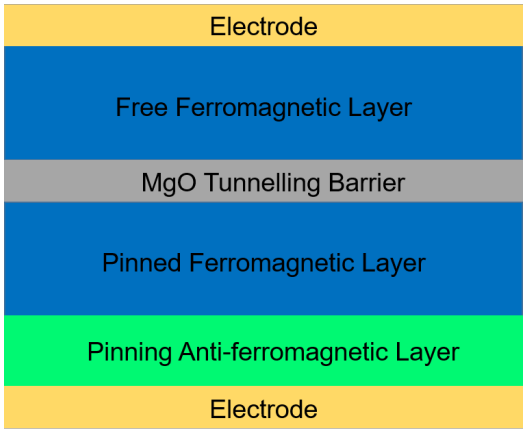

(a)

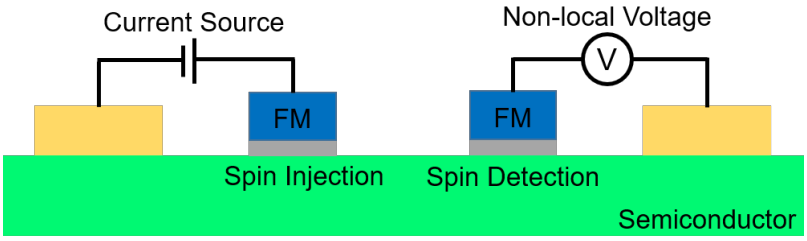

(b)

Figure 1.3: (a) Schematic of a magnetic tunneling junction (MTJ) spin valve device. When the magnetisation vectors of the ferromagnetic layers are aligned parallel, tunnelling across the barrier is allowed and voltage applied across the MTJ drops, whereas when the magnetisation vectors of the ferromagnetic layers are anti-parallel a large increase in voltage is observed due to tunnelling magneto resistance (TMR). An anti-ferromagnetic layer exists to pin the adjacent ferromagnetic layer [30, 31]. (b) Schematic of a circuit for measuring non-local voltage genreated from spin polarised current, known as the Hanle Four Probe measurement setup. A source of current applied to a ferromagnetic (FM) electrode that spin polarises the current injected into a semiconductor. A further ferromagnetic electrode is used to detect the spin polarised current.[32].

result semiconductors have short spin diffusion lengths at room temperature, however reports show that for spin transport in Si the spin diffusion length is $\approx 2\mu$m [33].

A long spin diffusion length, on the scale of source to drain distances, is required to maintain spin polarisation during operation of a device. The spinFET creates a solution for controlling multiple channels in the same transistor. By using spin polarised contacts with a traditional MOSFET design, both charge current and electron

spin orientation can be manipulated to provide switching and amplification to modern integrated circuits. By applying an electric field across the gate oxide a charge channel can be created to enable charge to pass between the source and drain. This electric field is also capable of causing the electron spins to precess and ultimately oppose their initial orientation entirely. Where the spin polarised contacts are aligned and the electric field at the gate creates a channel for electrons to conduct through the device, should the electron spins be anti-parallel in orientation to the magnetisation of the spin polarised contact at the drain then a large resistance will be measured, as described in the case of the spin valve. Similarly if the electron spins are aligned parallel with the magnetisation of the spin polarised contact then the resistance will be low. In these cases the observed voltage will be high and low respectively. The degree of precession of the electron spins will define the magnitude of the resistance, yielding transistor amplification properties. By using a tunneling barrier on the contacts, the magneto-resistance is enhanced therefore the current required for switching will be significantly reduced. Reduction in energy usage is one of the key aims of spintronics.

Research interest in spin injection into semiconductors has developed for the application of spinFETs. While polarising the spin of electrons in a ferromagnet and finding materials with long spin diffusion lengths may be straight forward, the realisation of injecting spin polarised current across an interface becomes difficult because of electrical conductivity mismatch. The conductivity mismatch and interface band structure result in a reduction in the spin polarisation of electrons conducting from the FM layer into the semiconductor. An alternative approach is to use a tunneling barrier, such as MgO, to isolate the FM and semiconductor removing the issue of conductivity mismatch. Therefore the MgO/SiC system studied in this work could be an example of a hetero-structure for use in future spinFET devices.

1.3 Dielectric Stability of MgO

Control of the electric field at the transistor gate in aforementioned devices is particularly important and therefore materials with impressive dielectric properties are desirable for this application. MgO has a large dielectric constant of $\kappa \approx 10$ [34] and can sustain voltages up to 12 MV/cm before electric breakdown occurs, which is a significant improvement over prior gate dielectric materials [35, 36].

Thin films of MgO deposited on various substrates by various techniques have shown close to bulk like dielectric properties . Epitaxial MgO deposition methods in the literature comprise Magnetron sputtering [8, 28, 37], Pulsed Laser Deposition (PLD) [38–40] and Molecular Beam Epitaxial (MBE) growth [41, 42]. The advantages of these techniques are discussed briefly in chapter 2.1. MBE growth has been chosen for production of MgO thin films in this project due to the large number of parameters that can be changed to optimise the growth and alter the growth mode (see figure 7). Dielectric properties of thin films are sensitive to defects in the crystal structure and strain at the interface between the thin film and substrate and in the case of the project material system, electric polarisation in thin films contributes to the dielectric properties measured.

For a dielectric material to succeed in an electronic device it must be stable over the lifetime of the device. This means that the crystal structure and dielectric properties should not degrade over the lifetime of the device. Degradation of MgO thin films is described in the literature, wherein the films are susceptible to adsorption of water vapour and oxidation of the substrate at the interface [43]. However in modern multilayer devices exposure of the dielectric layer to the atmosphere is mitigated by electrodes that cap and protect the dielectric layer. This is discussed in more detail in chapter 7. Furthermore the interface between the dielectric film and the substrate should have a low interface mid gap state density, typically less than 10^{11} eV^{-1} cm^{-2} carrier trap density.

1.4 Polarisation in thin film oxides

Electric polarisation in materials is common however the magnitude of polarisation may not have a significant contribution to the properties of the system. Applied examples of magnetic polarisation have already been discussed with regards to spintronics and this section provides details on the physical principles of electric polarisation in and across hetero-junctions. Whenever two materials are bonded together or there is a termination of a crystal structure from its bulk atomic configuration, a distribution of the charge between the systems involved is required. This is observed in surface reconstructions and interface band alignments that attempt to minimise the electric dipole from the termination of each crystal structure.

Starting with the case of bulk crystal termination, by cleaving the bulk structure of a crystal the electrons associated with bonding between atoms are no longer bound and as a result these electrons contribute to a surface charge density and create a electric dipole between the bulk crystal and the surface. This is described as the frozen bulk termination where dangling bonds remain at the surface. In reality these dangling bonds would be saturated by atoms and molecules from the atmosphere or where energetically favourable, the surface atoms can rearrange to reduce the number of dangling bonds remaining on the surface, redistributing the charge within the crystal to minimise the surface electric dipole and therefore minimise the potential energy of the surface. By working in Ultra High Vacuum (UHV) conditions with surfaces, contamination of surfaces is limited, establishing conditions to prepare specific surface reconstructions, providing the best template on which to prepare thin films. A frozen bulk description of the system can be extended to ionic crystals such as metal oxides. For example, the rock-salt structure of MgO is constructed from the exchange of electrons between anions and cations. The Oxygen anions complete the condition for nobility of the oxygen electron configuration by acquiring a negative charge that is equivalent to -2e, where e is the magnitude of the charge of an electron, that will be referred to from this point as σ^- so that the description can be applied to ionic structures generally. Magnesium cations achieve nobility of the electron configuration by donating electrons to the neighbouring anions. As a result, the charge associated with the cations is equal and opposite to the charge allocated to the anions. The cation charge will therefore be referred to as σ^+ for the discussion of ionic structures generally.

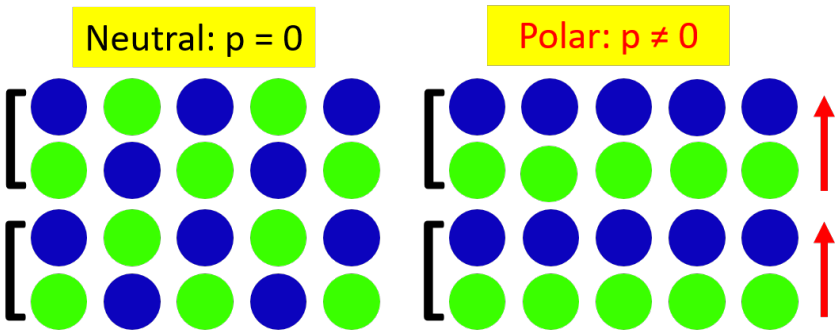

Figure 1.4: Schematics of ion arrangements when viewed along projection of different crystal orientations. Within the grouped plane pairs, for the neutral cell, the position of the ions means that the net surface charge density per plane is zero. However the arrangement of ions in the polar structure shows that alternating anion cation plane pairs are formed, producing a non zero dipole moment oriented as described by the arrow.

By considering the interaction between anions and cations in a crystal, it becomes apparent that electric dipoles form between ion pairs. Extending this to cover the ionic structure on the bulk scale results in electric dipoles between anion and cation planes. Figure 1.4 shows two of the three unit cell categories of both polar and non-polar structures described by Tasker [44], illustrating how the orientation of a unit cell can bring about electric polarisation. Charge neutrality states that for a surface termination to exist, the net dipole moment across the unit cell must be zero. However when considering the ionic rock-salt unit cell the condition for a non-zero dipole moment can be established. This problem extends through the crystal structure producing ionic planes with alternating surface charge density, analogous to an array of capacitor plates, described in figure 1.5. The charts below the plate array in this figure indicate how the electric field and electric potential behave as the number of charged planes increases. As the number of alternating charged plane pairs increases, described by 1.5 (a), the surface potential increases proportionally due to the alternating electrostatic potential, governed by $E=\frac{\sigma}{\epsilon_0}$ for an electric field, E due to surface charge density σ. This diverging electrostatic potential with increasing N anion-cation planes is know as the polar catastrophe and stipulates that polar surfaces are not energetically favourable. The stacking of alternating anion-cation planes is observed in rock-salt structured ionic crystals where the normal plane direction is along <111>. Divergence of the electrostatic potential from the polar structure can be written as equation 1.1

$$V = \frac{N\sigma R}{\epsilon_0} \tag{1.1}$$

where V is the electrostatic potential that accumulates across N planes each of surface charge density σ separated by a distance R and ϵ_0 is the permittivity of free space [45–50].

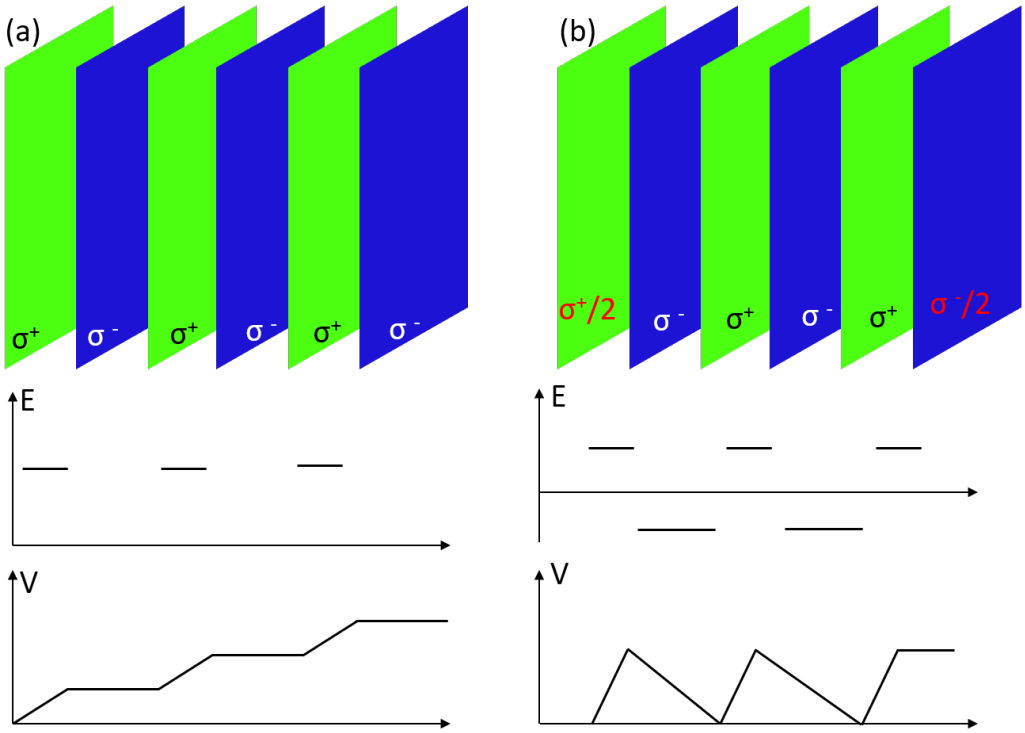

Figure 1.5: A figure describing the analogy of a capacitor plate model with anion-cation plane stacking in an ionic crystal. (a) A schematic with graphs indicating the electric field, E and the electrostatic potential, V as ionic planes are added. (b) A schematic with graphs of the predicted behaviour when modifications to the surface charge density of the primary and ultimate planes in the ionic plane array are made. The reduction in surface charge density of the outermost layers shifts the electric field starting point and enables a finite electrostatic potential to be maintained with increasing thickness. Please note that scales of the graphs are not relative to each other and are purely conceptual.

The schematic of the anion-cation plane stacking in figure 1.5 (b) shows modification to the surface charge density of the outermost ionic planes. This modification reduces the initial surface charge density, whereof the addition of alternating charged planes establishes a finite, non-diverging dipole moment, described by the shape of the electrostatic potential, V, for the model system (b). A similar result can be obtained

by modifying the distance between anion-cation plane pairs however in reality this would not occur for structures more than a few layers in thickness. The modification of surface charge density of terminating bulk planes is seen on many material surfaces through chemical adsorption and reconstructions of the crystal structure at the surface, however the electric dipole contribution adds complexity. Two key examples of compensation mechanisms for polar surfaces of rock-salt ionic structures are the octo-polar reconstruction and adsorption of hydroxyl groups. Rather inconveniently for the reader, the origins and physics of surface reconstructions are discussed in more detail in chapter 6.

The octo-polar reconstruction, also referred to as the (2x2) reconstruction, as written in Wood notation form [51], consists of a modification to the atomic structure of the top two surface layers, where the top layer contains one atom for every three in the layer beneath it. This modifies the surface charge density to become $\sigma^+/4$ on the surface layer and $3\sigma^-/4$ on the layer beneath, where the anions and cations of the two layers can also be oppositely charged. As described in figure 1.5 (b), for the octo-polar reconstruction the surface charge density is modified establishing a finite, non-diverging electrostatic potential except in this case the the surface charge density of multiple outer layers is modified. This surface reconstruction is observed for polar rock salt FCC structures such as NiO and may also be described as a type of nano-facet reconstruction [52–56].

While the octo-polar reconstruction is one reconstruction for reducing the energy of a polar surface, exposure to an atmosphere of atoms and molecules provides a plurality of other mechanisms for compensating the surface energy due to the electric dipole of the polar structure. Adsorption of water vapour and oxidation of metals is not a novel research area however research interest into stability of polar surfaces from adsorption of hydroxyl groups has increased within the last two decades. The development of oxide electronics is the motivation for understanding the stabilisation mechanisms within polar oxide structures and thanks to modern electron energy analysers, the energy resolution achievable with spectroscopy techniques such as X-ray Photo-electron Spectroscopy has developed research into bonding states at surfaces and interfaces. More on this is discussed in chapter 3.

The adsorption of hydrogen atoms and hydroxyl molecules establishes the condition for stabilising the divergent electrostatic potential of the polar structure to a finite surface potential by modifying the surface charge density of the outer most

plane to $\sigma/2$. Since water vapour is abundant within the atmosphere this is a common stabilisation mechanism that has been observed for the compensation of electric polarisation on both bulk polar surfaces and polar thin films [56–59]. The proposed benefit of adsorbing hydrogen to stabilise the surface is that an effective (1x1) surface is formed without reconstruction that would allow for flat multilayer growth of polar thin films for example in oxide electronic devices. This surface is also reported in literature arguing that the surface energy of the (1x1)-<111> hydroxyl surface is less than that of the non polar <100> [60].

While this compensation mechanism provides stability for polar surfaces of bulk samples and unsupported thin films, the compensation of the dipole moment for polar surfaces of supported thin films adds complexity because there is a contribution to the polarisation of the system from the interface dipole. This is known as induced polarity. Whenever materials are interfaced together to form a hetero-structure, there is charge transfer across the interface and the surface dipole of the substrate meets the surface dipole of the film creating the interface dipole. This charge transfer exists to equilibrate the Fermi level across the interface. Band bending occurs where the conduction bands and valence bands of each material meet. The electric charge associated with the band bending across the interface reduces the interface dipole by reducing the potential gradient of the valence and conduction band across the interface. Aptly, it is an aim of this work to understand the impact of the polar structure on the interface band structure.

MgO thin films supported on substrates in the literature provide a base to start the discussion of supported polar thin films [59, 61, 62], with a focus on irreducible oxides, applicable to MgO. Two conditions to consider for polar thin films are the thin regime and the thick regime. As already discussed, classically the magnitude of polarisation in these structures is dependent on the number of polar planes that make up the film. The properties of the electronic structure in these films can therefore be discussed for the regime of 1-10 polar MgO layers and another regime for thicker films comprising more than 10 polar MgO layers. Both theoretical predictions and experimental films have shown that for the thin regime polar MgO films exhibit metallic properties on metal and semiconducting substrates [59, 62, 63]. This is because the interface of the polar film with the substrate induces strain and a reservoir of charge is available that changes the local electrostatic potential at the interface, resulting in a change of the film structure from a rocksalt bulk structure to a graphitic structure with out of plane rumpling [46]. The properties of these ultra-thin films

are therefore sensitive to the preparation conditions and the substrate used. As the polar film thickness increases, the induced polarisation due to the interface with the substrate is less significant when compared to the ionic structure of the polar thin film and the electronic structure of the film becomes that of an insulator, as expected for MgO. The compensation mechanism for polar films in the thicker regime follows closely to that of the bulk surfaces, which is discussed further in chapters 7 and 8.

While the literature cited describes the physics of electric polarisation in thin films and on semi-infinite surfaces, the work presented in this thesis continues on from this to describe the physics of the growth of polar MgO thin films from analysis of experimental results and theoretical calculations.

1.5 Band alignment at oxide-semiconductor interfaces

In order to consider a prototype hetero-junction for electronic device applications, such as those described in sections 1.2 and 1.3, the electronic structure at the interface between materials in a junction must be understood. The electronic structure described herein is the band alignment, which is a measure of the energy differences between the conduction and valence bands across an interface between different materials. In the case of the MgO/SiC interface, the hetero-junction is formed between an insulating oxide and a semiconductor. This section aims to explain the physics associated with band alignment and the consequences of different types of band alignment. Band alignment measurements and predictions have been used for decades to determine the electronic properties of material junctions and such research has had a significant impact on the development of electronic devices such as Schottky diodes [64, 65], hetero-bipolar transistors [66, 67] and field effect transistors [68, 69] to name a few examples from a plethora of electronic devices available today.

The simplest description of interface band alignment comes from the comparison of two different metals in contact with each other. Upon contact, charge transfer at the interface occurs to equilibrate Fermi levels across the interface. Normally charge transfer would create space-charge resulting in an interface dipole, as discussed for the polar thin film interfaces, however because there are so many conduction electrons in a metal, the charge from these electrons screens the dipole from the charge transfer. A simple schematic of the metal-metal interface is provided in figure 1.6a. Once the Fermi level is equalised across the interface, an energy barrier in the conduction band then forms from the difference in work function of the two metals. This is is a very simple approach to predicting the interface energy band alignment and does not consider chemical bonds, terminating surfaces and reconstructions, interfacial strain and contaminants that may exist in real hetero-junctions. However it serves as a base to establish a model that can be applied to other material junctions.

Firstly, applying this simple model to the metal-semiconductor junction the requirement still exists to equalise the Fermi level under thermal equilibrium and that no current can flow when in this unbiased state. Figure 1.6b describes the interface between a typical metal and semiconductor, ignoring doping concentrations and bonding as per the model above. There are two energies to consider and these are the work function of the metal and the electron affinity of the semiconductor.

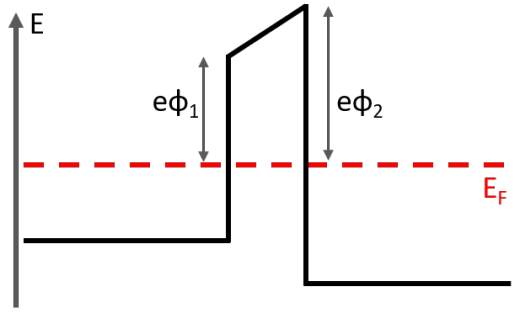

(a) An energy band diagram for a metal-metal interface, showing equalisation of the Fermi level under thermal equilibrium and the creation of a contact potential from the difference in the metal work functions [70].

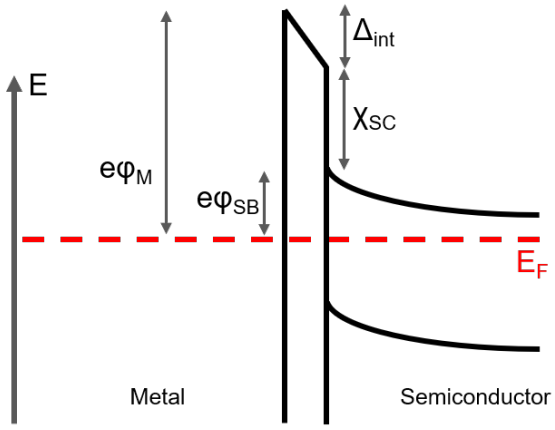

(b) An energy band diagram for the interface between a metal and a semiconductor. The central strip describes the energy barrier. In reality this barrier exists across a few Angstroms of the interface. The Schottky barrier $e\psi_{SB}$, is predicted from the differences in the metal work function $e\psi_M$, the electron affinity of the semiconductor χ_{SC} and the interface dipole Δ_{int} when the Fermi levels are equalised and the system is in thermal equilibrium [70]

Figure 1.6: Example energy band diagrams for metal-metal and semiconductor-metal interfaces.

Upon equalising the Fermi level across the interface an energy barrier is formed, the magnitude of which is dependent on the work function of the metal, the electron affinity of the semiconductor and the interface dipole. These are labelled in figure 1.6b wherein the energy barrier of the conduction band of a metal semiconductor interface is known as the Schottky barrier height. It is this barrier that has brought about devices such as the Schottky diode, wherein biasing and thus raising the Fermi level of the semiconductor promotes conduction electrons from the semiconductor conduction band into the metal, while preventing current flow when under reverse bias, characteristic of a diode [70]. Again, there are problems with this model due to the omitted contribution of chemical bonding, doping, interfacial mid gap states and strain fields however the contribution of an interface dipole is included in figure 1.6b. The significance of the interface dipole is of much debate because screening effects of the charge present in the metal due to conduction electrons can reduce the interface dipole, in theory. The band bending observed at the interface is due to the creation of space-charge. This space-charge is formed due to the exchange of charge across an interface when the Fermi levels are aligned and extends hundreds of Angstroms

across the interface. For a metal-semiconductor interface, the direction of charge transfer and therefore the magnitude of band bending, depends on the doping in the semiconductor, that affects the position of the Fermi level within the band gap, and the work function of the metal.

Now the core concepts of band alignment have been established they can be applied to semiconductor-semiconductor and insulator-semiconductor interfaces, where the latter will be described as oxide-semiconductor interfaces for reference to the MgO/SiC system. The semiconductor-semiconductor interface band alignment model in figure 1.7 follows Anderson's rule [71]. This rule stipulates that the conduction band offset ΔE_c is equal to the difference in the electron affinities of the two semiconductors. From this difference a valence band offset can subsequently be determined using the band gap of each semiconductor. The valence band offset is a standard used for determining electronic properties at the interface and ultimately indicates the type of band alignment. This model of Anderson's rule is a simplified model that does not consider; doping in either semiconductor, interfacial strain, chemical bonding, interface dipoles induced from space-charge and induced mid gap states. The significance of these is considered and accounted for in the discussion of valence band offset measurements in chapters 3 and 8. Improvements in predictions have been made over predictions based Anderson's rule. The common anion rule has developed to be in line with calculations used today for valence band offset measurements and predictions, described in equation 8.1 in chapter 3. The common anion rule states that for interfaced materials sharing a common anion, the valence band offset will be zero [72, 73].

The common anion rule accounts for bonding at the interface, an aspect that Anderson's rule fails to consider, and tight binding models in the literature [74, 75] describe p-orbital bonding states as important for calculating valence band offsets because the anionic p-states contribute to the wave function and subsequently the energy position of the valence band maximum. Further theory in the literature also accounts for the zero band offset consequence of the common anion rule arguing that spin-orbit splitting interactions between atomic orbitals need to be considered across the interface [76, 77].

Extending this basic model to oxide-semiconductor (insulator-semiconductor) interfaces, the main difference is that one of the materials has a much larger band gap than the other. This enables various degrees of overlap of the valence and conduction bands between the materials, resulting in three possible types of band alignment.

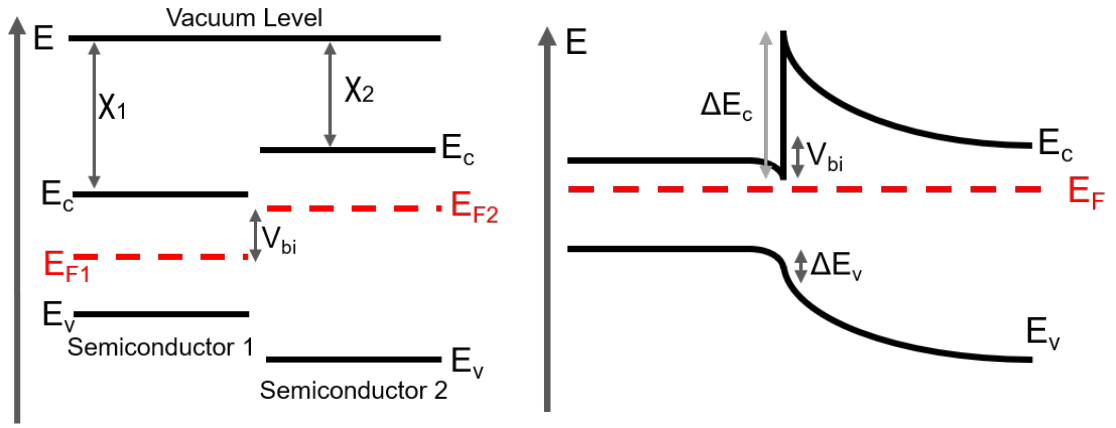

Figure 1.7: (a) An energy band diagram describing the positions of valence and conduction bands E_v and E_c respectively when the two semiconductors are not in contact. The energy position of the bands in this example follows Anderson's rule the the built in potential V_{bi} is determined from the difference in electron affinities χ_1 and χ_2. (b) An energy band diagram describing the positions of valence and conduction bands E_v and E_c respectively when the two semiconductors are in contact. Charge transfer across the interface creates space-charge that establishes band bending. Properties of the semiconductor-semiconductor interface include the built in potential V_{bi} and conduction band and valence band offsets ΔE_c and ΔE_v respectively [71].

These are described in figure 1.8 [78]. For MOSFET devices type I band alignment is required for the conduction of both electrons and holes while type-II and type-II band alignments are required for devices such as diodes. Figure 1.8 also shows why type-I band alignment is necessary for MOSFET devices. As discussed earlier in this chapter, conduction of charge is enabled by creating a channel of charge to enable conduction of charge carriers from the source to the drain of a transistor. Both electrons and holes require energy to overcome energy barriers in type-I band alignment, which means that when creating the channel, charge transport across the gate is mitigated. If type-II or type-III junctions form at the interface between the gate and base, charge leakage of one carrier type may occur.

The significance of space-charge is greater for semiconductor-semiconductor interfaces than metal-semiconductor interfaces, and the resultant interface dipole is enhanced due to minimal screening from conduction electrons in either side. This will of course depend on chemical bonding between the materials as well as doping concentration in the semiconductor and, particularly applicable to oxides, oxygen vacancies at the interface contributing to mid gap interface states that establish pin-

ning of the energy position of the Fermi level [77]. Fermi level pinning from mid-gap states was first predicted by Heine [79]. When considering polar oxide semiconductor band alignment reports in the literature predict that the density of interface mid-gap states is reduced for strongly polar bonded materials [77, 80]. This reduction in mid gap states also reduces tunneling through barriers at the interface, increasing barrier stability for polar bonded interfaces, the MgO(111)/SiC(0001) interface being such an example.

Extending on the literature and models described above, polar hetero-structures require models to be extended to potentials due to built-in polarisation when considering predictions for the valence band offset of such hetero-junctions. The difficulties of predicting valence band offsets are discussed briefly in chapter 8.

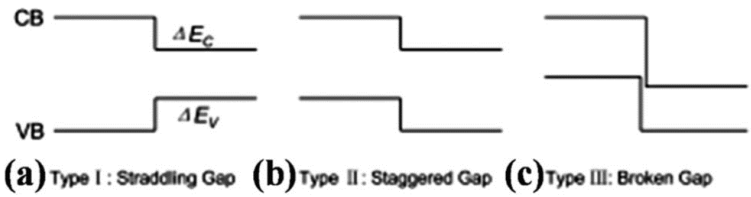

Figure 1.8: (a) An energy band schematic of a type-I band alignment where the conduction band energy position CB and the valence band energy level position VB of one semiconductor or insulator is positioned within the band gap of another semiconductor or insulator. The energy difference between conduction bands and valence bands across the interface is termed ΔE_c and ΔE_v respectively (b) A further energy band schematic of a type-II band alignment wherein the energy position of the conduction and valence bands of one semiconductor or insulator are both slightly higher than that of another semiconductor. (c) A further energy band schematic extending on type-II band alignment to the point where the band gaps of the two semiconducting or insulating materials no longer overlap [78, 81].

1.6 Overview of the thesis

Beyond this introduction, this thesis presents details on the experimental methods used and results obtained on the preparation of polar MgO thin films and the properties of MgO(111)/SiC(0001) hetero-structures. The chapters are summarised as follows.

Chapter 2 details the growth system setup comprising ultra high vacuum (UHV) equipment, material deposition and gas sources and in situ surface electron diffraction

methods and apparatus. A description of the Molecular Beam Epitaxial growth (MBE) system is included, along with physics of how each component in the system works to provide some understanding on the role each components has in thin film growth and analysis.

Chapter 3 describes the physical principles and apparatus used in X-ray Photoelectron Spectroscopy (XPS). This technique is used to measure the valence band offsets of the MgO/SiC interfaces reported in chapter 8. Details on physical principles and measurement apparatus include descriptions of X-ray generation, Photoelectron generation in the sample, and collection of photoelectrons in an analyser.

Chapter 4 describes the physics of electron optics in Transmission Electron Microscopy (TEM). Details of microscope components, sample preparation and image simulation and analysis are included to support analysis of results reported in subsequent chapters.

Chapter 6 describes preparation of SiC(0001) surfaces. There are in-situ and ex-situ methods involved in preparing substrate surfaces, in UHV conditions and controlled atmospheric conditions respectively. The advantages and disadvantages of these are compared and results from literature are discussed alongside experimental results of the SiC substrate surfaces prepared for subsequent MgO deposition. Reflective High Energy Electron Diffraction has been used to identify the surface reconstructions of the SiC(0001) substrate surface.

Chapter 7 presents the MgO growth conditions for both thin and thick films and the results of varying temperature and oxygen concentration. Preparation conditions reported in the literature are considered and compared to those used to prepare thin films analysed for this thesis. Reflective High Energy Electron Diffraction, Low Energy Electron Diffraction and Transmission Electron Microscopy have been used to analyse the MgO films grown under different oxygen and temperature conditions.

Chapter 8 reports valence band offset measurements for MgO/SiC hetero-structures. Results from literature are discussed and the results obtained experimentally clarify inconsistencies in the literature. X-ray Photoelectron Spectroscopy and Scanning Transmission Electron Microscopy are used to determine the energy position of atomic orbital states across the interface and determine the structure at the interface respectively. The experimental results obtained are supported using calculations based on theory. The theoretical methods include CASTEP density functional theory and QSTEM image simulations.

Finally chapter 9 summarises the work completed for this thesis and indicates potential future work related to this research.

Chapter 2

Techniques of thin film growth

This section aims to provide the reader with information on the experimental methods and apparatus used to obtain the results presented in this thesis. This also acts as a guide to the processes of thin film preparation and analysis. This section details the main apparatus and methods used however results from other experimental techniques may also be presented in further chapters.

2.1 Ultra High Vacuum Setup

In order to prepare atomically flat surfaces and thin films, contaminants need to be removed from the system by pumping the system down to ultra-high vacuum. Ultra-high vacuum is defined as the vacuum pressure range of 10^{-9} - 10^{-11} mbar. Whilst higher vacuum (lower pressure) is achievable, sustaining it is difficult when using the system for preparing films with gases on various substrates.

The main components for establishing high vacuum are the roughing pump and turbo molecular pump, which in combination establish vacuum of 10^{-7} mbar. The roughing pump establishes low to medium vacuum at round 10^{-3} mbar. An example of which is a rotary pump which uses an eccentrically rotating piston to pull molecules out of the system, compress them and push them through the exhaust. Most rotary pumps are oil lubricated however this oil can be pulled by vacuum pressure into the system. This can damage components for the system and as a result molecular sieves are employed between oil based rotary pumps and the system.

For increased efficiency and reduced backing line contamination a scroll pump can be used instead. This uses two spiraled scrolls, which rotate eccentrically to

allow inlet, compression and exhaust. A rotary or scroll type pump must establish low vacuum to back the turbomolecular pump.

The turbomolecular pump achieves pumping by spinning a series of blades oriented to push molecules by ballistic transport rather than pressure differentials at higher vacuum. This is due to the free molecular flow possible at higher vacuum, where the mean free path of the molecules in the system is much greater than the pipe bore of the vacuum chamber [82, 83]. To prevent molecules from leaking back into the pump, the exhaust of the turbomolecular pump should be held under medium vacuum. Backing pressure of $\leq 10^{-2}$ mbar is optimal to reduce molecular back flow and keep the turbomolecular pump operating correctly. The presence of molecules in a turbo creates friction in the bearings of the rotor when it is spinning at thousands of revolutions per minute, which develops into heating of the pump. Many modern turbo pumps have an interlock to shut down the turbo or seal it with a valve to prevent over-stressing the pump. A cross-section view of the inside of a turbo molecular pump is provided in figure 2.1 [82]. A turbomolecular pump was chosen for use on the project system to minimise contamination and for its compatibility with gases introduced into the system. A diffusion pump for example may contaminate a system and would not be capable of handling prolonged exposure to gases introduced in to the system. Turbomolecular pumps also offer greater pumping rates, essential for recovering vacuum between experiments.

The MBE growth chamber built and used during this project for preparing oxide thin films presented in this work, has a base pressure of 2×10^{-10} mbar. This vacuum is achieved by pumping the chamber down to 10^{-8} mbar with rotary and turbomolecular pumps then baking it out at 130°C to remove water vapour and hydrocarbons from the chamber walls. This establishes ultra-high vacuum of 10^{-9} mbar.

Further pumping the system below 10^{-7} mbar is the ion pump. This is used to keep the pressure low while analyzing samples with surface electron diffraction but is most advantageous on systems with vibration sensitive analysis tools, where mechanical pumps can be shut off. The ion pump consists of two charged plates. Molecules that pass between the plates are ionized by a large electrostatic field and then collected within holes on an anode plate. This process is supported by a magnetic field to assist with collecting the ions at the anode. This process is described in figure 2.2 [82] where cathode plates 1 and 2 separated by an anode 3 ionise particles within the pump that are collected within holed on the ion plate 3 with assistance from

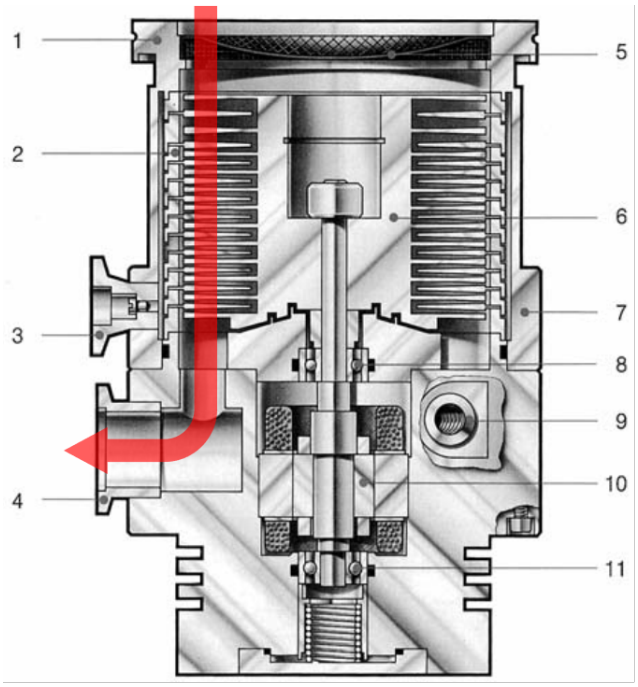

1 High vacuum inlet flange
2 Stator pack
3 Venting flange
4 Forevacuum flange
5 Splinter guard
6 Rotor
7 Pump casing
8 Ball bearings
9 Cooling water connection
10 3-phase motor
11 Ball bearings

Figure 2.1: A diagram of the inside of a turbo molecular pump, viewed in cross-section. This diagram was sourced from [82]. The arrow indicates the direction of flow of molecules that are transported by rotating blades mounted on and around a rotor, labelled 6.

a magnetic field B. The plates are charged to 7kV for optimal pumping efficiency but are vulnerable to damage from breakdown of molecules present in the pump at this voltage unless $<10^{-7}$mbar is reached. As a result, the ion pump is operated infrequently on the system due to the sources and operating pressures used. The ion pump is useful however for improving vacuum for electron diffraction experiments so as to reduce inelastic scattering of electrons from particles present in the system chamber.

UHV of 10^{-9} mbar or greater is maintained by a Titanium Sublimation Pump (TSP). This is an example of an entrapment pump where sublimed Titanium bonds with the free molecules in the system and deposits onto the walls of the chamber. The contamination can be removed again later by further baking. This pump is particularly useful for re-initialising the system after sample growth to ensure that contamination is minimized between experiments. This pump is also essential for

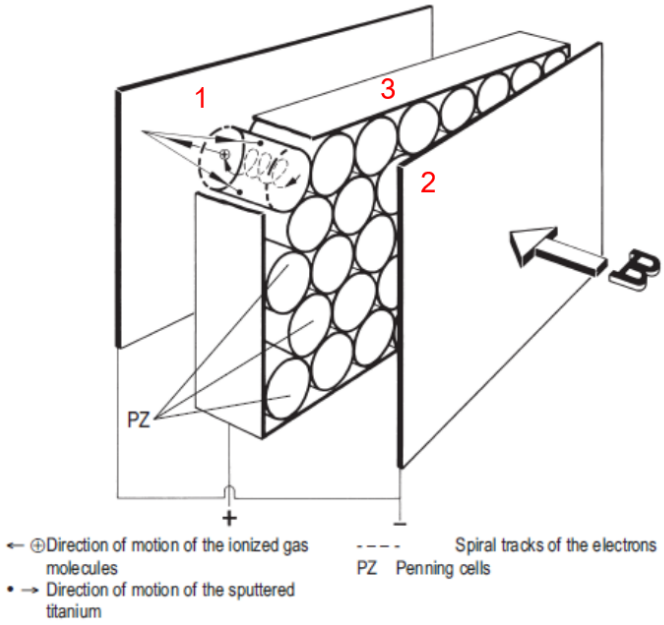

Figure 2.2: A diagram of the pump process that occurs inside an ion pump, sourced from [82]. The plates labelled 1 and 2 are both cathodes while the plate with an array of holes is the anode.

recovering UHV conditions between experiments and also provides entrapment of water vapour that may be introduced from gas lines in to the system.

When deposition sources are used, further improvements to the base pressure can be made by degassing. This process involves heating the sources up to 200°C, or just below the source operating temperature depending on the source material. A review of the sources is detailed in section 2.2.2. By heating up the sources and other filaments within the system, water vapour is boiled off and pumped from the system. Heating also prevents condensation of water vapour on to the sources and gauges.

The pressure in the system is measured using vacuum gauges, in particular pirani and ion gauges. Two gauges are used because they operate in different pressure/vacuum ranges. A pirani gauge is sensitive to low vacuum, where an ion gauge will not operate. At higher vacuum the ion gauge will provide accurate pressure readings where the pirani is no longer sensitive. The pirani gauge uses the resistance of a wire filament to determine the pressure of the system. Applying current to the wire filament increases its temperature. As the pressure decreases, thermal conductivity in the system decreases since there are less molecules to transfer heat to. Resistance of the filament increases with temperature, therefore if there are more molecules in

the system to transfer heat to, then the resistance will be low, indicating increased pressure in the system and vice versa [84]. A number of piranin gauges are employed on the project system for monitoring vacuum in the main chamber, in the FEL and on the backing lines of the turbomolecular pumps used. Problems with pumping and compromises in vacuum may first be indicated by readings on the pirani gauges so that maintenance can be conducted as quickly as possible to remedy the problems.

The ion gauge is a gas dependent method of measuring the pressure at ultrahigh vacuum. It uses an electric field to ionize particles in the system. This makes the gauge particularly sensitive at higher vacuum, but sensitive to damage and oxidation at low vacuum. The ions generated are then collected. The more ions collected, the more particles there are in the system, corresponding to a higher pressure. This is calibrated to nitrogen. Therefore, the ion gauge accuracy is reduced for other dominant gases in the system, but empirical correction factors can be applied [82].

Also appropriate to discuss within this section are some basic principles of good vacuum practice. The components listed above have limits and it is best practice to keep all components as clean as possible. When the pumps are mounted onto a stainless steel chamber a copper gasket and knife edge seal is typically used. Damage to a gasket or knife edge can be detrimental to acheiving ultr high vacuum, therefore when installing pumps on to a chamber it is good practice to use a new gasket and clean both the gasket and the knife edge with isopropyl alcohol, also checking the knife edge for damage. Wherever possible, minimising exposure to water vapour is essential. Nitrogen gas was available for venting on the project system. Using a slight over-pressure of Nitrogen, contamination from air in the system can be minimised. When pumping down, a useful component to have is a gas analyser or mass spectrometer to monitor the gas content in the system. Such components also help to indicate leaks within the system to atmosphere.

While the components listed above have been chosen to reliably provide UHV conditions, the ultimate base pressure achievable is still dependent on assembly of these components to form the system. A core component of a UHV system is the chamber to be pumped out. In this project a stainless steel chamber with fourteen ports was used. As discussed briefly above, the speed of pumping out a system depends on the diameter or bore of the chamber being pumped. On the project system, a turbomolecular pump is mounted on the system via an elbow extension piece. Any supporting components such as extension pipes increase the pumping load

and therefore also increase the time taken to achieve low base pressure. Furthermore, further seals are required to ensure that the system does not leak.

Installing components of a UHV system requires patience. Furthermore, all components must be cleaned thoroughly during assembly. For assembly of the project system, IPA was used extensively to ensure contact points between seals and the inner walls of components were not contaminated. Any contamination on the system will be difficult to remove once pumping begins and it will also be difficult to identify where contamination lies within the system once it is assembled.

To provide unrivalled sealing between components, copper gaskets are used. Flanges on port holes of the system comprise a knife edge. This knife edge and a further knife edge on the components that are to be mounted, bite into the copper gasket to create a seal. Any damage to a knife edge or incorrect mounting of a gasket could compromise the ultimate base pressure.

Assembly of the project system required installation of the pumps used and blanks on all other ports to test vacuum and pumping performance. A helium leak detector was temporarily installed on the system to provide backing pressure relief to the turbomolecular pump installed. Following this all of the seals were exposed to helium gas. If any leaks are present, helium will enter the system and be pumped by the the pumps installed. Since a helium leak detector is installed in series with the turbomolecular pump of the system, any helium pumped from the system will be detected, identifying the source of a leak.

Then each component of the system is installed and leak detection follows where necessary. Finally, to enable samples to enter and leave the system with minimal exposure of the system to atmospheric conditions, a Fast-Entry Load lock (FEL) is installed. The FEL has a gate valve between the FEL chamber and the main chamber. A transfer arm is also installed on the FEL to transfer samples under vacuum. The FEL has a rubber gasket seal on the sample door for re-usability. Once copper gaskets have been used, typically they will never seal as effectively again. The FEL is pumped by a separate turbomolecular pump and rotary pump in series. To further reduce contamination, nitrogen gas is used to vent the FEL or main system to atmosphere. Applying a slight increase in pressure of nitrogen over atmospheric pressure, dust and water vapour may be prevented from entering the system.

2.2 Molecular Beam Epitaxial growth (MBE)

2.2.1 Thin Film Epitaxy

The word *epitaxy* is of Greek origin meaning *ordered above*. Here the word is used to describe the crystallographic arrangement of atoms at the interface between two crystals. Having ordered single crystal interfaces is advantageous because it enables control of device properties at single atom precision. Crystal defects in thin films are an example of where the lattice match between two materials is high enough that in order to mitigate strain that would be induced by matching the arrangement of the base crystal, the crystallographic structure of the thin film dislocates atoms to more energetically favourable sites.

This also introduces novel material properties when considering thin films less than 5 nm thick, where interface strain creates large local electric fields. Due to the finite film thickness the electrostatic potential at the interface manifests into uncharacteristic material properties such as 2D electron gas and interfacial magnetism between otherwise insulating materials as discussed in the introduction.

Films of 2 - 30 nm thickness have been researched for this thesis, exploring the properties induced at the interface and the crystallography that drives them. Molecular beam epitaxial growth (MBE) is employed to control parameters such as thickness and crystallinity. For example, in this work MgO thin film growth uses simultaneous magnesium deposition and ambient oxygen exposure. By increasing magnesium deposition rate relative to oxygen plasma pressure, and vice versa, epitaxy can be controlled.

2.2.2 Deposition Sources

While there are several deposition sources and systems available, not all provide the precision and control to produce ultra-thin films. Magnetron and RF sputtering are examples of fast methods of depositing materials, but crystallinity is not easy to control when depositing by these methods, and annealing processes are usually required to improve thin film crystallinity. While chemical deposition methods are widely used, exposure to contamination removes control from the preparation of ultra-thin films. Hence, molecular beam epitaxial growth has been employed to exercise control for thin film deposition to atomic scale precision. The sources used for preparation and deposition of MgO and Fe_3O_4 thin films for this thesis include a Mantis hydrogen cracker, Oxford Applied HD-25 Oxygen Plasma source, Createc low temperature effusion cell for magnesium deposition and a Focus EFM3 e-beam evaporator source for iron deposition.

The hydrogen cracker was used for the preparation of SiC surfaces, however the atomic hydrogen process developed inconsistent results and increased the background pressure of the system significantly, as discussed in Chapter 6. Thin films deposited with atomic hydrogen present exhibited diffuse scattering in RHEED patterns and polycrystalline like RHEED patterns, with rings instead of spots. As a result, the source is not operated but hydrogen is passed into the system via the source to expose the substrate to molecular hydrogen.

The source aperture is sufficiently large enough to expose the substrate to hydrogen completely. However, should the hydrogen cracker be operated, it uses a filament to heat a Tungsten capillary to over 1500°C, through which molecular hydrogen flows into the system. The hydrogen molecules are cracked into hydrogen atoms from both the heat and catalytic behaviour within the Tungsten capillary.

Following substrate preparation,the MgO growth setup utilizes the oxygen plasma source for simultaneous deposition of magnesium and oxygen. The plasma source is operated at a power less than 100W. The use of a plasma source allows control of the oxidation strength to optimize growth conditions. The plasma power, oxygen pressure and plasma colour all provide control of the subsequent deposition process. The plasma is generated by inductively coupled RF excitation in an alumina crucible [85]. The radio frequency AC circuit oscillates current through the filament that is wrapped around the crucible. This is portrayed in figure 2.3.

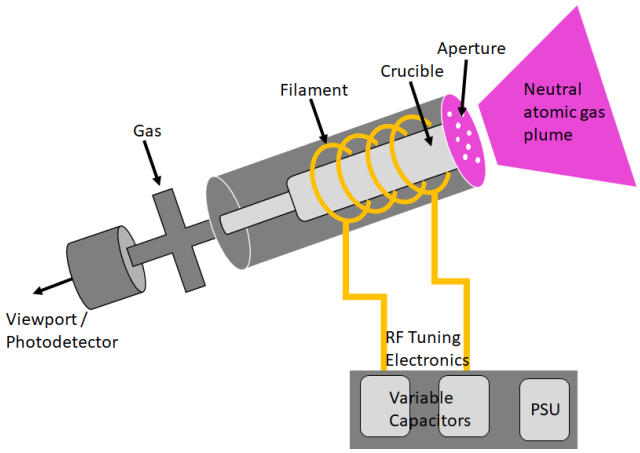

Figure 2.3: A schematic describing the operation of the Oxford Applied Research HD25 atom source.

The shape of the filament is helical identifying the inductively charged plasma type as cylindrical. As gas flows through the source, electrons in molecules of the gas are energised by a magnetic field generated by current passing through the filament. This interaction is as an electromotive force, described by Faradays Law of induction. The strength and direction of the force increases the kinetic energy of electrons in the molecules until kinetic energy overcomes the binding energy of atomic bonds in the gas and ionisation occurs [86].

The collection of ions and electrons creates a plasma contained in the crucible by electrostatic interactions between ions and electrons. Neutral atomic gas particles are not contained by this interaction and thus are drawn into the system by the pressure difference between the source and the system. The small apertures help to contain the plasma and suppress the number of oxygen ions introduced into the system as there are no ion deflection plates fitted to this particular source.

Magnesium is provided from an effusion cell. The optimal source temperature for deposition is between 270°C and 320°C. The principles of evaporation follow that of a Knudsen cell with some key differences. A Knudsen cell consists of a crucible, made of for example alumina, PBN or graphite, heated by a set of tantalum foil plates. The main difference between this type of source and the effusion cell used in this work is that the Knudsen cell has a closed end with a smaller aperture on the crucible. This creates an accumulation of material vapour in the source that passes through the aperture, the projection of which follows a cosine distribution.

Figure 2.4 describes the trajectories available to material vapour expelled from

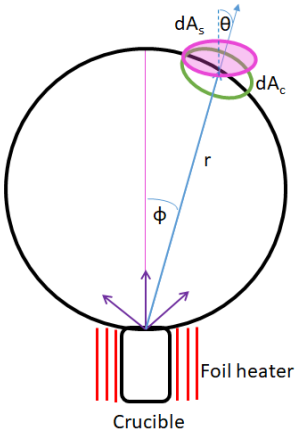

Figure 2.4: Schematic of a Knudsen cell and the distribution of vapour generated by the cell. θ is the angle that the surface normal is off from the source trajectory, r. ϕ is the angle at which material leaves the source with respect to the source axis.

the crucible of a Knudsen source. For a sample of area dA_c inside the sphere of material coverage, aligned to surface normal with the source, material will deposit uniformly across the substrate. The rate of deposition for mass M_c on the surface aligned normal to the point source and inside the sphere is given by

$$\frac{dM_s}{dA_s} = \frac{M_c cos\phi cos\theta}{4\pi r^2} \tag{2.1}$$

Of course exact alignment to the source is not always achievable yet it has an impact on the mass deposited on to the substrate. This is described by the area dA_s with surface normal positioned at an angle θ. The radius of the sphere r is is not to be confused with the particle trajectory in figure 2.4. Deposition from the Createc effusion cell similarly follows a cosine distribution but with the modification that particle trajectories are biased to the centre of the distribution. This is known as a Langmuir type cell. Benefits of a Langmuir type cell are that the operating temperature can be relatively reduced, because less pressure is required within the crucible to produce the required deposition rates since there is no aperture confining the particle trajectories. Also note that Knudsen cells without a heated lip tend to deposit on the inside of the crucible causing the aperture to become blocked after regular use.

Other tricks can be used to manipulate deposition parameters for example by adjusting the volume of material in the source since pressure is inversely proportional

to volume by the ideal gas law, particularly applicable to Knudsen cells wherein a closed system in equilibrium can be established.

Iron deposition is delivered from an e-beam deposition source. The EFM3 source uses a filament to heat a rod of material to be deposited. This is done by applying a high voltage, in the region of 800-1000V, between the filament and the rod, to excite electrons from the filament into vacuum and heat the tip of the rod. Sufficiently high temperatures can be achieved locally by this method to deposit materials with high vapour transition temperatures such as Iron, Cobalt and Nickel. An aperture is used to concentrate the flux at the cost of deposition area. Operating the EFM3 source can produce volatile deposition rates. Small increases in filament and emission current can largely increase the measured flux of metal ions from the source, which also depends on the position of the rod within the wound filament. This source can also be used with a crucible of material for deposition. Heating of the crucible allows vaporisation the material it contains. Electron emission from the EFM3 filament bombards and heats the crucible. This is shown in figure 2.5

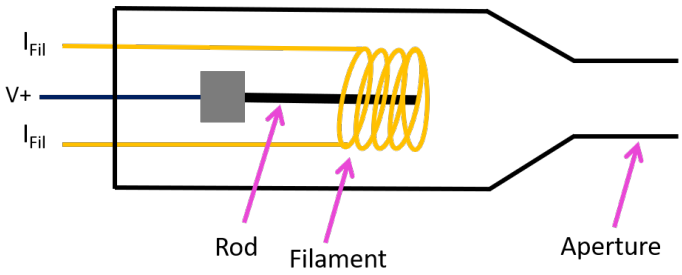

Figure 2.5: Cross section schematic of the EFM source and the components that define its operation. The rod of material is positioned inside a filament coil. By biasing the rod up to 1000V, electrons are excited from the filament and bombard the rod. The position of the rod is adjustable to maintain continuous flux.

2.2.3 Growth Modes

By adjusting the deposition source temperature and substrate temperature, the growth mode can be controlled. There are three growth modes considered herein. The first is 3D growth or Volmer-Weber growth. This is defined by the nucleation of islands of film that join as the film thickens and islands merge. The second growth mode is layer-by-layer growth, also known as Frank van der Merwe (FdM) mode. This growth is epitaxial, and each layer is deposited one at a time. The last growth mode discussed here is Stranski-Krastinov growth. This growth mode starts as epitaxial layer by layer growth, like FdM, but due to factors such as strain and temperature the film growth proceeds to nucleate into islands and 3D growth takes over.

The factors that dictate the dominant mode are as follows; vapour pressure of adsorbates, substrate temperature, and chamber pressure. To understand why these parameters are important one must look at the processes that happen on the surface during deposition. Atoms impinging the surface will saturate dangling bonds on the surface. Depending on substrate temperature and the strength of the interface bonding, the atom can become a nucleation site for the adsorption of other atoms or migrate across the surface to further nucleate islands of film. If the substrate temperature is too high, then desorption of adsorbed atoms may occur. The interface interactions between film vapour, film nucleation and atom migration can be described by Young's equation 2.2

$$\gamma_{sv} = \gamma_{fs} + \gamma_{fv} cos\theta \tag{2.2}$$

Condensation of evaporated material onto a surface is driven by the change in free energy between substrate-vapour (sv), film-substrate (fs) and film-vapour (fv) interactions during nucleation. Young's equation 2.2 is established through the evaluation of the strength of the interactions across the surface. Figure 7 identifies the components of these interactions that contribute to the film nucleation. The angle between substrate surface and a nucleus of film is important because only the component of the interaction between the film and vapour at the surface is required. By considering these interactions, Youngs equation can build a description of the three growth modes above. These are categorised in table 2.1.

Growth Modes	Young's Relation
Volmer Weber	$\gamma_{sv} < \gamma_{fs} + \gamma_{fv}$
Frank Van der Merwe	$\gamma_{sv} \approx \gamma_{fs} + \gamma_{fv}$
Stranski-Krastinov	$\gamma_{sv} > \gamma_{fs} + \gamma_{fv}$

Table 2.1: Definitions of the growth modes and their limits using Young's relation.

Although removed from the table for simplicity, the angle θ between the nucleus surface and the substrate surface dictates the magnitude of γ_{fv} and contributes directly to the growth mode. The limit that θ approaches zero describes FdM growth while $\theta > 0$ describes 3D growth. Once the film has complete coverage i.e $\gamma_{fs} = 0$ then the growth mode can be described as Volmer Weber or FdM. In this growth regime Stranski-Krastinov growth develops in to 3D growth where migration of atoms on the surface dominates. Knowledge of the growth constraints was obtained from [87]. Note that θ of the film vapour interaction is not linked to the sample angle discussed previously for deposition from a Knudsen cell.

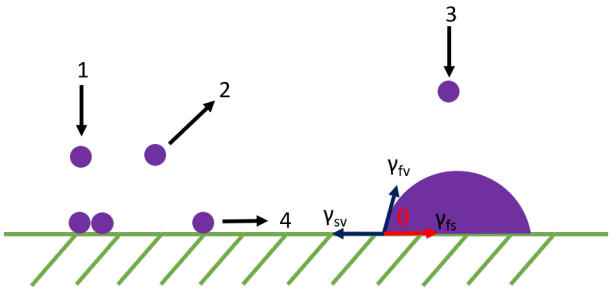

Figure 2.6: A schematic of the nucleation processes during MBE growth. 1) Adsorption of vapour molecules onto the substrate surface. 2) Desorption of vapour molecules where film-substrate interactions are weak. 3) Adsorption of vapour on nucleated islands of film. 4) Migration of film across the substrate surface.

2.3 Surface Electron Diffraction

Electron diffraction has been used for decades to uncover structures of bulk crystals, substrate surfaces and material interfaces. To discuss the surface electron diffraction techniques it seems appropriate to introduce electron scattering in crystals starting with the Bragg Diffraction, which is also applicable to X-ray diffraction of crystals.

Periodic arrangements of atoms, separated by a few Angstroms, form crystal structures. The scale of distances between atoms in such a periodic array is still large enough for electrons to pass and scatter between. For example, the de Broglie wavelength of an electron is 1nm for an electron energy over 1eV. In another example the wavelength of an electron, accelerated by a voltage of 200kV is theoretically on the order of picometers. As electrons or X-rays scatter through crystals, phase differences occur between electrons resulting in constructive and destructive interference of electron waves. The periodic arrangement of atoms in a crystal directly affect the phase difference and therefore the interference exhibited by radiation passing through the crystal. Examples ofproperties of the crystal that affect how electrons interfere with each other due to scattering are lattice spacing, atomic number, atomic radius, bond angle, space group (positions of atomic species in a crystal) and defects.

Examples of defects that may be observed in crystals are screw and edge dislocations. Screw dislocations may exist in SiC substrates as pipe dislocations, wherein the stacking sequence of SiC shifts on a number of atomic planes, resulting in a screw like pattern through the crystal. Edge dislocations may exist in MgO crystals as twin boundaries, wherein a shift in atomic planes creates a single shift resulting in a mirror-like image of the crystal structure across the dislocation. While these may be observed with high resolution electron microscopy techniques, they are difficult to observe with surface electron diffraction techniques.

An example of constructive and destructive interference between electrons scattered through a crystal is Bragg diffraction, which occurs when electrons or X-rays scatter elastically off atoms in a crystal and create a phase difference between the waves of electrons or X-rays scattered. It is electrons that are the focus of this section. Phase shift between electrons leads to interference. If the phase shift is equal to an integer number of wavelengths then the scattered electrons will interfere constructively. This leads to defined scattering trajectories where constructive interference will be observed. This also depends on the angle of incidence of electrons as they scatter

from atoms. So far this is considering only single scattering events of each electron incident on the crystal.

Figure 2.7 shows the parameters required to derive Bragg's law

$$n\lambda = 2dsin\theta \tag{2.3}$$

The scattering of electrons through crystals is considered in more detail in Chapter 4. If a single electron scatters from a crystal, the observation of the electron is only dependent on the angle of incidence for a single scattering event. It is the presence of multiple electrons that leads to interference and it can be seen from figure 2.7 that the condition for constructive interference is satisfied when the path difference is equal to an integer number of wavelengths, which can be related to the lattice spacing by trigonometry. The path difference of the electrons results in a difference in phase. For electrons to constructively interfere they should be in phase. Therefore, for the electrons to be in phase, the path difference and therefore the phase difference must be a multiple of the wavelength λ of the electrons.

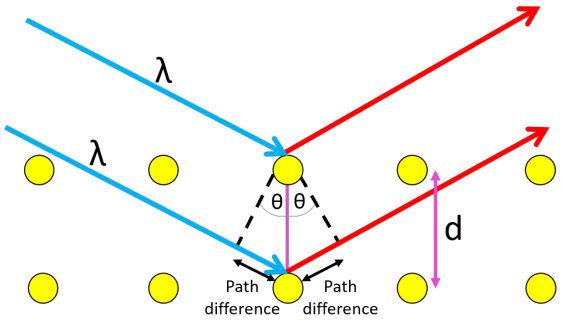

Figure 2.7: A diagram illustrating Bragg diffraction from atoms in a periodic array, identifying the parameters included in the derivation of Bragg's law.

While Bragg diffraction explains the geometry of electrons scattering through bulk crystals, Bragg's law does not apply to electrons scattering from surfaces, particularly in the cases of Low Energy Electron Diffraction (LEED) and Reflection High Energy Electron Diffraction (RHEED). When discussing the scattering of electrons from surfaces, in its simplest form there is no contribution from atoms below the surface to the scattering of the electrons. This is the main modification to the geometry of Bragg diffraction. Rather than scattering through a crystal of three dimensions,

the electrons are only scattered from atoms arranged in two dimensions. This is confined by both the energy of the electrons incident on the surface and the angle of incidence. Figure 2.8 describes two possible geometries for which diffraction occurs from surfaces.

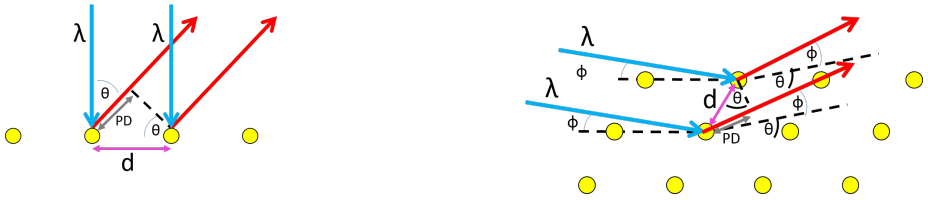

(a) (b)

Figure 2.8: Schematics describing (a) back scattered geometry for LEED and (b) reflective geometry for RHEED.

For each geometry outlined in figure 2.8 it is clear that the path difference, PD, of the electrons scattered from the surface can be resolved through trigonometry and derive equation 2.4, a variant of Bragg's law.

$$n\lambda = dsin\theta \tag{2.4}$$

Now that the basic principles of diffraction from crystals have been considered it seems pertinent to discuss the features of interest for analysis of electron diffraction patterns from surfaces.

2.3.1 Reflection High Energy Electron Diffraction (RHEED)

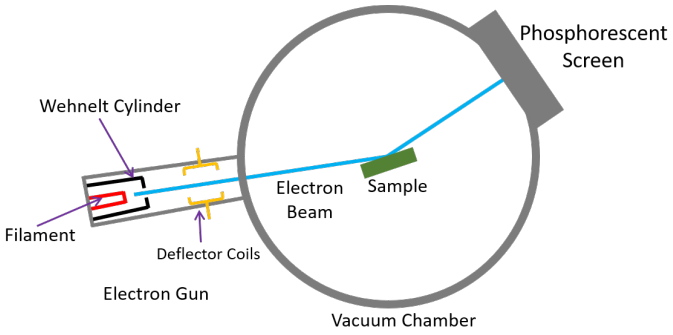

Figure 2.9: A simple diagram of the experimental RHEED setup on the project MBE system, viewed in cross section.

As discussed in the previous section, RHEED is a useful tool for determining characteristics of substrate and thin film surfaces. While RHEED is considered a qualitative technique, RHEED patterns still provide a wealth of information for understanding surface structures, as will be discussed in this sub-section.

The experimental setup for RHEED requires an electron gun. The gun consists of a filament, made of Tungsten in the case of the project MBE system. In order to perform RHEED in situ on the MBE system, minimum vacuum of $10^{(}-5)$ mbar is required. The filament will begin to oxidise and become damaged at higher pressures. The filament is heated by an electric current and thermionic emission of electrons is driven by a voltage in the range of 10-100kV. 15kV is used on the project RHEED system to accelerate the electrons from the filament and in to vacuum. Along the path of the generated electron beam is a Wehnelt cylinder that is used to focus the beam, thereby controlling the energy distribution of electrons in the beam. This reduces the background intensity in diffraction patterns from inelastically scattered electrons. The beam diameter at the sample surface is $\approx$ 1mm.

This beam of electrons is focused on to the surface of a sample at a grazing incidence, typically $< 8°$. Electrons are scattered off surface atoms and the interference of electrons creates a pattern following the condition for constructive interference described by equation 2.4. This pattern is observed when the scattered electrons impact a phosphorescent screen. Figure 2.9 describes the experimental setup. In order to describe formation of a diffraction pattern from the scattering of multiple electrons, an understanding of reciprocal space is required.

The real lattice is a description of the arrangement of atoms in a crystal through geometry. The reciprocal lattice is simply another description of the crystal structure using planes with a reciprocal relation to the real lattice geometry. This means that larger dimensions in real space will be smaller in reciprocal space and vice versa. The spacing of the features in the diffraction pattern correspond to reciprocal space.

The mathematical description of the reciprocal lattice requires the real space definition of lattice vectors. Since this is a section on surface analysis it is appropriate to describe the two dimensional surface lattice vector as

$$\mathbf{r} = n_1\mathbf{a} + n_2\mathbf{b} \tag{2.5}$$

where n_1 and n_2 are integer scaling factors for the basis vectors $\mathbf{a}$ and $\mathbf{b}$. Equally the reciprocal surface lattice vector can be written as

$$\mathbf{r}^* = m_1\mathbf{a}^* + m_2\mathbf{b}^* \tag{2.6}$$

where $\mathbf{a}^*$ and $\mathbf{b}^*$ are the reciprocal basis vectors and m_1 and m_2 are integer scaling factors. The relationship between the real space vectors will be stated here as

$$\mathbf{a}^* \perp \mathbf{b} \qquad\qquad \mathbf{b}^* \perp \mathbf{a} \tag{2.7}$$

Note that $\mathbf{a}$ and $\mathbf{b}$ are not necessarily orthogonal to one another. Figure 2.10 shows the conversion of a real surface lattice into its reciprocal form.

(a) (b)

Figure 2.10: The conversion of the lattice vectors from (a) the real lattice to (b) the reciprocal lattice. This diagram also shows the conversion of the lattice spacing, d.

To further describe the formation of diffraction patterns from surfaces, miller indices are required. These indices are used to give the directions of planes in reciprocal space. In three dimensions they take the form $(h\ k\ l)$, where each index is an

integer multiplier of a vector $\vec{u}$, $\vec{v}$ and $\vec{w}$ respectively. In two dimensions, i.e. surface geometry, only (h k) are required. The third dimension of a surface is continuous and can be represented as lattice rods in reciprocal space. The concept of the surface lattice rods becomes important when indexing diffraction patterns and determining how they are formed on the screen. Typical RHEED patterns constructed from diffraction of electrons from a surface consist of streaks. Formation of these streaks can be explained using the concept of reciprocal lattice rods. By applying the equation 2.4 a continuous sphere of possible diffraction angles can be constructed since the locus of all possible final wave vectors for elastically scattered electrons is a sphere. The radius of this sphere is dependent on the energy of the incident electron beam. The condition for constructive interference is met where the sphere intersects a lattice rod. This is described in figure 2.13. The sphere is known as the Ewald sphere. The larger the incident energy, the larger the radius of the Ewald sphere. Considering this information it can be seen, for the first order streaks, that the streak is formed in the diffraction pattern where the lattice rod intersects the sphere along its tangent. The Ewald sphere also explains formation of Laue zones where the sphere intersects other lattice rods. Streaking of features in a RHEED pattern is further amplified due to inelastic scattering from the surface and the fact that the incident electron beam has an energy distribution.

The energy spread of electrons generated from an electron source leads to a distribution in the wave number. For a point electron source with perfect optics, the beam can be focused into a parallel monochromatic beam approaching an ideal plane wave. The very dimensions of the electron source give rise to a spread in energy of electrons emitted. This energy distribution can be minimised by the addition of the Wehnelt cylinder but this is not a perfect fix. Therefore, the electron beam can be described by wave packets. This description does not consider the effect of temperature on the crystal and its consequences on the diffraction pattern formed. This is because the primary energy of the electrons is sufficiently high that small random shifts in the position of atoms on the surface has only a miniscule effect on the trajectories and phase of the electrons scattered. The energy distribution from the source masks any changes to the diffraction pattern due to brownian motion of atoms on the surface.

Electrons generated at the source are described as plane waves of a form e^{ikx}, which are propagating in a direction x with energy distribution ΔE. Therefore the

total number of electrons within the distribution gives the total wavelength distribution in equation 2.8.

$$\frac{1}{\Delta k}\int_{k_0-\frac{\Delta k}{2}}^{k_0+\frac{\Delta k}{2}} e^{ik_0x}dx = \frac{2sin(\Delta kx/2)}{\Delta kx}e^{ik_0x} \tag{2.8}$$

This means that for a monochromatic plane wave, $\Delta k \to 0$, the above equation forms that of a single plane wave that has an effective length tending to infinity. For a finite Δk, the effective length is obtained from $\frac{\Delta kx_1}{2} = \frac{\pi}{2}$ and $\frac{\Delta kx_1}{2} = \frac{-\pi}{2}$. This effective length, $l_{\parallel} = x_1 - x_2$, is known as the coherence length that describes coherence of wave packets scattered simultaneously by two points. Should the two points be separated by a distance larger than the coherence length then waves scattered from those points will not be coherent i.e the waves will not fulfill the requirements for constructive interference. As an example, for a source with energy distribution $\Delta E = 0.1eV$ and primary energy of $E = 10keV$ the parallel component of the coherence length is $\approx$ 2.4 μm.

For a source of finite size the electrons will not be focused into a perfectly parallel beam and there will be an angular spread $\Delta\theta$ that will affect both parallel and perpendicular components of the coherence length. For the perpendicular case, consider a Tungsten hairpin filament with wire diameter 0.1mm. The distance from the filament to the lens is $\approx$ 10cm. The angular distribution is $\approx$ 10 mrad that at 10keV primary energy results in a wavelength $\lambda \approx 0.1$ $\mathring{A}$ and the coherence length becomes $l_{\perp} = \frac{\lambda}{\Delta\theta}$, which is $\approx$ 100Å. For the parallel case, the coherence length is mostly determined from the angle of incidence θ_i. The variation in k_x forming the wave packet is $\Delta k_x = ksin\theta_i\Delta\theta$ and so the parallel component of the coherence length for the source described above with incidence angle $\theta_i = 2°$, is $l_{\parallel} = \frac{2\pi}{\Delta k}$ that equates to 350nm, for the above conditions. Therefore the instrument has a resolution limit given by the coherence length, which is discussed below for analysing RHEED patterns.

The shape of RHEED streaks is characteristic of certain surface features. For large flat surface reconstructions such as the Si-(7x7) of the order L $\approx 1\mu m$ [88], diffraction patterns consist of sharp spots where the width of the streak (or spot) is equal to $2\pi/L$. For rough surfaces, stepped surfaces or island growth, RHEED patterns are spot-like. The vertical spacing of the spots is equal to $2\pi/s$, where s is the step height. For extreme surface roughening and islands on the surface, electrons may scatter through such features and obey Bragg's law 2.3. Periodicity of the

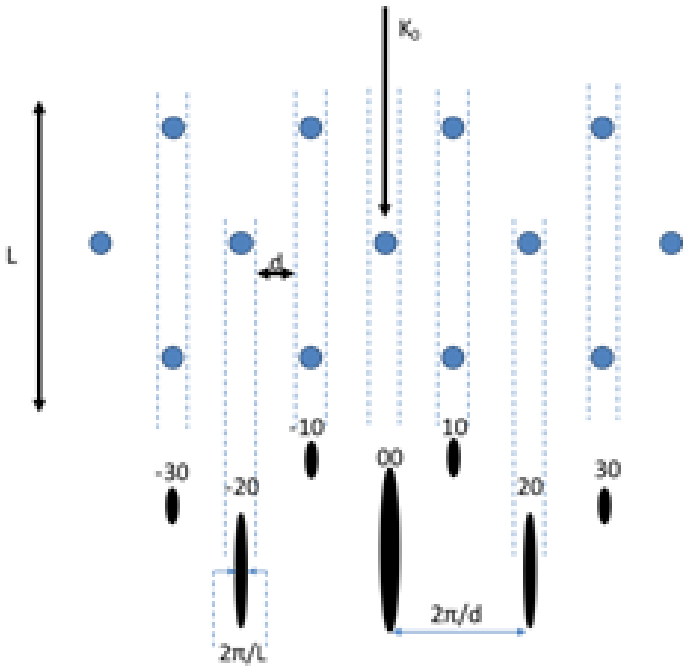

Figure 2.11: A diagram of the formation of a RHEED pattern from the reciprocal lattice, identifying the parameters for analysis of the pattern features

features results in an array of diffraction spots or rings depending on the arrangement of surface features. Figure 2.11 describes these features through conversion of the reciprocal lattice into pattern features.

The pattern in figure 2.11 has two rows of spots. The three main streaks labeled (00), (-20) and (20) form the zeroth order Laue zone, L_0, from the scattering of electrons from the plane perpendicular to K_0, the electron beam direction in reciprocal space. These indices correspond to their surface reciprocal space vectors (hk). The second row of spots labeled from (-30) to (30) form the first order Laue zone L_1, generated by scattering from the next plane along K_0. Figure 2.12 shows experimentally obtained RHEED patterns from (a) a flat surface prepared in UHV, (b) a rough surface with islands and steps, (c) transmission of electrons through surface features indicative of Bragg diffraction. The Laue zones are labelled where necessary. An "X" like feature over the (00) order streak in the diffraction pattern is formed from Kikuchi diffraction. This type of diffraction will be explored in detail in chapter 4.

Analysis of the shape of the features in the diffraction pattern is mostly qualitative yet can provide information about step direction, surface faceting and surface reconstruction. To form a map of the surface, it is useful to have a rotating sample stage that can rotate the sample in-plane. By rotating the sample it is possible to

observe diffraction from different planes along different zone axes. This is important when determining the type of surface reconstruction from the diffraction patterns which will be revisited in chapter 6.

To determine the lattice spacing of the surface with RHEED, the system is calibrated using a well defined substrate surface. MgO(001) was used to calibrate the project system because it has well defined surface reconstructions. This means that for a specific camera length from the screen, the spacing of the streaks from the diffraction pattern will be x pixels or mm apart as viewed by the camera, which is equivalent to reciprocal lattice plane spacing. Alternatively, for calibrating the lattice spacing of thin film surfaces, the substrate peaks can be used as a reference. In either case, the equality 2.9 can be used wherein d_s and d_f are the reference and measured lattice spacing and L_s and L_f are the reference and measured streak spacing on the screen respectively.

$$\frac{d_s}{L_s} = \frac{d_f}{L_f} \tag{2.9}$$

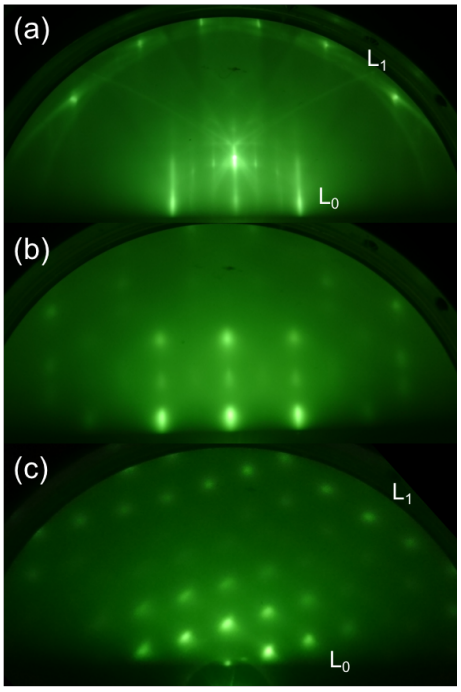

Figure 2.12: Experimentally obtained RHEED patterns from (a) a flat surface prepared in UHV, (b) a rough surface with islands and steps, (c) transmission of electrons through surface features indicative of Bragg diffraction.

Further details on RHEED pattern analysis and Dynamical RHEED can be studied from the book on RHEED by Ichimiya and Cohen [89], from which the knowledge in this section was acquired.

2.3.2 Low Energy Electron Diffraction (LEED)

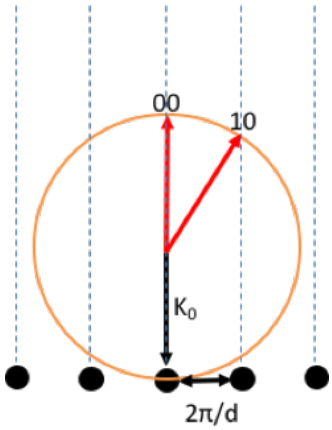

Figure 2.13: A diagram of the Ewald sphere intersecting the reciprocal lattice rods in back-scattered geometry.

Like RHEED, the technique of surface electron diffraction by back scattering obeys the modified Bragg's law 2.4, however in order to do so, the primary energy of the beam is much lower, typically up to 400eV. This means that the diffraction pattern created in LEED is due to the interference of electrons scattered from surface atoms, because the energy of the incident electrons is too low to penetrate into the crystal bulk and even if the electrons could penetrate beyond the first few atomic planes, they would not have sufficient energy to escape the crystal. The De Broglie wavelength [90] of a 100eV electron is $\approx$ 1.2Å, so even at low energies, compared to RHEED and electron microscopy techniques, the instrument can resolve atomic distances.

The condition for diffraction from atoms on the the surface in back scattered geometry is described in figure 2.8(a). The electrons incident on the surface have a wave vector, k. Elastically scattered electrons that meet the condition for constructive interference are described by equation 2.4. The Ewald sphere, described in figure 2.13, is a map of all the possible scattering angles and where the sphere intersects a surface reciprocal lattice rod satisfies the condition for constructive interference. This is all discussed for RHEED geometry in section 2.3.1 however, the main difference

in the construction of the LEED pattern is that the radius of the Ewald sphere is much smaller than that for RHEED, due to the reduced beam energy, and as a result, the LEED pattern is an array of spots, rather than streaks, mapping out the surface reciprocal lattice. The experimental setup of the instrument is shown in figure 2.14 where electrons are generated from an electron gun, which has a Lanthanum hexaboride (LaB_6) filament on the project system. The advantage of using a LaB_6 filament instead of a Tungsten filament is that the energy distribution of the electrons generated is smaller. This is partly due to dimensions of the filament, but is also due to the work function of the filament. The LaB_6 filament is shaped to a sharp tip to approximate conditions for a point source, to reduce energy spread of the beam and thereby minimise inelastic scattering. This filament type also has a longer working lifetime than Tungsten filaments, ideal for UHV conditions so the lowest possible base pressure can be maintained.

Similar to the RHEED system, electrons are filtered by a Wehnelt cylinder and are then focused by electromagnetic lenses to approach parallel beam conditions. Such lenses are the L_1, L_2 and L_3 lenses, the strength of which can be varied to focus electrons to a point on the sample with $\approx 100\mu$m beam diameter. The sample is positioned $\approx$ 10cm from a screen. The screen is biased to 5kV electric potential to uniformly accelerate electrons onto a phosphorescent screen.

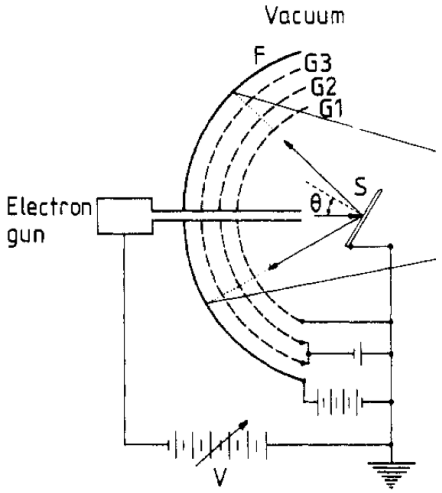

Figure 2.14: A schematic of the Low energy electron diffraction system viewed in cross section. The sample is labelled S, the grids focusing the electrons are labelled G_{1-3}, the phosphorescent screen is labelled F, and the energy of the electron beam is labelled V. Although the sample is drawn with tilt θ, LEED is typically conducted at normal incidence. Image sourced from an article on LEED by Jona et al. [91]

Analysis of a surface by LEED is conducted by varying the primary electron beam energy. Increasing the beam energy results in two outcomes; higher scattering angle and increased sample penetration, although the primary energy will not be high enough to penetrate more than ≈2nm at its maximum. This does make the instrument sensitive to both the surface and selvedge of the sample. Due to the interference of elastically scattered electrons, this becomes convoluted and so simulations of the kinematics from the scattering of electrons from different surface structures is required to accurately identify the correct structure. This technique of analysis is Dynamical LEED and will not be considered again in this thesis however the principle of this technique is worth mentioning briefly. The intensity of the spots can be tracked as the energy of the electron beam is increased and decreased. From this, spot intensity vs. beam energy (IV) can be plotted. Simulations of IV curves for scattering of electrons from predicted surface structures can be fitted to the empirical data in order to determine the structure of a sample surface. In this thesis, only indexing of the spots and the pattern geometry has been utilised to analyse sample surfaces with reference to the literature.

The spots that appear in the diffraction pattern represent a map of the recip-

rocal surface lattice. As the primary energy increases, the angle at which electrons scatter off atoms increases, causing spots on the screen to translate toward a specular reflection of the electron source. As beam energy increases, the scattering angle for higher order diffraction falls within the angular field of view of the screen and higher order spots are observed on the screen. These spots identify surface reciprocal lattice directions relative to the specular reflection and can be indexed with miller indices (hk) for the 2D reciprocal lattice. By analysing spacings between first order and higher order spots, parameters such as lattice spacing and surface reconstruction can be determined alongside features such as specular reflections and surface steps.

The LEED instrument is calibrated in a similar way to the RHEED system; using a well defined reference surface structure, in order to convert distances between spots on the screen into atomic distances. In all diffraction patterns, a longer length in reciprocal space corresponds to a shorter length in real space and vice versa. This is important to consider when deducing the type of surface reconstruction and surface lattice parameter. For the discussion of the heavily reconstructed MgO surface in Chapter 7 it seems pertinent to describe the formation of LEED patterns from faceted surfaces.

Diffraction from flat surfaces with normal incidence exhibit a specular reflection where electrons are scattered directly back into the path of the electron beam. This is the (00) spot. Elastic scattering is also observed from faceted surfaces, where the surface has reconstructed into an ordered array of tilted planes because the surface energy density of these planes is significantly lower than that of frozen bulk or reconstructed surfaces. Since facets are tilted at an angle off normal incidence, the electron beam is reflected off the surface and can be further reflected by surface features. When coherence of electrons in the primary beam is sustained over multiple reflections, specular reflection spots can be observed on the screen. The spot formed in a diffraction pattern from a specular reflection can be identified by the fact that the position of the spot does not alter with or depend on the primary energy of the electron beam, and the position of a specular spot can only be changed by tilting the sample.

2.3.3 Indicators of successful sample preparation by MBE

Using the deposition system and techniques described above, a systematic method for determining successful growth of MgO thin films was developed. A number of trial attempts at depositing MgO thin films were conducted. While thicker MgO films were consistently produced during this project, preparing thin MgO films of around 2nm depth was difficult, however the successful conditions are presented below and in Chapter 7.

Key components of the system used to identify indicators of successful growth are the quartz crystal microbalance (QCM) and RHEED instruments. Monitoring the deposition rate of Magnesium before and after deposition ensures that the conditions for exposure of a substrate to magnesium is consistent for each deposition. Oxygen adsorption on a SiC substrate surface is essentially guaranteed making the Mg source conditions critical to successful Mg deposition. The magnisum deposition rate measured by the QCM drastically shifts with temperature. As the source becomes hotter, the time for the QCM to stabilise increases. This can be misleading and patience is required for the QCM to stabilise. Water cooling the QCM is essential to acquiring reliable deposition rates. The background pressure of the system is also vital for determining accurate deposition rates. Background pressure during Mg deposition was 1 x 10^{-8}mbar.

Between 270°C and 320° the deposition rate of Mg increases drastically as temperature is increased. Table 2.2 shows the deposition rate measured at 10°C intervals in the above temperature range.

Temperature in °C	Deposition rate in Å/min
270	1
280	1.5
290	2
300	3
310	6
320	10

Table 2.2: A table showing Magnesium deposition rate as a function of temperature measured using the QCM of the project system. Note that deposition rates measured are dependent on background pressure and the volume of material in the source.

As presented in Chapter 7, 280-300°C source temperature is typically used for thin film deposition for this project. This Mg source temperature was settled upon

based on initial deposition results from RHEED and TEM and conditions reported in literature [92]. Initial conditions for the oxygen source were also sourced from literature and are discussed in Chapter 7.

Following deposition, initial analysis of samples by RHEED will provide an indication of the quality of the samples. RHEED patterns from both substrate and film surfaces identify key indicators of successful sample preparation. For example, diffuse scattering and reduced intensity of features from Kikuchi diffraction in the RHEED patterns may indicate small domains on the surface, which for substrate surfaces may inhibit subsequent thin film growth.

Similarly, diffuseness of features in LEED and RHEED patterns may also indicate inconsistent surface features, such as steps and islands. For MgO thin film growth, as shown in later chapters, RHEED and LEED patterns may include features indicating surface roughness even for successful samples. Features in RHEED patterns indicating failed sample preparation include rings and diffuse background scattering. Failed samples may show no pattern and diffuse electron scattering in LEED patterns. Features of interest in diffraction patterns from successful samples are presented in later chapters.

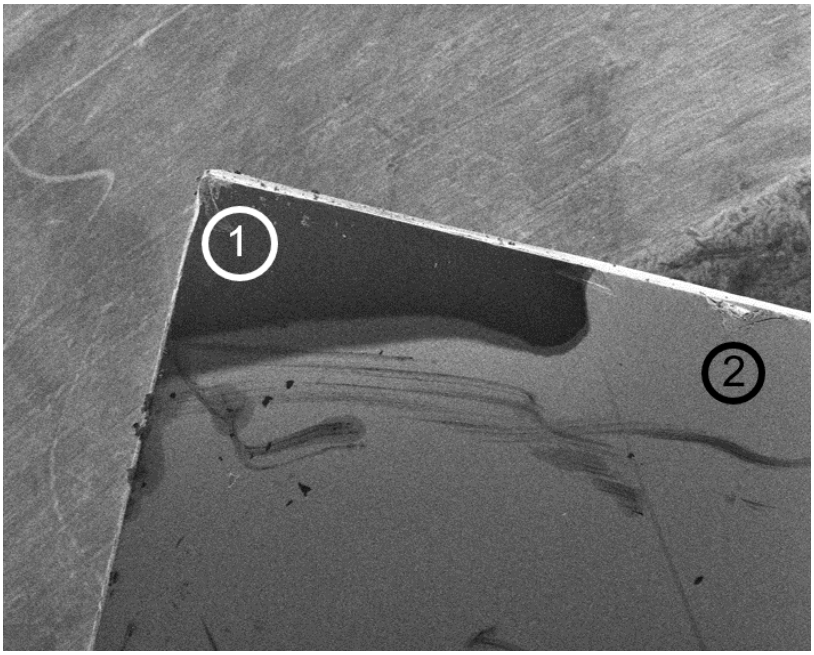

Figure 2.15: A secondary electron micrograph from a corner of a successful MgO/SiC sample. Area 1 shows dark contrast representative of the substrate where a clip holding the sample covered the substrate during deposition. Area 2 shows an area of bright contrast associated with film deposited on the surface.

Further indicators of successful sample preparation can be found from further analysis by ex-situ techniques. After analysis by RHEED and/or LEED, Scanning Electron Microscopy (SEM) may be used as an ex-situ technique to analyse samples. An indicator of successful sample preparation observable by SEM includes distinct contrast in secondary electron yield from areas of the sample. In addition to SEM imaging, chemical mapping by Energy Dispersive X-ray Spectroscopy (EDS) in the SEM should also identify the presence of magnesium and oxygen on a successfully prepared sample. Figure 2.15 shows indicators of successful sample preparation observed by SEM.

Note that other chemical analysis techniques may be used to analyse samples such as XPS. X-ray Reflectivity (XRR) experiments were also attempted on samples however due to low film thickness and similarities in density between film and substrate, XRR measurements did not provide indicators of successful sample preparation. Once indicators of successful sample preparation have been observed, one may proceed to preparation of specimens from samples for transmission electron microscopy.

Chapter 3

Characterisation by electron spectroscopy

3.1 X-ray Photo-electron Spectroscopy (XPS)

X-ray photoelectron spectroscopy is a surface sensitive technique for determining the chemistry of sample surfaces and interfaces. The chemical information obtainable by XPS technique is vast because the technique is able to probe energy levels from atomic core shells up to valence electronic levels [93]. The spectra are essentially maps of the density of states of a material system. The technique requires a X-ray source, typically assembled with an Al or Mg anode to generate a $K\alpha$ X-ray emission line of 1253.6 eV or 1486.6 eV for Mg and Al respectively. These are popular choices due to the narrow X-ray line width generated from these elements.

The XPS results reported in this thesis have all been acquired in experiments with a monochromated X-ray source. The monochromation of X-rays is achieved through Bragg diffraction of the generated X-rays off quartz crystals, in order to create a narrow X-ray line width and stop the X-ray spectrum from broadening, impairing the energy resolution of the instrument. X-rays can also be focused within a monochromator by shaping the quartz crystal. Another type of X-ray source available is a dual anode source, wherein multiple anodes may installed, for example either an Mg or Al source can be used. Both monochromated Al and dual anode sources have the same operation. A LaB_6 filament is used as an electron source. The anode is biased to >10kV, which excites electrons from the filament that bombard the anode, generating X-rays by ionisation and relaxation of electrons bound in the anode material. The LaB_6 filament is chosen over a W filament for high electron yield,

which proportionally leads to the generation of more X-rays. The dual anode source is usually positioned close to the sample and as a result illuminates the entire sample area. the monochromated source is usually focused to a spot of ≈3mm diameter in order to improve intensity and, by shifting the sample position, improve spatial resolution.

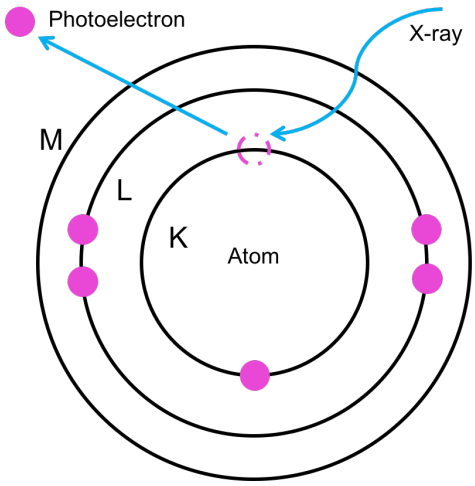

Figure 3.1: A schematic of the ionisation process inside the atom with the orbitals labelled K, L, M.

Although the elements used in the dual anode produce narrow X-ray line widths, the distribution of X-ray energy and local heating from bombardment processes lead to sample heating and peak convolution when acquiring spectra, which leads to lower energy resolution. A benefit of monochromated sources is that damaging heating effects are significantly reduced and peaks do not require deconvolution because of the narrow X-ray line width. However, sample charging is more of an issue with monochromated sources because of the reduction in local charge compensation when compared to exposure from a dual anode source. To make the charging uniform throughout the energy range of measurement, a flood gun can be used to provide charge compensation to provide electrons to the surface, typically <5eV.

The XPS system is held under UHV conditions, $\approx 10^{-10}$mbar, in order for the photoelectrons generated in the sample to have a long mean free path and reach the analyser, and to minimise any modification to the surface from contamination. Therefore the XPS instrument is typically mounted on the same system as the sample preparation or growth system. In this work, collaboration with XPS specialists has required exposure of samples to atmospheric conditions in order to transfer them from the growth system in to a remote XPS measurement system. The generation of

electrons from a sample originates from ionisation of electrons from electron orbitals in the atom, described in figure 3.1. The sample is secured to the manipulator using silver paste to minimise contamination and charging. Elastic collisions of X-ray frequency photons with bound electrons in the atom provide ionised photoelectrons with kinetic energy of the incident X-rays minus the orbital binding energy. The generated photoelectrons are then collected by an energy analyser. The energy of the electrons collected by the analyser is then expressed as

$$E_B = h\gamma - E_k - W \tag{3.1}$$

where E_B, $h\gamma$, E_k and W are the binding energy, X-ray photon energy, kinetic energy of the electron and work function of the analyser respectively.

An example of the analyser used for acquiring spectra reported in this thesis is a hemispherical analyser. Figure 3.2 describes the analyser components with a cross-section schematic. The analyser consists of two concentric hemispheres between which there is a path along which collected photoelectrons can travel. The two hemispheres are biased to accelerate the electrons around the path inside the analyser to channeltrons. The magnitude of the bias on the hemisphere varies as the analyser scans through an energy range of measurement. The angle of trajectory of electrons entering the analyser is critical for the collection of the electrons at the channeltrons and therefore the intensity of the electrons measured in the hemispherical analyser is low relative to the number of photoelectrons that may be generated in the sample. This is addressed at both the entrance and exit of the analyser.

Photoelectrons entering the analyser have too much kinetic energy for the analyser to process, therefore a transfer lens is used on entry to the analyser to reduce the kinetic energy of incoming electrons to ≈300eV. This also acts as an energy filter as the analyser scans through the energy range for a measured spectrum. The transfer lens is also capable of aligning the electrons onto the tangential path of the hemispheres in the analyser, increasing the acceptance angle of the analyser and the number of electrons detected. At the exit, the sensitivity is further improved through the use of multiple detection channels. The electron intensity may be amplified by up to 10^8 electrons per photoelectron incident in a channeltron. A channeltron is a helical tube that is closed and positively biased at one end. The wall of the channeltron tubes are coated so that incident photoelectrons in the channeltron with energy greater than the coating work function can generate many secondary electrons. The

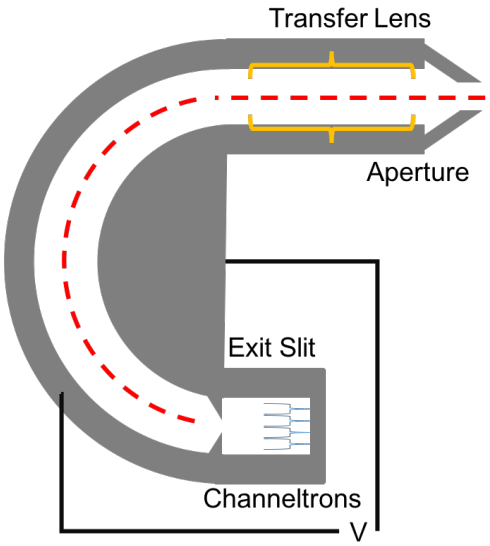

Figure 3.2: A cross section view of a hemispherical analyser. The dashed line marks the ideal path of a photoelectron through the analyser. The inner and outer hemispheres are biased to accelerate the electrons of a desired energy through the exit slit into the channeltrons.

positive bias at the end of the channeltron accelerates the secondary electrons that can cascade through the channeltron generating even more secondary electrons.

In theory a hemispherical analyser is capable of achieving an energy resolution better than 0.1% of the energy it is set to during measurement. The analyser is operated in constant analyser energy (CAE) mode. This means that throughout the measurement energy range, the potential difference between the inner and outer hemisphere surface is constant, which means that the energy resolution throughout the energy range is also constant. If the pass energy that the electrons are accelerated to is small (≈20eV) then the potential difference between the hemispheres is small, increasing the resolution and if the pass energy is higher then the intensity increases, at the cost of resolution due to the widening of the potential difference across the hemispheres. Error in sensitivity due to the interference of the Earth's magnetic field is compensated for by constructing the analyser from high magnetic permeability metal.

The XP spectra are recorded by collecting the intensity of photoelectrons within a defined kinetic energy range, which is usually converted to binding energy. The more steps used to measure through the energy range increases the resolution, while increasing the dwell time at each energy increases the signal acquired. With this in

mind, the time to acquire high resolution spectra can be high and the risk of high dwell time is that the charging of the sample can change during acquisition, shifting the spectra. A method for combating this is to have multiple scans of the same range and summing them but this is still time intensive.

In almost all experiments, a survey scan is conducted on the sample. Figure 3.3 is an example survey spectrum. This is conducted in the energy range from ≈1350eV - 0eV for measurement with an Al Kα X-ray source. Once the peaks in the survey scans and the peaks of interest have been identified, further spectra are acquired around selected peaks at higher resolution. The binding energy obtained from fitting of the peak can be used to search on the NIST database [94] for a chemical state that the peak has been generated from. These orbitals are labeled with respect to the quantum number n and the angular momentum quantum number l. Peaks labelled with KLL originate from Auger electrons generated in the sample through energy conservation when electrons move from outer orbitals to replace the photoelectrons ionized from core levels. The generation of photoelectrons throughout the energy range leads to a non-continuous background of counts in the spectra. This background baseline is known as the Shirley background. This tilts the base line of spectrum peaks requiring correction before fitting said peaks. A charge correction is also required. Scattering of X-rays can generate secondary electrons and regions of positive charge in the measurement area that interact with outbound photoelectrons, shifting their kinetic energy. This is less of an issue with metallic semiconducting samples but is important to consider when measuring electrically insulating substrates. Gold or silver are usually used as a charging reference to correct spectra. Carbon can also be used as a reference but is not as reliable due to contamination containing carbon bound in different states. While a charge reference material provides reliable calibration, charging of the sample may not be continuous throughout the energy range of measurement, therefore use of a flood gun to create a continuous charge offset may be used as a reliable charging compensator.

When analysing peaks in spectra, there are some conditions that decide how to best fit data. The shape of a peak is almost Gaussian however the bias of background electrons to the lower kinetic energy (higher binding energy) end of the spectrum makes Guassian fitting inappropriate. This has led to modified Gaussian and Lorentzian functions, popular functions being of Doniach Sunjic and Pseudo-Voigt type. These allow asymmetry parameters to best fit the peaks after the Shirley background

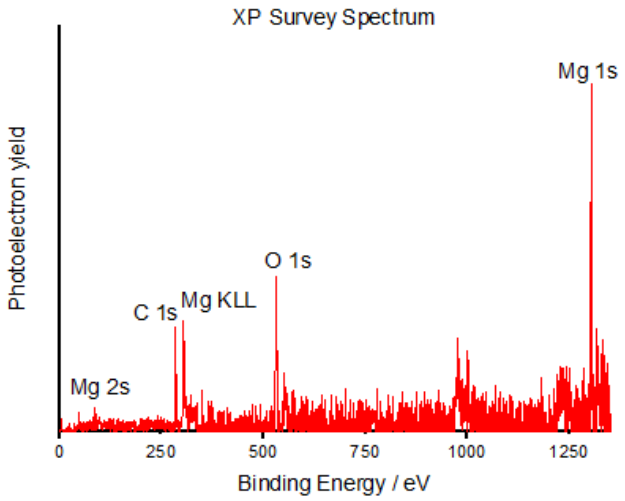

Figure 3.3: A survey scan of the MgO surface, identifying the orbitals from which the photoelectrons are generated.

is removed. Once the peak is fitted, analysis of peak parameters such as the full-width-half-maximum (FWHM) provide information on the source of the photoelectrons that comprise the peak of interest. If the FWHM is $\geq$2, then that suggests that more than one function is required to fit the peak correctly and that could be a satellite or other chemical state present. This is described in figure 3.4 where a shoulder peak is present on the Carbon 1s spectra, both at 90° and 30° X-ray incidence. The intensity of the shoulder increases at 30° incidence because the sample tilt reduces X-ray penetration into the sample, making the instrument more sensitive to surface electronic states. This is known as Angle Resolved XPS. As a result, multiple peaks can be fitted to these multiple states. The separation of the shoulder and core peak may not always be clear and therefore the value of the fitting parameters for one peak can help to deduce the requirements for further peak fitting.

The information presented in this section has been sourced and interpreted from Watts and Wolstenholme [95] and Briggs and Seah [93], both of which provide extensive detail into the XPS measurement technique.

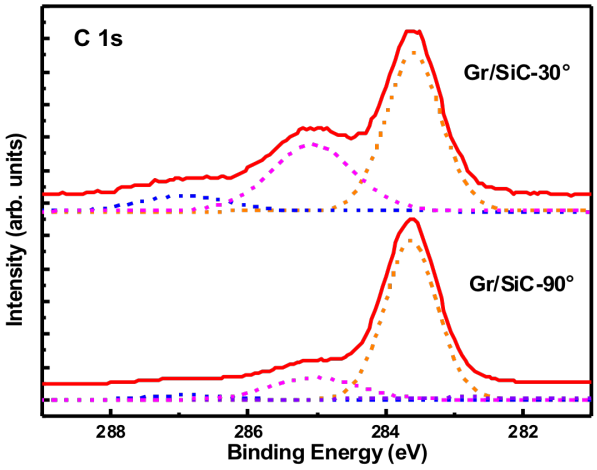

Figure 3.4: The fitting of multiple peaks to the C 1s orbital peak from a graphene (Gr) terminated SiC(0001) surface. The 30° and 90° scans refer to different incidence angles of X-rays on the sample. Tilting the sample allows the surface sensitivity to be adjusted.

3.2 Band offset measurements

Band alignment of materials at the interface is important for the development of novel electronic devices. The physics of band alignment discussed in the introduction will be discussed briefly again here in order to explain the analysis of XPS spectra for band offset measurements.

When materials are bonded together, the Fermi level of each material shifts to align with the Fermi level of the other. For the interface of two different semiconducting materials, depending on the width of the band gap and the position of the Fermi level within the band gap, the valence and conduction band alignment can be described by either the type-I, type-II or type-III band alignment. The difference in energy between the bands of each material then leads to localised charge transfer at the interface, which is described by band bending. Figure 3.5 shows an energy band diagram for the alignment of two semiconducting materials, where the Fermi levels are aligned following Anderson's rule [71] and band bending is observed.

The XPS technique can be utilised to measure the energy position of the valence band maximum, the last bound electronic states of the system. Measurement of the

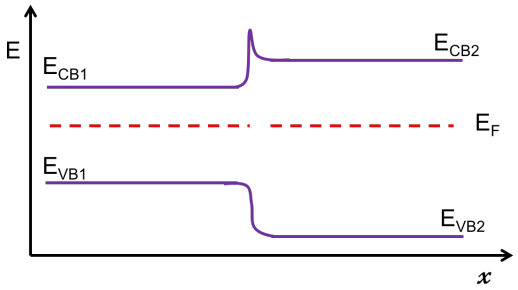

Figure 3.5: An energy band diagram at the interface of the two materials. The axis E is decreasing binding energy while x is the distance through the interface of the two semiconductors.

valence band maximum requires high resolution and low noise acquisition of spectra. Figure 3.6 illustrates a spectrum acquired at the valence band edge and its appropriate fit. The valence band maximum is the lowest bound electronic state that can be measured in XPS and so the energy value of the valence band maximum is derived from the energy axis intercept for the line fitted to the spectrum i.e. the final point where the intensity of photoelectrons approaches zero because no more electrons can be excited by X-rays from the sample above this point and below the Fermi level.

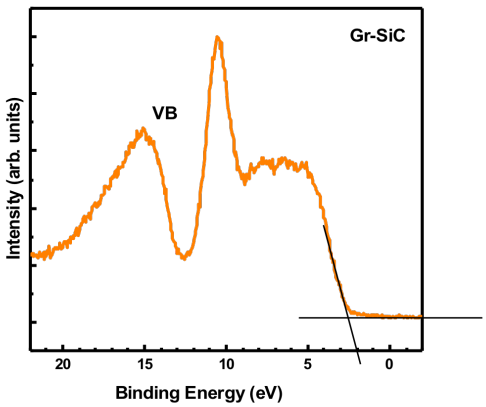

Figure 3.6: An example XP spectrum of the valence band edge from a graphene terminated SiC surface. A linear fit is extrapolated to intersect the background baseline. The binding energy at the intersect is the energy of the valence band maximum. This is to account for the broadening of the XP spectrum.

Although a tail can be observed at the edge of the VB spectrum in figure 3.6, a linear fit is best as it accounts for the tail on the spectrum due to broadening of the XP spectrum from background electrons comprising secondary electrons. Where the

line intersects the background baseline is the position of the binding energy for the valence band maximum [96, 97].

To determine the valence band offset using XPS, core energy levels of the bonding states from each material are required. This means that multiple samples or measurement stages are required. Firstly, the position of the binding energy for the core levels and valence band maximum from the substrate surface are required. Next, the core level spectra are required from the interface. This is collected from a sample with a thin film ($\leq$5nm) to allow the collection of core levels from both the substrate and the film close to the interface. Finally, the binding energy position of the core levels and the valence band maximum are required from a thick film or bulk reference. From the analysis of these spectra, the valence band offset (E_{VBO}) can be calculated using equation 3.2 [41, 98–100].

$$E_{VBO} = \Delta E_{CL} + [E_{nl} - E_{VBM}]^{Film} - [E_{n'l'} - E_{VBM}]^{Substrate} \tag{3.2}$$

ΔE_{CL} is the difference in binding energy between film and substrate core level bonding states from the spectra at the interface. For there to be a valence band offset there needs to be a shift in the binding energy between the core level states at the interface and in the bulk. The difference in the core levels between E_{nl} and $E_{n'l'}$ at the interface, where n and l, prime or not, are the electron orbital quantum number and angular momentum quantum number respectively. The "bulk reference" core level and valence band edge spectra for the film and substrate are used to calculate the positions of the valence band edges, on each side of the interface, relative to the core level bonding states. The difference in these positions is the valence band offset, described in figure 3.7 [101].

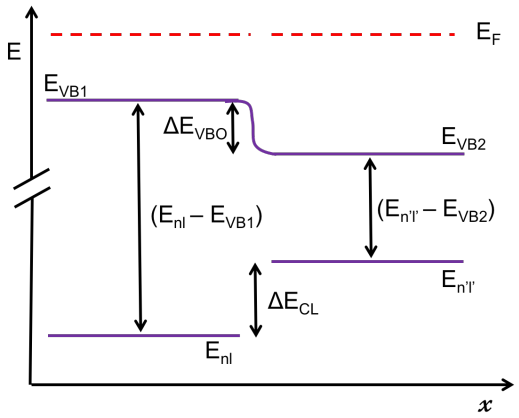

Figure 3.7: A simplified schematic of the energy band diagram for clarifying the origin of the calculation of the valence band offset.

Chapter 4

Analysis of atomic structure using Transmission Electron Microscopy (TEM)

The transmission electron microscope (TEM) is an important instrument for understanding the origins of the electronic properties and structural properties of thin film hetero-structures. The atomic structure at the interface can define the electronic structure across the interface through lattice mismatch induced strain or intermixing, charge transfer and electric dipoles, as described in chapter 8. Like with surface diffraction techniques, because of the short de Broglie wavelength, electrons are able to scatter through crystal lattices and can be collected on a screen or recorded on a CCD, forming an image. Unlike X-rays, electrons, although accelerated by several hundred kV, cannot penetrate through a sample on bulk scales i.e. mm thicknesses. Therefore TEM requires involved sample preparation techniques to reduce the specimen thickness to sub-80nm, which are discussed in this section but to start, the discussion will look at the components of a microscope and how an image is formed.

Electrons generated in a TEM are accelerated by 100-300kV potentials. This accelerates the electrons up to $\approx 0.6c$, where c is the speed of light in a vacuum. Therefore relativistic considerations are required for describing the behaviour of an electron in a vacuum. From the modification of the de Broglie equation relating kinetic energy to wavelength [90];

$$\lambda = \frac{h}{p} \tag{4.1}$$

the relativistic relation between wavelength and energy of the electron can be determ-

ined from equation 4.2.

$$\lambda = \frac{h}{(2m_0eV(1+\frac{eV}{2m_0c^2})^{\frac{1}{2}}} \tag{4.2}$$

This is equation is derived from a relativistic modification of momentum p substituted into the de Broglie equation.

A source is required to generate electrons in the microscope and to ensure electrons can reach the sample the system is held under UHV conditions, using ion and diffusion pumps to sustain vacuum without introducing vibration to the system. UHV is also required to reduce contamination on the sample. The instrument is shaped as a long column with a narrow tube for the electrons to travel down. Typically an electron source is positioned at the top of the column and electrons are focused by a series of lenses through the instrument to a screen and/or sensor at the bottom. Figure 4.1 describes the position of each component in a TEM. The discussion of components begins with the electron gun.

4.1 Generation of electrons in a TEM

On early TEM instruments, thermionic emission was favourable using LaB_6 as a filament over W, for its narrower energy distribution and longer working lifetime. This is the same method of generating electrons as in the surface electron diffraction techniques, where heating of the filament can allow electrons to overcome the work function of the filament material. To reduce the energy distribution of the electrons further and to improve the brightness, the choice of electron source type was changed to a Schottky Field Emission Gun (SFEG). The SFEG generates electrons using both heating and electric potential. The filament is made of W, shaped into a fine point. The fine tip shape, electric potential and heating of the filament, enables sufficient reduction of the work function to allow electrons to tunnel out of the filament. For example a 1kV potential can create an electric field of $\approx 10^{10}$ Vm^{-1} across the tip of the filament.

Although the SFEG type was an improvement over the thermionic emission type, development of the electron gun was taken further and the Cold Field Emission Gun (CFEG) was introduced. The main difference is that the CFEG generates electrons, as the name suggests, without heating and by electric potential alone. The filament material and design remain the same as the SFEG type. By removing the

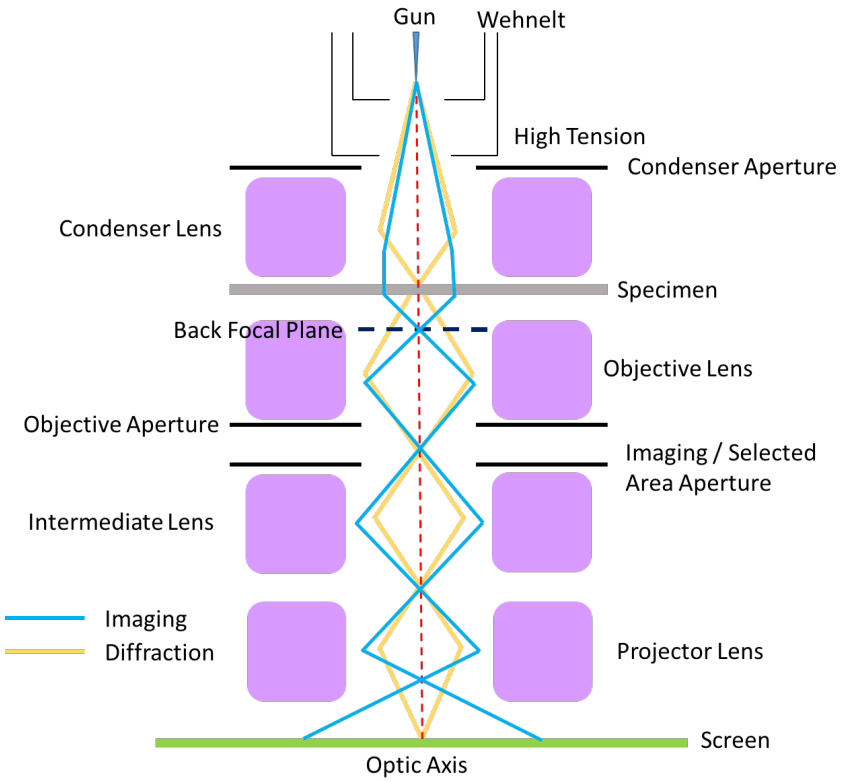

Figure 4.1: A schematic of the lens layout and optical path of the electrons for both imaging and diffraction modes. In reality the column is very narrow and the beam is deflected by lenses at angles on the order of mrad.

heating element, the CFEG can generate a more monochromatic beam with similar brightness. Although the reduction in chromatic aberration (C_c) is important, by designing the filament as a fine tip the electron beam is also spatially sharper, improving the maximum resolution of the microscope. The electron beam undergoes further energy filtering from a Wehnelt cylinder before being accelerated by a 100-300kV electric potential towards the specimen.

4.2 Lensing of high energy electrons

Just as in optical microscopy, where glass lenses are used to refract light, lenses are used in the a TEM to deflect the path of electrons. The lenses in the TEM are electromagnetic lenses typically comprising pole pieces with windings of wire. Current driven through the wire windings creates a magnetic field that is amplified by the pole piece in order to generate sufficient force to deflect high energy electrons.

Using multiple pole pieces enables a lens to deflect the beam in multiple directions within the plane of the lens. Research into electron lenses is continuous in an effort to combat unwanted aberrations and astigmatism. Such aberrations include chromatic and spherical aberration. The chromatic aberration originates from the distribution of energy within the electron beam, causing the lenses to deflect the electrons by different amounts. A similar effect is observed when electrons enter a lensing plane at large angles or at distance from the optic axis. These high angle vector electrons are deflected more than those closer to the optic axis resulting in a loss of phase and an increased energy distribution within the beam. This is known as spherical aberration. Figure 4.2 describes the effect of these aberrations on the trajectories of the electrons in the beam.

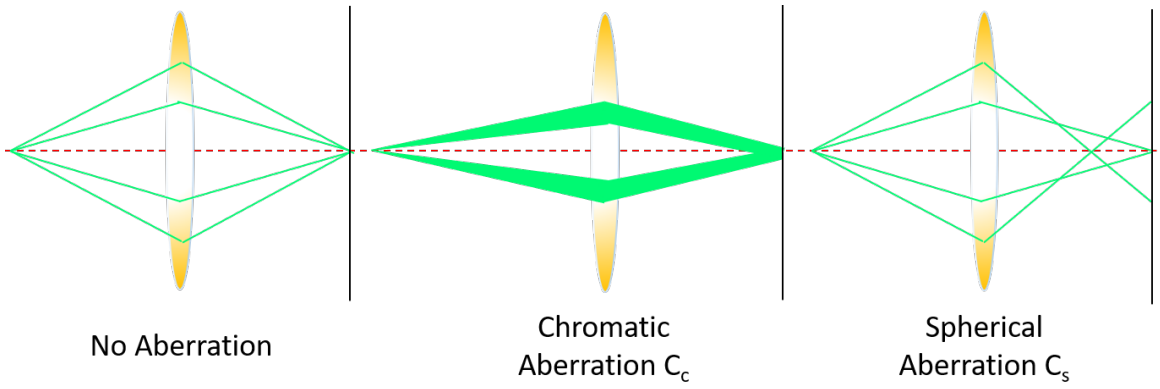

Figure 4.2: A schematic of the effects of chromatic and spherical aberration on the electron beam due to lensing. Chromatic aberration results in a broad energy distribution in the beam that is not completely focused by the lens. Similarly the amount that the beam is deflected by the lens away from the optic axis is greater than that of the beam deflection closer to the optic axis, resulting in electron beams that are not focused at the back focal plane.

Astigmatism arises from the shape of the lens. Ideally magnetic fields forming the lens should create a round lens so that all beam vectors within the lensing plane are focused equally. When adjusting the power of the lens to focus the beam, astigmatism can arise from hysteretic effects of magnetising the pole piece in the lens. This is corrected using stigmators, typically in the form of a quadrupole electromagnetic arrangement. Figure 4.3 illustrates the effect of astigmatism on the image of a sample.

Correction of distortion to the image due to astigmatism is particularly important at high magnifications (>250kX). Increasing magnification alters the current passing through the objective lens coils that changes the strength and shape of the

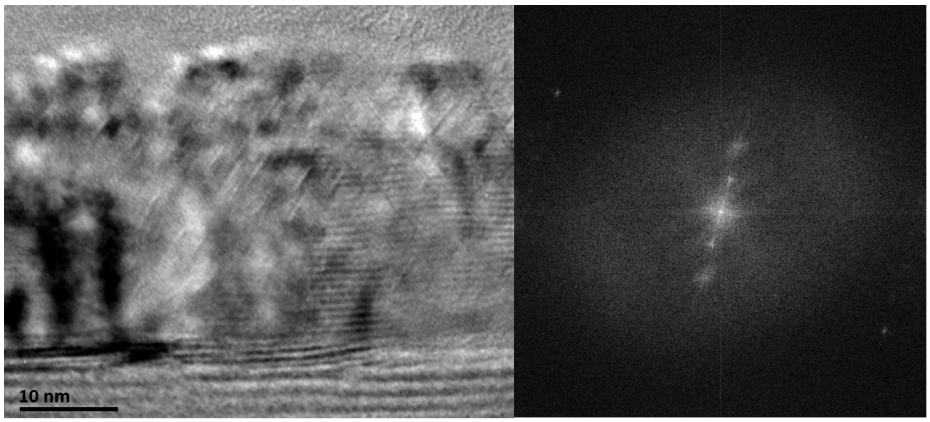

Figure 4.3: An image of a sample (left) where the roundness of the magnetic field has not been corrected. This causes features in the image to elongate in the direction that the lensing magnetic field has become an elongated ellipse. A fast Fourier transform (FFT) (right) of the original astigmatic image shows an ellipse-like disc indicating that the shape of the magnetic field requires correction.

magnetic field due to the magnetic interactions between pole piece. Magnification of an image in light microscopy is achieved by swapping lenses for higher refractive index glass to deflect the light more so that a larger image is formed at the eye piece. In the TEM there is no option to swap lenses on the fly however the strength of the magnetic field generated by the electromagnetic lens can be increased to achieve greater deflection of the electrons.

Apertures in a microscope are used to limit the angular range of electrons in the beam as they pass through the column. This helps to reduce spherical aberration and align the beam along the optic axis. The proximity of the apertures to the lenses does mean that charging of the aperture plates can distort the magnetic field of a lens, contributing to astigmatism. Apertures are fundamental to dark field (DF) and bright field (BF)imaging, where positioning an objective aperture over a diffraction spot allows a microscopist to record an image containing only the information that contributed to the diffraction spots enclosed by the aperture. Figure 4.4 illustrates the process of filtering diffracted beams to choose the electrons corresponding to certain reciprocal lattice vectors by positioning an objective aperture over specific diffraction spots. Another result of using an aperture is change to the contrast of a formed image, since the intensity of electrons is decreased, reducing the exposure. This can also be manipulated when navigating across thin specimens where the contrast observed on the phosphorescent screen can make it difficult to see an image of the specimen by

eye.

The Selected Area Aperture set is used for acquiring diffraction patterns of certain areas of the sample. When diffraction patterns are formed from constructive and destructive interference of electrons scattered through a specimen, as described in 2.7 they include interference from electrons scattered and collected along the column, however electrons included in the final diffraction can be limited using a Selected Area Aperture. This is particularly useful for analysing the crystal structure of epitaxial thin films on substrates, where omission of electrons scattered by the substrate crystal structure is advantageous to enable accurate analysis of the diffraction pattern from a thin film independently. Analysis of diffraction patterns is important when studying the crystal structure of specimens in the TEM because it can provide more information about the crystal structure than can be acquired from a TEM image. For single crystal specimens the distance between diffraction spots corresponds to the spacing between crystal planes while the crystalline uniformity dictates sharpness of the spots.

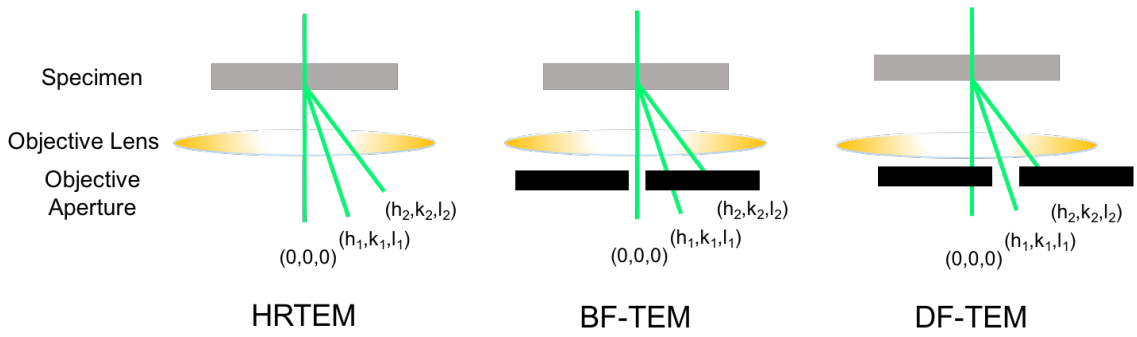

Figure 4.4: At high magnifications all of the electrons scattered by the sample are required in order to obtain high resolution (HRTEM) images. Positioning an objective aperture on the back focal plane to include just the central beam and electrons lightly scattered by the specimen is known as bright field imaging (BF-TEM), while positioning the aperture over a diffraction spot for electrons scattered further from the optic axis corresponding to diffraction from the reciprocal lattice $h_(n), k_(n), L_(n)$ is known as dark field imaging (DF-TEM).

An image of a specimen is created from the scattering of electrons as they pass through a specimen. At low magnifications, contrast in the image is defined by the scattering and absorption of electrons in thicker specimen regions and from heavier element atoms. At high magnifications, wave nature of the electrons dominates and interference of electrons scattered by the specimen dominates the image contrast. For HRTEM at high magnification, the cleanest images are generated when inelastic

scattering is minimised. This is achieved by making a specimen very thin; <80nm. The next section describes methods of producing specimens to view the sample in cross section.

4.3 Preparation of cross section specimens

4.3.1 Manual polishing

Preparation of a specimen for TEM starts with cutting the sample in order to expose a face of the sample in cross section. This is required for imaging and analysis of thin film interfaces. The sample is cut into 0.9mm wide strips. The number of strips available depends on the total sample size. The sample is mounted to a glass slide with resin and a diamond coated disc saw is used with water at low rpm to produce sharp cuts without damaging the sample surface. Where the saw is too aggressive, pits in the sample surface may be observed that will increase the risk of the sample cracking at later stages of preparation. During the cutting phase the specimen will require silicon supporting pieces, used to provide structural support and indicate sample thickness when thinning. Silicon will transmit red light when the sample thickness approaches $<10\mu$m. The silicon pieces are typically cut from 5x5mm square silicon slabs to create 0.9 x 5mm area strips, the same width as the sample strips. The strips will either fall into a water bath below the disc saw or remain on the glass slide once cut. The strips are then cleaned using acetone, ethanol and IPA, however for the MgO thin film specimens analysed for this thesis the ethanol step was skipped because reports indicate that MgO can be soluble in ethanol.

Once cleaned, two strips are bonded face to face using a heat activated epoxy mixture. Only a small amount needs to be applied and the strips are compressed together and heated by a hot plate to set the resin. Figure 4.5 shows an example of how the pieces are contiguously positioned. The structure consists of two sample strips supported by two Silicon strips.

Once the sample sandwich structure is prepared, it is mounted to a glass slide with glue, with the length of the strips running parallel to the length of the glass slides. This allows the sample to be handled when polishing. The sample is polished on the cross-section exposed surface using diamond polishing pads of 15, 9, 6, 3, and 1μm coarseness. The sample is polished down to a smooth, scratch free finish on one side, observable with an optical microscope, particularly at the glue line between the two strips because scratches and pits in this region can cause cracks at a later stage. The specimen is polished in water to lubricate the slide over the pad. At this stage the sample can be removed from the slide and cleaned in Acetone, Ethanol and IPA to remove contaminants before applying a copper or molybdenum grid to the

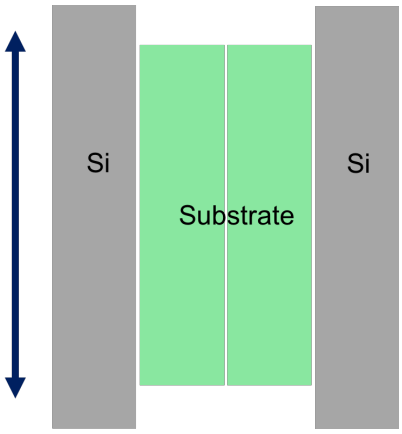

Figure 4.5: A schematic of the sandwich structure assembled from the substrate and Si strips. The arrow indicates the polishing direction to minimise the material pulled across the glue line while polishing. The small space between the strips represents the epoxy layers.

specimen, bonded to the polished side using epoxy. The grid is circular and 3mm in radius with a slot or hole in the centre that is 1mm wide. The glue line between sample strips is positioned across the middle of this slot or hole. Copper grids are cheaper but molybdenum grids are more resistant to sputtering when ion milling than copper grids.

Upon setting the epoxy by heating the grid bonded to the specimen, the specimen with grid is mounted on a slide exposing the side previously mounted to the glass slide in the first polishing stage. Here it is important to ensure that the grid is positioned as flat as possible and that no bubbles are observed in the glue beneath the specimen, which can be observed using an optical microscope. Once set in the same relative position as the first side, the specimen can be polished on the second side, again using 15, 9, 6, 3 and 1μm diamond pads, except a thickness guideline is used to determine when to switch to a finer pad. These are outlined in table 4.1. The specimen thickness is measured using a micrometer accurate to $\pm 0.5\mu$m.

Once the specimen has been polished to $<70\mu$m total thickness the final step is to continue polishing until the silicon support pieces transmit red light. Alternatively a dimple grinder can be used with 1μm polishing paste to thin the sample. This adds an advantage of thinning the sample most in the centre that can help during the ion milling stage and prevent resputtering because the milling will take less time, however

Required polishing pad	Specimen thickness, x
15μm	$>200\mu$m
9μm	$150\mu\text{m} < x < 200\mu\text{m}$
6μm	$120\mu\text{m} < x < 150\mu\text{m}$
3μm	$100\mu\text{m} < x < 120\mu\text{m}$
1μm	$<100\mu$m

Table 4.1: A table linking the polishing pad used at specified specimen thicknesses. Once the specimen thickness is less than 100μm the sample is polished at 1μm until the silicon support strips transmit red light, observable in a transmission optical microscope.

the results are similar to manual polishing. This stage should optimally conclude with orange silicon strips and minimal damage to the sample strips. The specimen can then be removed carefully from the slide and cleaned in Acetone, Ethanol and IPA in preparation for the final thinning step by ion milling.

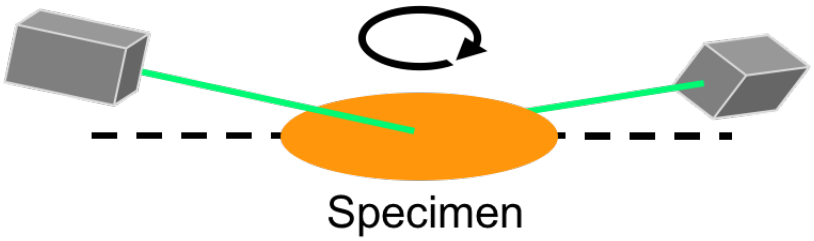

Figure 4.6: A schematic of the double ion milling configuration used in the Gatan PIPS. The dashed line describes the specimen plane while the solid lines show the ion beam trajectories from each gun. The rotation of the sample is coordinated so that milling alternated from the top and bottom side of the specimen.

The ion milling process performed on samples prepared for this work was conducted using a Gatan Precision Ion Polishing System (PIPS). This system holds the specimen under medium vacuum on a variable speed revolving platform. Ion milling occurs by the introduction of Argon gas that is ionised in one of two guns. These guns are set between 3-5kV during early milling stages, to accelerate Argon ions at a designated angle toward the specimen. When used in a double milling configuration, the

angle of the guns can be set between -10° to +10° off the specimen plane, where each gun is set opposite in angle to the other. Ion milling of the specimen starts at ±5° with 4kV Argon ion beam voltage to generate ≈30μA of ion current. The milling time depends on the initial specimen thickness. If the sample is too thick milling will take many hours and the specimen will become damaged before the specimen is thin enough for microscopy. This ion beam damage means that milling times should be kept to a minimum. At this point attention should be payed to the glue line and milling intervals of around 20 minutes should be performed. Using a reflection optical microscope the glue line can be observed.

Once approaching electron transparency, the central glue line should exhibit colour fringes from its interaction with a white light source, observed with an optical microscope. Further milling at 2-5 minute intervals should thin the sample steadily enough to observe the formation of a small hole in the glue line. A picture of this result is shown in figure 4.7. Switching to ±8° and <1kV starts the cleaning phase with the aim to gently widen the hole. After a short period, typically less than 5 minutes, the sample is ready to be observed in the TEM. Some back and forth from the microscope to the ion milling system may be required until the sample is the optimum thickness. More details on the specimen preparation conditions can be found in [102].

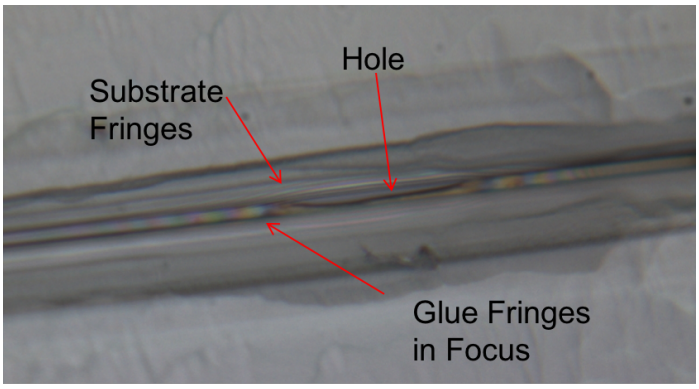

Figure 4.7: A micrograph acquired using an optical microscope identifying the final condition of the glue line after ion milling. Colour fringes can be observed around a black hole in the glue line.

4.3.2 Focused Ion Beam Lithography

In recent years the preparation of TEM specimens by Focused Ion Beam Lithography (FIB) has become popular due to its improved sample thinning over manual polishing. This of course comes at the cost of an expensive FIB instrument accompanied by a competent experimental officer to get the best results, however sub-100nm samples can be made with some patience. Methods for creating cross section specimens from a sample using FIB are described in [103, 104]. For oxide thin film surfaces, a conducting layer is required on the surface, which also protects the film from ion damage. The process of FIB utilises a Gallium ion beam to etch material away from the sample. Alignment of the ion beam is very important, especially at later thinning stages.

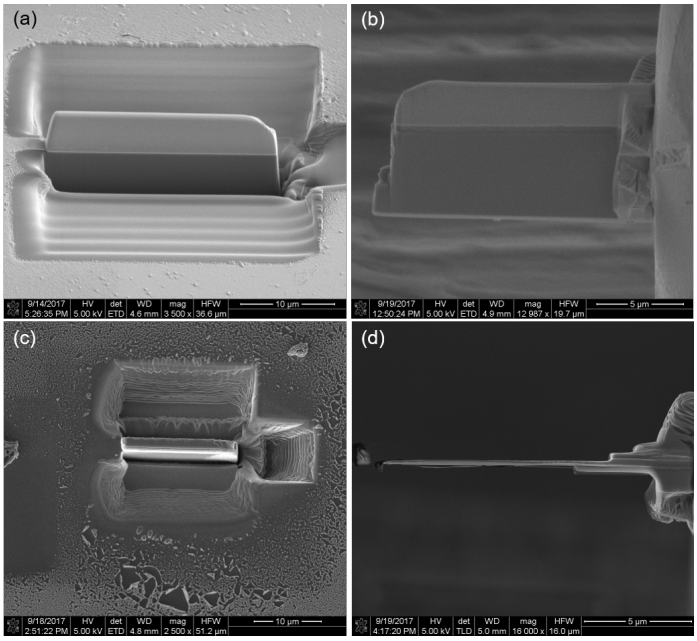

Figure 4.8: Secondary electron images of the TEM lift out process conducted in a FIB-SEM. (a) Shows the lamella being formed by ion milling tranches into the surface. (b) Shows the lamella mounted on to a grid. (c) and (d) are top view images of the lamella imaged in (a) and (b) respectively.

First an inert metal is deposited on the sample surface before loading the sample into the FIB vacuum chamber. Once under vacuum and the sample area is located, an electron beam is used to deposit a few hundred nanometers of platinum onto the sample followed by subsequent ion beam deposition of platinum of around 1μm thickness. The electron beam formed platinum layer comprises a high concentration

of carbon cracked by the electron beam, providing better adhesion than just ion beam formed platinum alone. The whole specimen "wedge" width is 30μm by 2μm once main trenches are etched above and below the platinum rectangle deposited by the ion beam. The sample can then be removed using a needle and platinum welds. The sample is then welded to a copper or molybdenum grid where the final specimen thinning is conducted.

Figure 4.8 provides secondary electron images of the lithography process. A lamella of 2μm depth is milled out of a trench. The bright contrast on the top of the lamella is platinum. The lamella is removed with a needle and welded with platinum onto a TEM grid. Finally the lamella is thinned to <100nm thickness in a multistep thinning procedure, the results of which are shown in figure 4.8(d).

As with the manual polishing final stages, the sample may need to be checked and undergo more thinning until the sample is optimised for imaging with electrons. While FIB specimens are improving in quality and it enables the user to acquire specimens from multiple areas of the sample, there are still some drawbacks to the technique namely; being unable to image the as grown surface of the sample due to platinum deposition, specimen crystal axis alignment of the specimen is non-uniform across the specimen because it bends at low thicknesses and not every microscopist has access to such an instrument. The majority of specimens prepared for this work were produced by manual polishing.

For specimens prepared by both FIB and manual polishing, TEM is utilised during the final stages of thinning and cleaning the specimens. In this work, a non-aberration corrected TEM with 200kV beam voltage was used to observe the specimens throughout the final stages of specimen preparation. Some iteration between ion milling systems and the TEM is required in order to achieve optimum specimen thickness without damaging the interface to be observed. Specimens are observed at low magnification, $\approx$10k$\times$ magnification, to assess and identify areas of interest on the specimen.

Diffraction mode in the TEM may also be used to navigate a specimen. Defocussing the beam, i.e. spreading the beam, in diffraction mode enables a low magnification image of the specimen to form on the screen. Diffraction is also used to tilt the specimen on to a preferred crystallographic orientation. Typically a camera length of 30cm is adopted in diffraction when performing initial analysis of specimens.

In TEM experiments, a double tilt holder was used to ensure that the specimen was aligned to the crystallographic axis of the film and/or substrate. This axis is referred to as the zone axis. Without this alignment through tilting, obtaining atomic resolution is difficult due to scattering from atomic planes in the specimen that interfere with electrons scattered from planes in the specimen associated with the crystallographic axis of interest.

Specimens prepared by FIB are typically more difficult to align on zone axis due to bending of the lamella during thinning and charging under the electron beam in the microscope. However, manual prepared specimens may have a variable tilt due to the wedge shape as the specimen approaches the glue line from thinning by ion milling.

For thin and subsequently successful specimens, images are also acquired at high magnification, typically up to 800k$\times$ magnification, to acquire atomic resolution images. Magnifications of this scale are also required to observe very thin films for example of nanoscale thickness.

Results presented in later Chapters from work conducted in collaboration with SuperSTEM, include STEM images acquired at 100kV acceleration voltage. The instrument used for acquiring the data also utilises a probe corrector for correcting aberrations induced by the lenses on the electron beam. The physical principles of correctors are not discussed in this document, however the author refers the reader to [105] for further reading.

4.4 Scanning Transmission Electron Microscopy

While TEM allows analysis of crystal structures, the interference of multiple electrons contributes to the entire image, therefore ordered crystal structures are observed by phase contrast however this means that determining the structure of defects and the position of each element in a compound has previously required simulations of HRTEM imaging. The development of Scanning Transmission Microscopy (STEM) has developed research into material interface and defect structures thanks to the Scanning probe method of forming an image. This section describes the principles of STEM and the tools used to analyse STEM images.

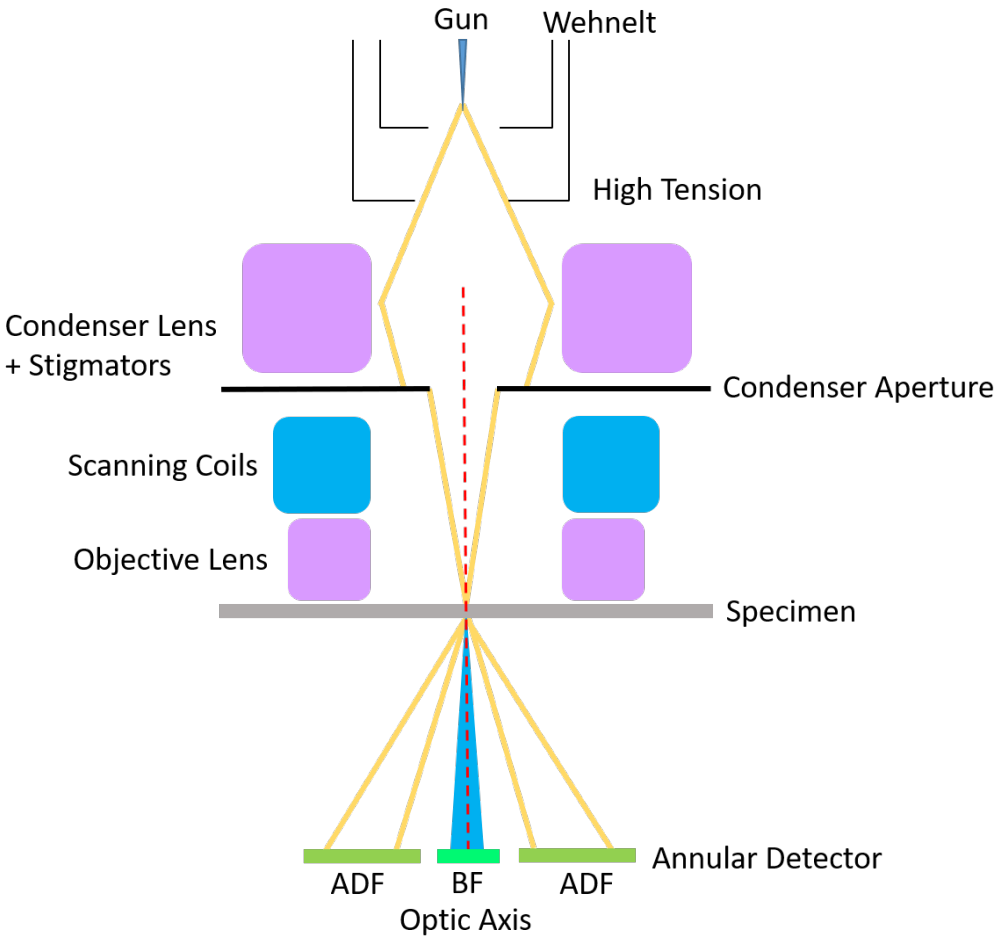

Figure 4.9: A schematic of the STEM instrument indicating the beam trajectories for forming the probe as well as the position of the detectors, viewed in cross section.

The microscope design is similar to that described in 4.1 however some modifications are made to allow the scanning of a focused electron beam. The interaction

of electrons with a specimen in STEM is different to TEM, wherein a specimen area is exposed to the parallel electron beam generating an image from transmission, scattering and interference of electrons as they pass through the exposed specimen area. The STEM technique instead focuses an electron beam, forming an electron probe, on to a specimen. Electrons forming this probe are scattered by a small area of the specimen. By decreasing the spatial width of the probe, smaller specimen features can be observed. The schematic in figure 4.9 illustrates the principle optics and components that an instrument comprises. As described in the previous sections regarding TEM, the top of the microscope houses the electron gun, typically of Cold-FEG type on modern STEM instruments due to the high electron coherence and intensity that Cold-FEG filaments provide. The first lens electrons interact with is the condensor lens. In early generation STEM instruments, the job of the condensor lens is to focus the beam into a probe on the sample. In modern STEM instruments the objective lens is used to further focus the probe after the electron beam is process by a probe corrector that is used to correct higher order spherical and chromatic aberrations, alongside stigmators to correct first order aberrations in the beam and improve spatial resolution.

Prior to the beam entering the objective lens it is influenced by a set of scanning coils. These are responsible for scanning the beam probe across an area of the specimen resulting in magnification by making the scan area smaller and increasing the magnetic force at the projector lens, hence the need to confine the probe width to improve spatial resolution. Manual alignment of the STEM is completed by altering the shape of the Ronchigram, which is a projected image or pattern formed in the diffraction plane. The shape and symmetry of the Ronchigram inform the user of the aberrations and astigmatism that need correcting.

Electrons scattered by the specimen are collected on a bright field (BF) detector and an annular dark field detector (ADF) depending on the angle of scattering. The angular ranges for the collection of scattered electrons on to these detectors are ≈0-20mrad for BF detectors while ADF detectors are capable of accepting scattering angles between 70-200mrad, including High Angle ADF (HAADF) range. An image is formed by recording the intensity of electrons incident on a detector as a function of the beam probe position within a scanning area. The scattering angle depends on a number of factors comprising the atomic number of elements in the specimen, the thickness of the specimen and the crystallinity of the specimen.

The HAADF imaging paradigm is also referred to as Z-contrast imaging and as a result has become a popular technique for measuring the structural properties of materials [106, 107]. HAADF imaging was developed around ADF due to diffraction contrast in images acquired with ADF detectors, which complicated image analysis and as a result the inner radius of the ADF detector was increased to reduce the intensity of electrons contributing to diffraction contrast in an image. The contrast in HAADF imaging is dominated by mass contrast from incoherently scattered electrons. At high magnification, resolution in HAADF imaging can be improved from channeling in the specimen. The coulomb interaction of electrons with atomic columns channels electrons between columns, mitigating beam broadening and improving resolution.

There are of course multiple factors that contribute to features in STEM and TEM BF and DF images. The main factors responsible for contrast in an image are Amplitude and phase contrast. Amplitude contrast comprises mass-thickness contrast and diffraction contrast. The TEM specimen preparation processes described above are rarely able to create a specimen with uniform thickness, although specimen preparation by FIB produces specimens that are more uniform in thickness than specimens prepared by conventional polishing methods. Electrons passing through thicker regions of a specimen are scattered more. The result is the same for electrons scattered from heavier elements. Higher atomic number elements exert higher coulomb force on electrons, increasing the scattering angle. Scattering from nuclei can be described by Rutherford scattering, resulting in incoherent scattering of electrons. High angle scattering produces contrast in an image at any magnification. In a TEM this contrast can be enhanced by using an aperture, which eliminates electrons scattered at high angles, increasing the contrast in an image. Diffraction contrast occurs from variations in the crystalline uniformity of the specimen, such as bend contours. Bragg scattering contributes to imaging due to scattering at defined Bragg angles. Isolating a scattered electron beam at Bragg angles with an objective aperture is how TEM DF images are formed. The diffraction from planes creates the conditions for Bragg diffraction therefore by isolating the scattered beams the image is formed by only the electrons scattered from the crystal features that establish the condition for Bragg scattering. Diffraction contrast is a result of coherent elastic scattering.

Phase contrast is also present, and is a major component of the contrast observed in HRTEM images. It is sensitive to many factors such as specimen thickness,

orientation, scattering factor, focus and astigmatism of lenses, particularly the objective lens. Phase contrast is prevalent whenever fringes are observed. As described by Fraunhofer and Fresnel diffraction of light, the scattering of electrons through a crystal is analogous to diffraction through an array of slits where the atomic structure determines the slit width and diffraction pattern shape that is formed due to the interference of electrons. The relative phase differences of electrons scattered and transmitted through the specimen combine, resulting in an image formed from both diffracted electrons and transmitted electrons. Small differences in phase of electrons hitting the screen result in small changes in contrast. Therefore phase contrast may enable resolution of small features but the image recorded is a convolution of transmitted and diffracted electron beams. Atomic resolution imaging in HRTEM is therefore described by phase contrast and requires image simulations and diffraction patterns to be measured in order to identify the stoichiometry of a specimen. Other examples of phase contrast comprise Fresnel contrast, observed in the over focus and under focus conditions when imaging due to near-field optic conditions between the specimen and the objective lens, and Moiré patterns that may occur due to dislocations within the specimen. Even at low magnifications Moiré patterns can be observed from which information about the crystal structure can be determined. On the face of it, HAADF STEM images are easier to interpret than HRTEM because of the multi-component contrast observed in the TEM.

However, to accurately determine the structure of specimens observed in HAADF STEM, image simulations and, where appropriate, DFT calculations of interface and defect structures are still required. The STEM image simulation package used in this work is QSTEM [108], which uses multislice methods, such that a slice comprises an atomic plane, to model the scattered trajectories of electrons passing through each plane in the specimen and create an image based on parameters comprising the detector acceptance angles and microscope gun and lens variables.

QSTEM simulations conducted as part of this project were setup using CrystalKit software to build atomic models of the interfaces that include atom size, crystal space group and lattice spacing parameters. Once interface model is built, simulation parameters are specified in the QSTEM graphical user interface. This user interface enables selection of a region of the model for simulation and setting of parameters for simulation such as beam energy, sample thickness, lensing and detector size parameters and optionally allows for thermal diffuse scattering. QSTEM simulations in this project were performed for 200 x 200 pixel images with a detector angle between

100-200mrad and beam energy, focussing and astigmatism parameters recorded from the microscopes used.

4.5 Advances in sample analysis with TEM

To improve resolution, in both TEM and STEM, a dedicated aberration corrector is used like a convex lens to separate and then re-converge the electrons to a point to remove focusing problems from aberration effects. Positioning the corrector within the condenser lens enables probe correction while positioning of the corrector below the objective lens enables image correction typically for STEM and TEM aberration correction respectively. The addition of ancillary instruments to the electron microscope also enables spectroscopy of the specimens to further quantify the chemical structure if the specimen. Such examples of these in situ spectroscopic techniques are Energy Dispersive X-ray spectroscopy (EDX) and Electron Energy Loss Spectroscopy (EELS) wherein the latter is used in STEM where electrons from the beam probe scatter from atoms in the specimen they lose energy, characteristic of the quantised electron energy levels within the atomic structure of the specimen.

This overview of Transmission Electron Microscopy is brief however it details the relevant information required to understand the results presented in later chapters acquired with both STEM and TEM instruments. The work of Williams and Carter provides extensive detail into the physical processes inside the microscope [105].

Chapter 5

Methods of simulating electronic structure and properties of materials

While experimental methods are capable of characterising the properties of materials, our understanding of the physical properties needs to be reinforced and as modern computing has advanced, theoretical calculations have become increasingly more accurate and more efficient. These calculations of physical quantities are known as first principles calculations, which start with an understanding of what is known about condensed matter systems. The calculation therefore starts with atoms in an array and considers electrostatic potentials of electrons and atomic nuclei in the system. By simulating different arrangements of atoms of different elements, the electronic band structure of uncharacteristic stoichiometries can be predicted. Therefore the electronic properties of defects in a crystal can be predicted and develop further understanding of materials beyond pure experimental analysis. The most widely used method of modelling material properties at the nano-scale is Density Functional Theory (DFT). Implementation of DFT has become popular for the efficiency and accuracy it offers. The accuracy of these simulation codes are developing as predicting potential functions improves. The subsequent sections of this chapter will discuss two particular codes used in the work presented in this thesis.

5.1 Density Functional Theory (DFT)

Modern quantum mechanics has pioneered materials research. A total energy functional provides information on the electronic structure of a crystal, however solving the Hamiltonian for each electron in a large structure (≈100 atoms) is inefficient and the time for a calculation scales proportionally with each electron added to the system. A major step was taken to streamline the calculation time for these quantum mechanical systems by Hohenberg and Kohn [109]. Their method calculates the electron density that minimises the total energy functional corresponding to the ground state of the system. Therefore the total energy functional does not need to be determined for each electron individually. However this simplification results in a total energy functional that is incomplete. The total energy functional comprises a kinetic energy term, external potential terms, a Hartree term; due to Coulomb interactions between electrons, and an exchange-correlation term. It is this last term that is non-specific in DFT calculations, however there are ways of modelling the interactions of electrons together.

Two of the most accepted approaches to modelling exchange correlation are Local Density Approximation (LDA) and Generalised Gradient Approximation (GGA) [110, 111]. LDA assumes that the local exchange correlation is concurrent with that of the uniform electron gas and as a result this approach prefers to smoothly vary the electron density [111]. GGA on the other hand realises that the exchange correlation is not simply effected by the local electron density alone but also the gradient of the density. As a result, GGA is more capable of correcting for inhomogeneities in the electron density [112].

Many DFT codes only model valence electrons and collate core level electron interactions with atomic nuclei as pseudo-potentials. This assumes that the effect of valence electrons on core level electrons is minimal and interactions of core level electrons with atom nuclei generate a potential that affects the valence electrons. The reason for this approximation is that the strong potential exerted by nuclei on the core level electrons introduces high oscillatory wave functions which are undesirable when using the approximations for the electron density described above. The pseudo-potential approach is valid because a majority of material properties depend on the behaviour of electrons outside of the atom core.

Further validity of the pseudo-potential approach is the requirement that the pseudo-potentials must be transferable and reproduce accurate valence wave functions

in other materials. Therefore this approach has the advantage of significantly reducing the number of electrons required for a calculation, which in turn reduces the cost of performing a calculation.

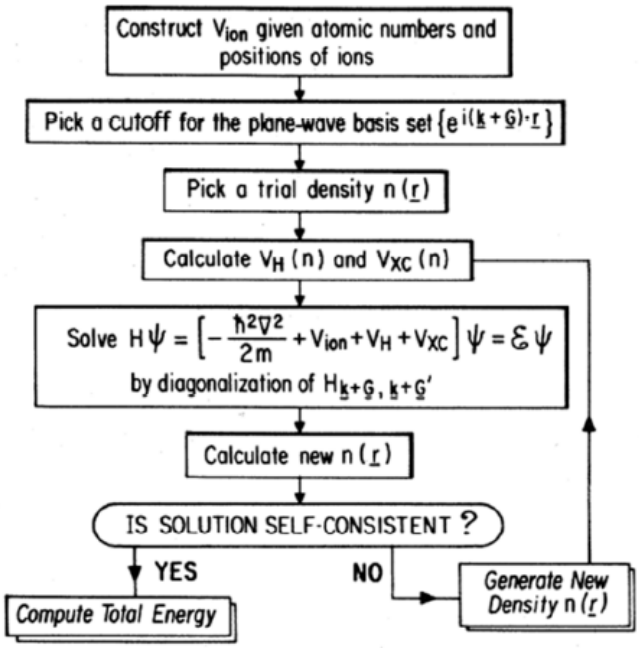

Figure 5.1: A flow chart of the computational process conducted to calculate the total energy of a material [113].

An electron density can be determined using the pseudo-potential approach. This trial energy density is valid up to a predetermined energy cut off established by bonding strength in the material. The trail density is then used to determine the Coulomb potential and exchange correlation potential, which are inserted into the Hamiltonian, as wave functions determined from Kohn-Sham equations, and a new electron density is calculated. If the output electron density is concurrent with the input electron density up to a preset error value then the density is accepted and used to calculate the total energy. This process is described in Figure 5.1.

5.1.1 CASTEP

In CASTEP, algorithms are implemented that can extemporaneously calculate pseudo-potentials for each chemical element and there are also libraries with pre-determined pseudo-potentials. These pseudo-potentials are geometry optimised in CASTEP by an iterative process to determine the lowest energy state of the system. Geometry optimisation can be done with or without atomic position constraints. CASTEP implements the Broyden-Fletcher Goldfarb-Shanno (BFGS) algorithm for the geometry optimisation process [114]. Geometry optimisation is essential when studying material interfaces because epitaxy at the interface can effect atomic positions. Any residual external forces due to interfacial strain can be observed as a linear dipole field contribution to the energy band calculation. The geometry optimisation aims to neutralise external forces on ions in the crystal. This calculation is the most costly part of a simulation.

Once ionic positions have been optimised, a map of energy levels for reciprocal lattice vectors of a crystal can be produced. This is known as the band structure, plotted in 2D by projecting chosen reciprocal lattice vectors on to the x-axis of an energy band diagram. The lines that form correspond to electron orbitals and the shape of the lines provides insight into bonding of valence electrons in the crystal. Parabolic bands are consistent with free electron approximations while flat bands indicate electrons that are localised. The pseudo-potentials and wave functions that are determined using CASTEP can be fed directly in to a program called OPTADOS that calculates the LDOS or "partial" density of states (PDOS) for a system. When studying material interfaces, this map of electron energy levels across reciprocal space represents the Local Density of States (LDOS). The total density of states will not provide information on interface electronic states. LDOS allows simulation of specific crystallographic regions, atomic sites and layers. Layer-by-layer simulations have been conducted in this thesis, as can be seen in chapter 8. Using LDOS calculations, the energy position of the valence band maximum as a function of distance from the interface between materials can be determined. By this method, CASTEP has been used in this work to simulate the valence band offset for different terminating layer atom configurations. This makes DFT, and CASTEP due to the built-in features described above, a powerful tool for understanding the properties of material interfaces.

5.1.2 *flair*

As mentioned in an earlier section of this chapter, costs can be saved by approximating core electrons and nuclei into pseudo-potentials due to the periodicity of crystals. However, there are still benefits to implementing all electron codes for DFT calculations. The main advantage of all electron codes are their ability to improve the calculation of the exchange-correlation potential because such codes have to accurately account for a 1/r singularity generated by potentials of the nuclei when using a plane wave basis set to model a material system [115]. The 1/r singularity results in an extremely slow convergence of the calculations for electrons close to nuclei, which makes calculations costly. This is not an issue for simulations that use pseudo-potentials to represent core level and nuclear potentials because of the smoothing functions described earlier in this chapter, however this results in the iterative approach to determine the charge density that introduces error into the calculations.

Therefore, Augmented Plane Wave (APW) concepts were introduced to accurately model the 1/r singularity. This approach distinguishes atomic sites from interstitial sites and models muffin-tin spheres at atomic sites that do not overlap with each other, with the remaining crystal volume described by plane waves. Inside the muffin-tin spheres, the electrons are modelled by spherically symmetric functions that are also consistent at the boundary of the sphere with the interstitial plane wave functions. While this concept addresses convergence problems with the 1/r singularity, the complexity of the calculation means that the resultant Hamiltonian cannot be diagonalised to determine the band structure of a given energy but instead each energy must be fixed in order to determine the reciprocal lattice vector solutions one by one.

In an attempt to fix the Hamiltonian diagonalisation issue, the functionals inside the spheres were supplemented by their derivatives to create a Linear APW (LAPW) approach wherein radial basis functions are replaced by a Taylor series. This method removed the energy dependence of the Hamiltonian that was a concern for earlier APW methods. However, this method introduced a quadratic error dependent on deviations in the potential. Therefore, further improvements could be made to simulating ionic potentials by this method, which led to the development of Full-potential Linear Augmented Plane Wave (FLAPW) simulations, as implemented in the simulation package *flair*. The concept utilised in FLAPW is that constraints on the shape of the atomic site muffin-tins and the constant interstitial potential are relaxed. This

accounts for non-spherical functionals in atomic sites as well as variations in the potential in interstitial regions.

Due to the periodicity of crystal structures, once the potential for one atom has been determined, it must be the same for the same atoms in the crystal. Extrapolating the potential for atoms of the same type over the whole crystal to be simulated results in a Hamiltonian comprising two components, a muffin-tin component and an interstitial component. Once the electron densities for these regions are calculated, the Coulomb and exchange-correlation potentials can be determined. To streamline determination of the Hartree component of the Coulomb potential in the interstitial region, a pseudocharge method is implemented [116]. This separates the calculation into further interstitial and vacuum components, the result of which is a more rapidly converging calculation. Following the structure of a DFT calculation, the exchange correlation potential can then similarly be determined by separating the interstitial and vacuum regions that can be calculated independently of each other because exchange correlation potentials are localised.

Separation of the electronic structure into muffin-tin, interstitial and vacuum regions has further enabled FLAPW to be implemented for different crystal geometries, such as bulk and thin film structures. The FLAPW methods implemented in *flair* therefore enable simulations for density of states, band structures and density plots for bulk and thin film crystal structures [115, 117–119]. Examples of such results are presented in chapter 7.

Chapter 6

Preparation of SiC surfaces

6.1 Introduction

In order to prepare epitaxial thin films interfaces and therefore measure properties of a subsequently formed heterojunction, the substrate surface needs to be prepared. This chapter introduces the surface structure of 6h-SiC(0001). There are over 250 polytypes of SiC and it would be beyond the requirements of this thesis to disclose the surface properties of them all, however when considering the surface properties and reconstructions of 6h-SiC(0001), some of these properties may also exist for other polytypes, notably 4h-SiC(0001) and 3C-SiC(111) surfaces. The 6h-bulk stacking sequence is described in the introduction to this thesis, however the surface structure of 6h-SiC(0001) is not yet described. The 2D arrangement of atoms on the 6h-SiC(0001) surface is shown in figure 6.1 where the unit cell of the surface is constrained by the black lines creating a small diamond shape in the image. The in-plane atomic distance between atoms linked by the black lines is 3.07Å. In this chapter both Si and C terminated surfaces will be considered and the origins for the surface reconstructions of each termination will be reviewed from the literature

When studying surface reconstructions, samples are analysed under UHV conditions. The methods that are used to characterise the structure of surface reconstructions are described briefly herein and comprise Low Energy Electron Diffraction (LEED) and Reflective High Energy Electron Diffraction (RHEED). These surface electron diffraction techniques are discussed in detail in Chapter 2.

Firstly, Si terminated surface structures will be discussed, followed by the process of hydrogen etching SiC surfaces. C terminated SiC surface reconstructions will

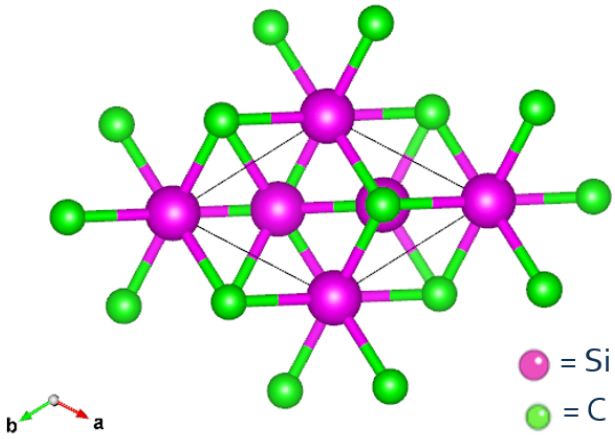

Figure 6.1: A crystal model of the 6h-SiC(0001) surface produced using the software package VESTA. The colour code used in this figure is the same as that used for the 6h structure in figure 1.2.

not be discussed in detail in this chapter. Synthetic SiC wafers were historically prone to defects, resulting in rough surfaces making them unsuitable for epitaxial interface studies, however in recent years manufacturing of SiC wafers has progressed and improved the micro-pipe dislocation density as well as the surface roughness with the addition of epilayers. This chapter will also consider experimental results from SiC surfaces prepared in this work in parallel with results reported in the literature.

6.2 Si terminated 6h-SiC(0001) surfaces

When discussing Si and C terminated surfaces they can also be described as the (0001) and (000$\bar{1}$) surfaces respectively. While the preparation processes on (0001) surfaces can lead to either Si or C termination, the (000$\bar{1}$) surface will, within the scope of this thesis, always be C terminated. The reasons for this will become clear throughout this chapter. At this point it would be appropriate to introduce the general concept of surface reconstructions.

As discussed in the introduction to this thesis, when the bulk structure of a crystal is terminated, in this case on a semi-infinite scale where the ratio of surface area to volume is high, a frozen bulk termination of the crystal can be imagined for the surface structure of the terminating face. In this picture of the frozen bulk termination we can imagine an array of dangling bonds across the surface leading to a surface charge density that is unbalanced from the bulk making these surfaces energetically unfavourable. In UHV conditions the frozen bulk structure can almost be realised since very few atoms or molecules are present in the system to saturate the dangling bonds.

Therefore under such conditions surface reconstructions both stable and metastable can be observed. Factors such as temperature and terminating crystal plane will affect how a surface reconstructs. In UHV conditions, dangling bonds are energetically unfavourable and as a result, with temperature or otherwise, the structure at the surface may change to saturate some or all of these dangling bonds. This is conducted within the selvedge; the top few planes of the crystal proximate the surface. It is within this region that changes in surface atomic configuration can result in changes to electronic structure, as described in the case of polar surfaces and interfaces in the introduction to this thesis. Therefore it is important to understand the platform that the thin film growth will start from on the substrate surface.

6.2.1 The $\sqrt{3} \times \sqrt{3}$ - R30° reconstruction

The first of the 6h-SiC(0001) surface reconstructions to discuss is the $\sqrt{3} \times \sqrt{3}$-R30° surface. The naming of the surface comes under wood notation and describes the translation of the bulk in-plane lattice vectors required to form the surface reconstruction. In this case the surface lattice spacing is $\sqrt{3}$ times larger than the bulk lattice spaceing and rotated by 30° from the bulk lattice vectors. Figure 6.2 illustrates the $\sqrt{3} \times \sqrt{3}$-R30° reconstruction and its relationship to the bulk.

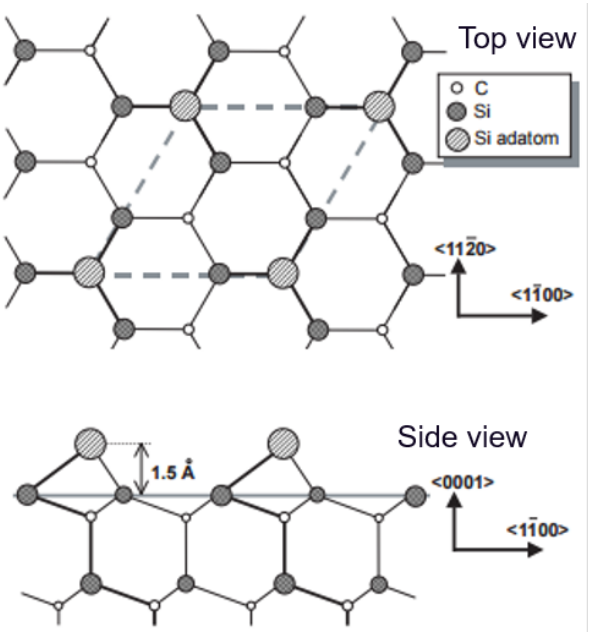

Figure 6.2: A model of the $\sqrt{3} \times \sqrt{3}$-R30° reconstruction over the underlying bulk structure both viewed from above (top) and from the side [120].

The reconstruction described by figure 6.2 shows how Silicon atoms are arranged to reduce the number of dangling bonds on the surface. The model produced by Fujino et al. [120] shows the surface Si atoms tetragonally bonded to subsurface atoms with just one unsaturated bond remaining per surface Si atom. The tetragonal site sits over a first subsurface carbon atom. Another atomic site predicted for this surface was the hexagonal site, positioned over a further subsurface carbon atom however both theoretical calculations and STM experiments confirmed that the tetragonal site was preferred reducing the surface energy of 6h-SiC(0001) [120–122]. The tetragonal and hexagonal sites are termed T_4 and H_3 respectively. The differences in position of the two sites on the surface is shown in figure 6.3. This model also supports the features observed by RHEED that will be discussed in chapters 7 and 8.

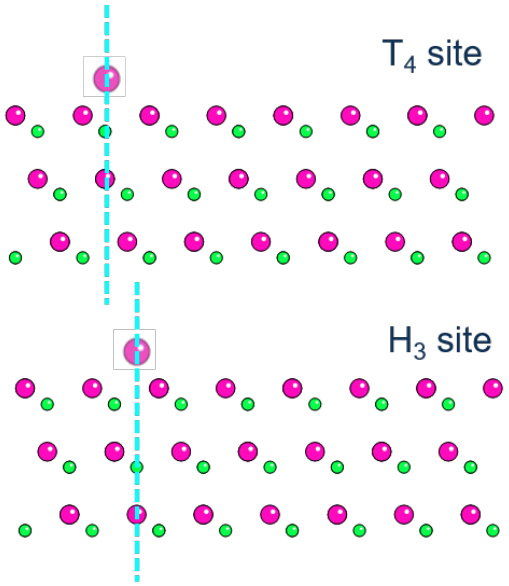

Figure 6.3: A model showing the atomic position of an Si atom in the T4 site (top) and H3 site (bottom), viewed in cross-section. Si atoms are pink while C atoms are green.

Since there is a single dangling bond left per atom on this surface this surface may still be sensitive to changes in the local chemical potential. An example of this would be a change in atmosphere or the presence of contaminants. When Si is exposed to atmosphere SiO_x starts to form. This process also occurs on SiC and can form a silicate adlayer reconstruction based on the $\sqrt{3} \times \sqrt{3}$-R30° where an oxygen atom bonds to the remaining dangling bond of this surface reconstruction [123–125]. This adlayer is notoriously difficult to remove from both Si and SiC. Methods of preventing the oxide adlayer formation will be discussed within this chapter.

An alternative means of saturating dangling bonds on surfaces would be to add more material. Adsorption and desorption of material on surfaces is the premise behind catalysis however by working in UHV conditions the species adsorbed can be controlled. An example of this is the oxidation of Si at the surface.

6.2.2 Preparation of 6h-SiC(0001) surfaces by Hydrogen etching

Hydrogen etching of substrates is a well founded technique for preparing atomically flat surfaces. Typically the etching is applied in the form of HF or buffered-HF [126]. One problem with using HF is that it is dangerous to handle and as a result experimentalists have turned to etching with hydrogen gas in a remote environment. Only a small amount of hydrogen gas is required resulting in miniscule amounts of hydrogen gas being exhausted from a system. Most substrate materials have a reason for being etched and for SiC there are two main reasons for treating the surface with hydrogen. The first reason is the removal of silica that can form when SiC surfaces are exposed to air and the second reason is to remove excess carbon from the surface when annealing SiC at high temperatures. The latter becomes necessary when trying to maintain a Si terminated surface at high temperatures. High temperatures are required to remove stubborn hydrocarbons and oxygen atoms. Above 850°C Si will desorb from SiC but carbon will remain. It is this process that allows graphitic layers to form on the SiC surface and, under certain conditions, establish epitaxial graphene [127]. Substrate preparation methods described in the literature describe how to process SiC substrates with molecular hydrogen. These methods comprise annealing in separate systems (ex-situ) or annealing within the same system, for example in the same system that is used for MBE growth (in-situ).

A popular experimental setup for preparing SiC substrates by hydrogen is using a tube furnace. Some tube furnace materials vary but the principle is the same. The furnace used for this work comprises an Al_2O_3 tube heated by an electric heater. Gas lines can be integrated to provide flow inside the tube either in static confinement or dynamic flow using valves within the furnace. The furnace described is capable of heating the tube up to 1500°C. Early annealing experiments with hydrogen etching of SiC required heating substrates to over 1500°C under 1 atm of molecular hydrogen gas pressure. The high temperature causes hydrogen molecules to dissociate and the formed hydrogen atoms bond with C on the SiC surface to form hydrocarbons. Desorption of hydrocarbons compensates Si desorption at the same elevated temperature [128–131].

This method is not always successful and reports from the literature show that the hydrogen etching can be too aggressive creating rough surfaces with pits and holes on the surface [129, 132]. These pits and holes are considered to be a sign of

incomplete etching in the report by Ramachandran et al. Similar results were obtained when preparing substrates for this work with a tube furnace. Due to limited control of parameters and atmospheric composition within the tube furnace, the decision was made in this work to prepare samples in-situ by preparing the 6h-SiC(0001) surface with hydrogen provided from a hydrogen cracker as described in chapter 2. Improved surface etching has been reported from the use of atomic hydrogen in HV thanks to reduced contamination and improved hydrogen cracking efficiency from using a hydrogen cracker [133, 134].

In the results presented in this thesis the above methods were combined, providing molecular hydrogen to 6h-SiC substrates heated to >800°C. The total pressure measured by the ion gauge in the UHV system during hydrogen exposure read 5×10^{-8} mbar. The local pressure at the sample is higher because the sample is in close proximity to the hydrogen source and the ion gauge is not calibrated for hydrogen. A correction factor should be applied to the ion gauge reading. Attempts to prepare samples by atomic hydrogen etching using a gas cracker were made however the SiC surface formed was not consistent. The background pressure in the chamber also rose considerably when operating the gas cracker, increasing the risk of contaminating the SiC surface.

6.3 Results

Figure 6.4 shows a RHEED pattern obtained for the 6h-SiC as it came out of the box, without undergoing any surface processing. Although kikuchi diffraction and both ZOLZ and FOLZ are observed in these RHEED patterns indicating surface order, the absence of streaks indicates the presence of surface roughness.

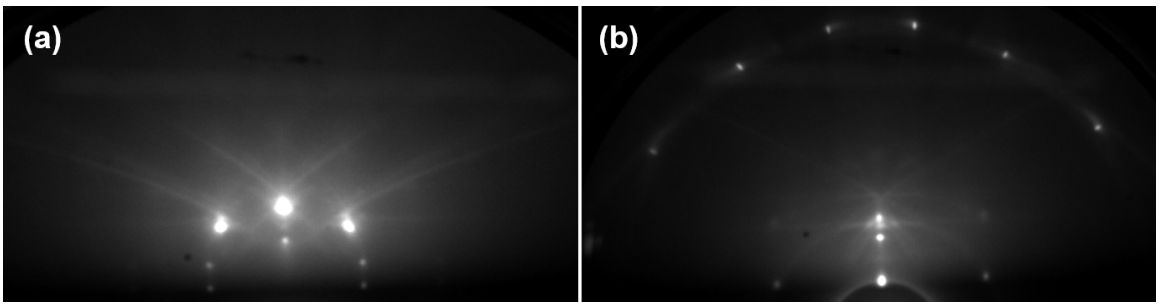

Figure 6.4: (a) A RHEED pattern recorded for diffraction from an out-of-the-box sample surface with incident beam along <11$\bar{2}$0> crystal zone axis. (b) A RHEED pattern recorded for diffraction from an out-of-the-box sample surface with incident beam along <1$\bar{1}$10> crystal zone axis, with the First Order Laue Zone (FOLZ) visible around the edge of the screen.

After preparing the same 6h-SiC sample at 900°C and 5×10^{-8} mbar molecular hydrogen pressure, as measured by an ion gauge, the sample surface flatness improved based on RHEED patterns recorded. These results are displayed in figure 6.5. Streaks are now clearly visible after 30 mins exposure to molecular hydrogen at elevated temperature. The streaks indicate that there is both long range order and that the surface is flat.

LEED conducted on the SiC sample after hydrogen treatment shows a pattern indicative of a $\sqrt{3}\times\sqrt{3}$ - R30° surface reconstruction. Looking at the pattern in figure 6.6 obtained at incident beam energy of 104.3eV, the inner most spots correspond to the reconstruction that are 30° rotated with relative to the main brighter spots. Spots are positioned at $\frac{1}{3}$ the radial distance of the main spots due to the conversion of the real space to reciprocal space in diffraction. The sharp spots and low background intensity indicate a flat surface with long range surface order.

The final figure of this chapter shows results from Scanning Electron Microscopy (SEM) of the surfaces of two samples. One of which has been prepared with hydrogen treatment at 900°C while the other has been heated to 900°C under UHV without

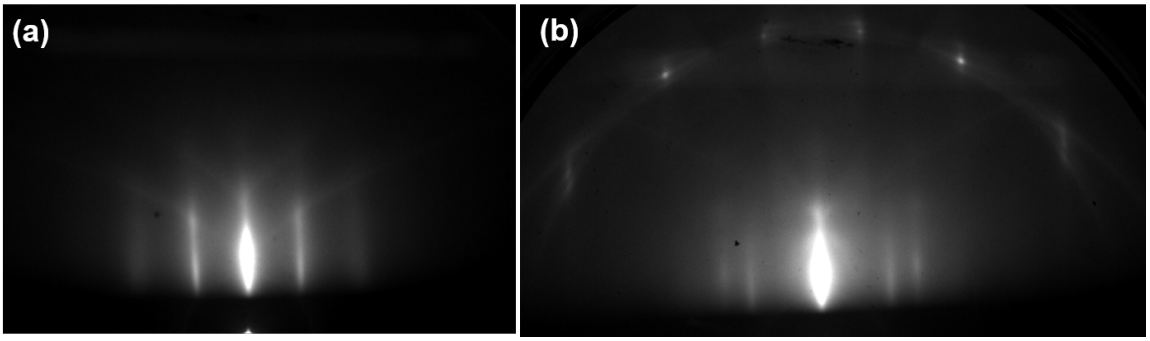

Figure 6.5: (a) A RHEED pattern recorded for diffraction from a 6h-SiC(0001) surface after treatment with hydrogen at 900°C with the incident electron beam along <11$\bar{2}$0> crystal zone axis. (b) A RHEED pattern recorded for diffraction from a 6h-SiC(0001) surface after treatment with hydrogen at 900°C with the incident electron beam along <1$\bar{1}$10> crystal zone axis, with the FOLZ visible around the edge of the screen.

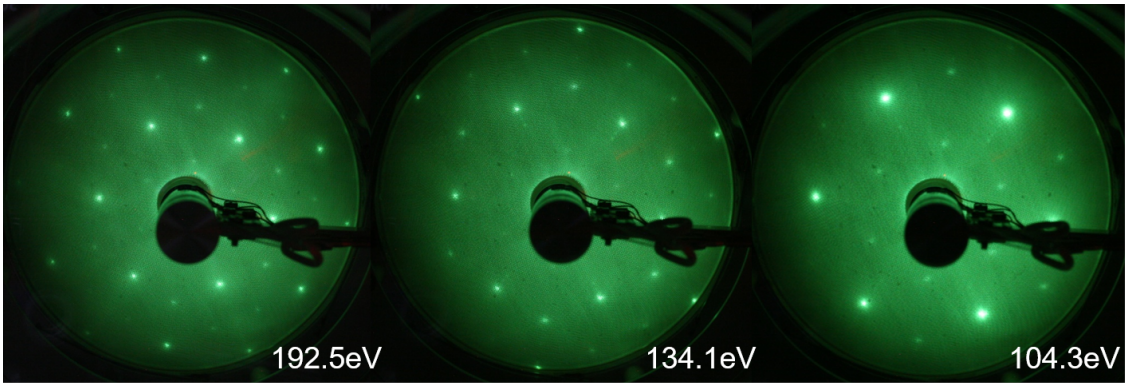

Figure 6.6: A series of LEED patterns acquired at 192.5eV 134.1eV 104.3eV from the scattering of electrons from a 6h-SiC surface prepared with hydrogen at 900°C. The Wehnelt potential and filament current are kept constant throughout the energy range, therefore any relative variations in intensity are due to properties of the sample.

hydrogen. Both films imaged are coated with MgO thin film however the growth conditions are identical and at low thickness will not affect the terrace structure observed for the underlying substrate. After all, the primary beam potential used in the SEM is 5kV, therefore secondary electrons are escaping from more than a few nm below the surface. However, features observed within terraces in figure 6.7 are properties of the MgO thin film surface. Such features are discussed in Chapter 7. Note the different terrace directions are due to different sample orientations, the terrace direction follows the same crystallographic direction in both samples. The main result displayed here is that the step edges are sharper for the sample prepared with hydrogen, figure 6.7a,

compared to the step edges for the sample prepared without hydrogen, figure 6.7b. The differences in brightness and contrast between the two SEM images do not indicate any differences chemically or otherwise because the brightness and contrast are constantly being adjusted when imaging, particularly at high magnifications, however figure 6.7a is acquired with a lower secondary electron detector, while the image in figure 6.7b was acquired with a secondary electron detector mounted inside the SEM column. This only affects the resolution achievable between the two images, because the sample is at a shorter working distance in 6.7b. Despite the differences in step edge sharpness, both samples exhibit ≈180nm wide terraces.

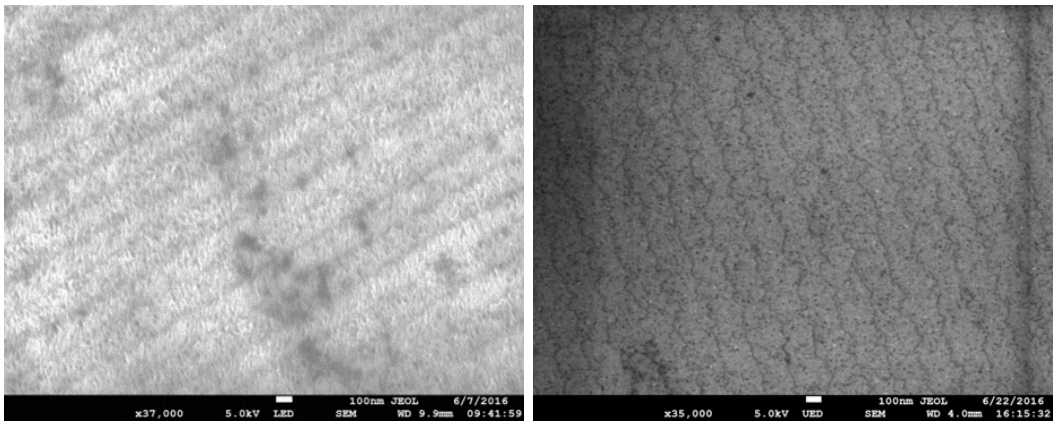

(a) (b)

Figure 6.7: SEM images of samples where (a) the SiC surface has been prepared with hydrogen and (b) the SiC surface has been prepared without hydrogen. The differences in the brightness do not indicate any differences between the samples.

6.4 Conclusion

In summary, hydrogen etching of SiC(0001) surfaces reduces surface roughness and sharpens step edges, as reported in the literature and discussed herein. Hydrogen etching of the SiC surface using molecular hydrogen produces surfaces comparable for those produced in ex-situ environments and provides the added benefit of minimising contamination of the SiC surface prior to subsequent thin film deposition. Surface electron diffraction patterns show significant improvement in flatness of the substrate by hydrogen etching.

It is still unclear whether further improvements can be made using atomic hydrogen from a hydrogen cracker rather than molecular hydrogen. One advantage of atomic hydrogen is enhanced silicon removal resulting in silicate removal at reduced temperatures. The upcoming chapters show further improvements in SiC surface preparation using the same in-situ molecular hydrogen surface treatment. These chapters will also cast light on the surface and interface structure of samples exhibiting the $\sqrt{3}\times\sqrt{3}$ - R30° reconstruction and the impact that this structure has on the electronic properties across the interface of MgO/SiC hetero-structures.

Chapter 7

MBE growth of polar MgO thin films

7.1 Introduction

This chapter aims to review results from literature on MgO(111) MBE growth conditions and apply first principles modelling to MgO growth methods. As discussed in the introduction to this thesis, MgO is of interest for potential device applications with 6h-SiC, however the polar structure along the (111) crystallographic orientation of the rock-salt structure introduces potential problems with preparing MgO thin films because of the predicted polar catastrophe [45, 46, 48] where the structure of alternating anion-cation planes creates electric polarisation in the MgO unit cell that leads to a diverging electrostatic potential dependent on thickness. The polar compensation mechanisms discussed in the introduction to this thesis are considered again in this chapter and results reported show evidence of such compensation mechanisms.

First, experimental methods of preparing MgO(111) thin films are considered. There are reports of successful MgO(111) growth on metals and semiconductors via a number of methods, of which the main two are described in this chapter. MgO is an irreducible oxide and only forms one oxide structure; the rock-salt structure. Therefore, careful balance of magnesium and oxygen vapour is less critical than for other oxides such as iron oxides [135, 136]. However, sensitivity of the substrate to oxidation does need to be considered. In the first layer-by-layer growth method, a substrate is first exposed to magnesium to deposit a Mg layer, preventing oxidation of the substrate. Exposure to magnesium is then ceased and the layer is exposed to oxygen until the magnesium layer is covered by an oxygen layer and exposure of

the sample to oxygen is ceased. This alternating magnesium and oxygen exposure is then repeated to control layer-by-layer growth of MgO along the polar orientation [61, 63, 137]. The second method comprises MgO deposition under simultaneous exposure of magnesium vapour and oxygen vapour. This method still supports layer-by-layer growth but magnesium and oxygen atoms are competing for the lowest energy states on the sample surface. Results reported in literature for MgO thin films grown using this co-deposition technique show epitaxial film growth comparable with results reported for alternating magnesium and oxygen deposition [92, 138–141].

Simulations of the growth conditions described above have been conducted by collaborators of this work, the theoretical methods of which are discussed herein. The results of these simulations are then compared with experimental results of thin and thick MgO films grown by MBE.

7.2 Methods of thin film growth and simulation

This section details methods of simulating growth conditions as well as the details for preparing MgO thin films by MBE. First, methods of simulating layer-by-layer alternating growth are considered. Simulations of the energy of formation of an anion or cation layer is non-trivial for MBE growth, as common methods using a Gibbs free energy formalism to predict the stoichiometry of layers assumes the system is in thermal equilibrium, which MBE growth scenarios are not due to thermal reservoirs of material from the material sources used.

7.2.1 Simulating MgO growth

To simulate the formation of MgO(111) thin films, first principles calculations have been undertaken using a full-potential linearised augmented plane wave method (FLAPW) [117, 119] in the form of the package *flair* [118]. A Generalised Gradient Approximation (GGA) functional of Perdew-Burke-Ernzerhof (PBE) [111] is implemented in this package. This GGA functional is used to improve estimates of the exchange-correlation energy due to structural energy differences. The MgO growth models were calculated for 3×3 supercells and a single-atom-adding approach is applied where the energy cost of adsorbing an atom is compared with the energy cost of changing the surface stoichiometry. Each constituent element has a chemical potential, μ defined as the energy required to add a single constituent species atom

to the system. Values of the chemical potential used for μ_{Mg} and μ_O are the energy of metallic magnesium and half the energy of molecular oxygen respectively. The chemical potential used becomes equivalent to the adsorption energy. As a result the problem of describing layer-by-layer growth is solved by calculating the the adsorption energy of single magnesium or oxygen atoms at varying degrees of magnesium or oxygen layer coverage. For MgO(111) growth calculations of adsorption energy can be obtained for magnesium and oxygen atom adsorption on magnesium surface layers and oxygen surface layers independently. At this point effects of the polar MgO structure are considered. Results of these simulations are discussed later in this chapter.

The adsorption of hydrogen on the surface has also been proposed to act as a surfactant for polar MgO growth. The model for this hydrogen stabilised layer by layer growth mode was proposed by Lazarov et al.. A schematic of this growth process is shown in figure 7.1.

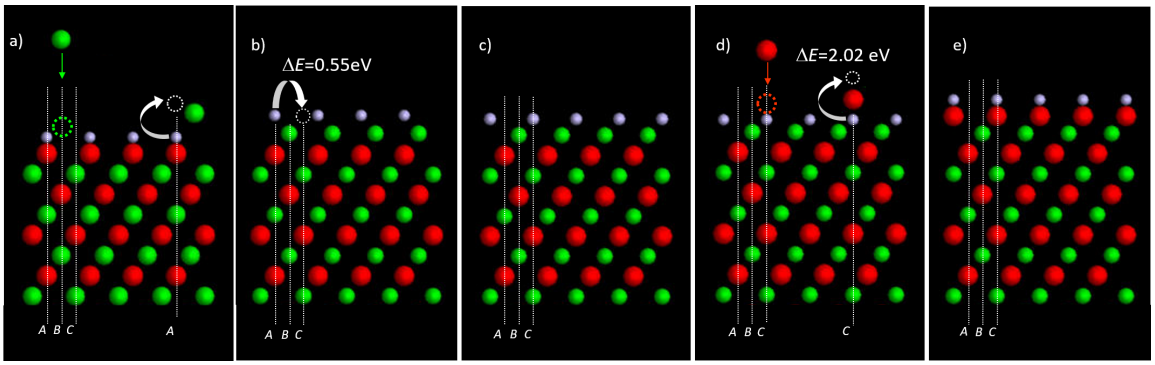

Figure 7.1: A model proposed for hydrogen stabilised MgO(111) growth. Hydrogen atoms are coloured grey while oxygen atoms are red and magnesium atoms are green. This figure was sourced from [142].

This model starts with a hydroxyl terminated MgO film in figure 7.1(a), wherein a Magnesium atom is incident on the surface. Forming a new magnesium layer in the B site is favourable over the hydrogen layer and therefore the neighbouring hydrogen atom is displaced. Figure 7.1(b) shows the system after a complete Mg layer has formed. There is also an advantage energetically for the hydrogen atoms to move to the C site shown in 7.1(c). Subsequent oxygen exposure reveals in figure 7.1(c) that it is energetically favourable to displace the hydrogen atoms again, even more so than in the case of Mg adsorption. Figure 7.1(d) shows the result after deposition of a layer of MgO that is hydroxyl terminated, as described at the start of the process. There

are results to support this model from research of hydroxyl terminated MgO(111) surfaces [57]. However, for films prepared for this work, the presence of hydrogen has not been confirmed from XPS measurements, discussed in chapter 8.

7.2.2 MgO(111) growth by MBE

MgO(111) thin films presented in this work were prepared using the aforementioned simultaneous deposition technique. Methods in the literature also disclose the use of oxygen in plasma form. Both plasma assisted MBE and MBE with molecular oxygen were conducted in this work, however the plasma conditions described in the literature are low power and throughout this PhD project no advantage was found for using oxygen plasma in place of molecular oxygen. There is, however, another parameter that has an impact on the quality of the quality of the thin films produced. Quality here refers to defect density and surface and interface roughness.

6h-SiC substrates were prepared in the MBE chamber by heating to 900°C under a flow of molecular hydrogen, as described in chapter 6. The base pressure of the system prior to starting hydrogen surface preparation was $<10^{-9}$ mbar in all experiments. The hydrogen cleaning process reduces surface roughness and sharpens step edges by saturating dangling bonds on the SiC(0001) surface. After preparing the SiC surface, by the methods described briefly above and in chapter 6, and conducting RHEED, MgO thin films are prepared under two different conditions, the results of which are discussed in this chapter. Parameters used for magnesium deposition from a Createc effusion cell are the same for both conditions. For the MgO(111) thin films presented in this chapter, the source was set to 280°C and the Mg flux of 10^{14} atoms cm^{-2} s^{-1} is monitored using a quartz crystal microbalance. Similarly, flow of oxygen to the system is constant between the two conditions measured with the ion gauge as 10^{-6} mbar total pressure in the system. Fluctuations in the oxygen content between experiments are minmised by monitoring the oxygen content in the chamber using a residual gas analyser. The difference in the two conditions is substrate temperature during deposition.

The results can be divided into high and low temperature results, where the high temperature results were acquired from samples prepared with a substrate temperature of 500°C while the low temperature results have been measured from samples prepared at 200°C substrate temperature. Following MgO deposition, all samples were analysed with RHEED and LEED in-situ before being removed from the system

for TEM specimen preparation by manual polishing [102]. The results from LEED, RHEED and TEM analysis are shown.

7.3 Results

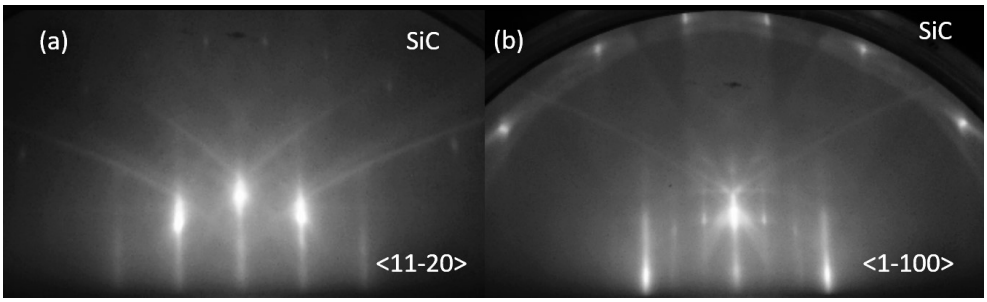

Figure 7.2: RHEED patterns representative of the SiC surface prepared for both high temperature and low temperature growth conditions. The patterns are obtained from diffraction with the beam aligned to (a) $<11\bar{2}0>$ and (b) $<1\bar{1}00>$ zone axes.

Preparation of the 6h-SiC surface in all cases results in the pattern shown from RHEED in figure 7.2. Here the $\sqrt{3} \times \sqrt{3}$ - R30° reconstruction is visible when the incident electron beam vector is parallel to the $<1\bar{1}00>$ crystal zone axis shown in figure 7.2(b) by streaks positioned at $\frac{1}{3}$ intervals between the main order streaks. The terminating atomic species on the surface cannot be confirmed by RHEED. The reconstruction could be Si terminated or be a silicate adlayer reconstruction described in chapter 6. Kikuchi diffraction and the first order Laue zone are observed indicating an ordered surface ensuring that the differences in MgO film quality are due to the different growth conditions and not the substrate surface.

RHEED patterns recorded for subsequent MgO growth on prepared SiC surfaces are shown in figure 7.3. RHEED patterns were recorded with the electron beam aligned to the same $<1\bar{1}0>$ zone axis for each sample. Figure 7.3(a) corresponds to diffraction from the surface of a MgO film grown at low substrate temperature, while figure 7.3(b) corresponds to diffraction from the surface of a MgO film prepared at high substrate temperature. The pattern from low temperature MgO film displays diffuse streaks showing some surface roughness indicated by gaps along the streaks, whereas high temperature MgO film displays sharp spots arranged along the positions expected for streaks on this surface, indicating greater surface roughness. Both cases exhibit high inelastic background intensity and Kikuchi diffraction and first order

Laue zones are not observed indicating that surface features are not periodic over large distances on the surface.

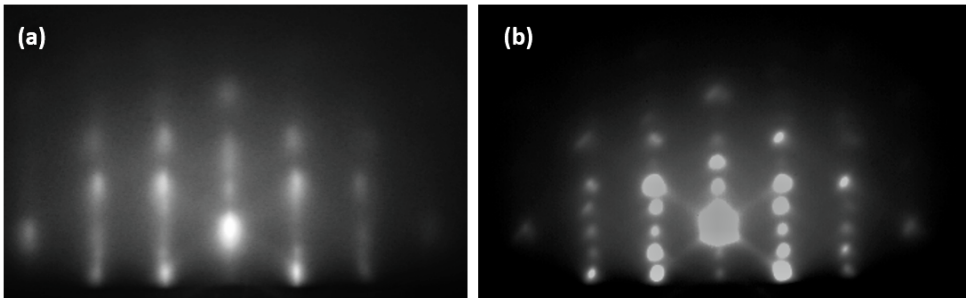

Figure 7.3: RHEED patterns acquired after MgO thin film deposition at (a) low temperature and (b) high temperature. Both patterns are acquired with the electron beam aligned to the $<1\bar{1}0>$ zone axis.

LEED was conducted on these MgO surfaces after deposition, providing further information on the surface structure. Figure 7.4 presents an array of diffraction patterns from the surface of a MgO film prepared at high substrate temperature. The array shows how the pattern changes with incident beam energy, ranging from 43eV to 118eV. A hexagonal pattern expected for the MgO(111)-(1x1) surface appears at 43eV, however when increasing the primary energy of the electron beam new spots start to form that are not positioned as expected for the MgO surface. Typically spots on the LEED screen will move toward the center point of the screen with increasing primary energy of the electron beam, however in this series as the beam energy increases the position of the hexagonal pattern is unchanged. Instead, the spots separate and converge with spots observed at the edge of the screen. This behaviour cannot be explained by diffraction from $\sqrt{3} \times \sqrt{3}$ or 2×2 reconstructions of the MgO(111) surface [57].

Polar surfaces are known to undergo large reconstructions of the surface to compensate electric polarisation in the structure. The first results from simulations using flair are presented to understand polar contributions that may affect the preferred stacking sequence in the calculations. For the case of Mg adsorption on an O-terminated surface with O occupying the A sites and the subsurface Mg atoms in C sites, adsorption of the first Mg adatom in the B site is preferred over the C site by 0.23 eV/atom at the start of Mg growth. This site becomes increasingly preferential to 8.2 eV/atom before reducing in preference to 2.3 eV/atom at a one-third and two-third Mg coverage, respectively. This shows that the system structure is

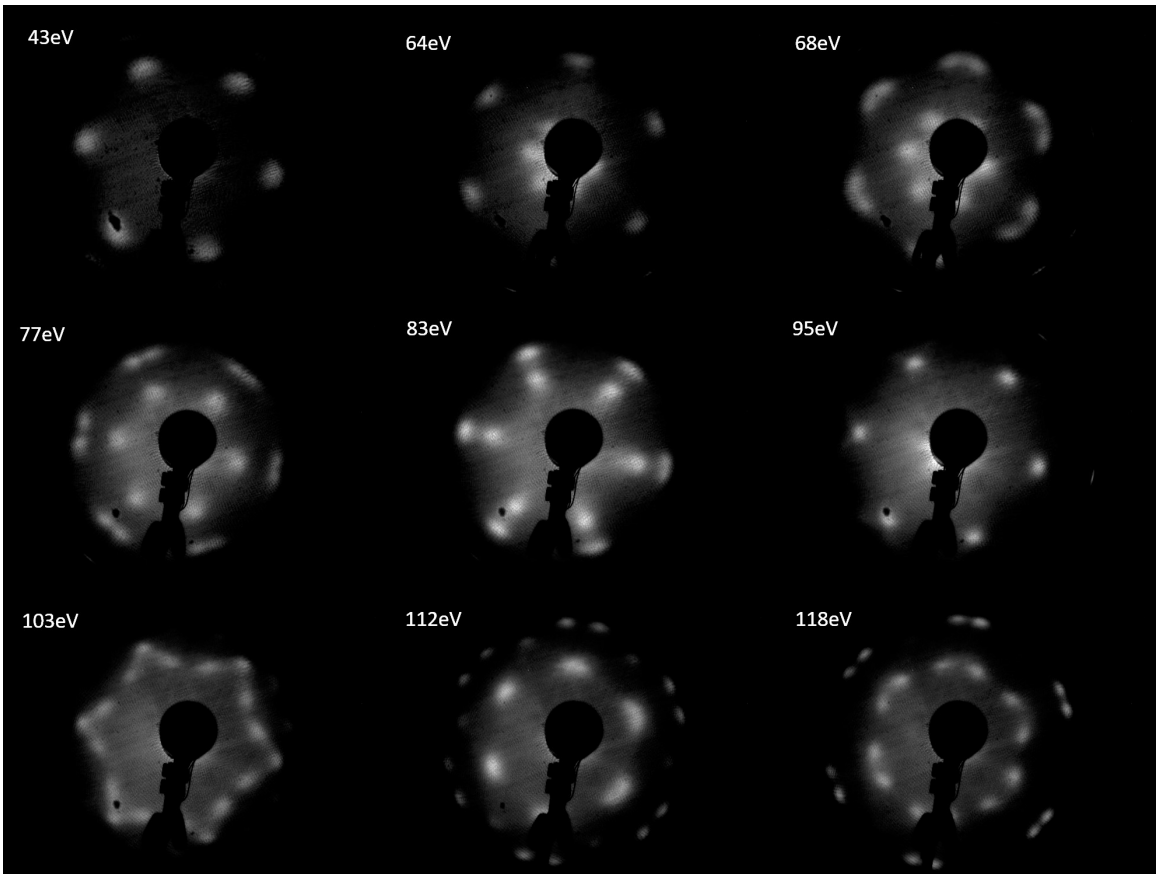

Figure 7.4: An array of LEED patterns acquired from a MgO film surface grown at high temperature at different incident beam energies. The diffraction spots surround the shadow of the LEED gun.

the ABC stacking sequence of the FCC structure. Similarly for O adsorption on an Mg-terminated surface with Mg atoms in B sites, the ideal C site is preferred over the A site by 0.50 eV/atom at the start of O growth, as expected for FCC stacking. The preference for O adsorption increases to 7.1 eV/atom at one-third coverage. This indicates that bulk MgO fcc polar stacking is preserved throughout growth.

While these adsorption energies show that calculations can predict the preferred atomic site for an atom on a surface, the calculations have not considered the nucleation process of the film. As discussed in chapter 2, the growth mode of a film is defined by the nucleation process on the surface, where it is energetically favourable to either adsorb atoms on existing nucleated islands or to nucleate new islands that may or may not coalesce during growth. The next set of results from calculations show that at one-third Mg coverage, the adsorption of magnesium atoms in nearest neighbor sites (forming a triangular cluster) is preferred over adsorption at other sites by

0.4 eV/atom. Cluster formation is even more preferable in the case of oxygen, where adsorption of on a triangular cluster is more favorable by 2.2 eV/atom.

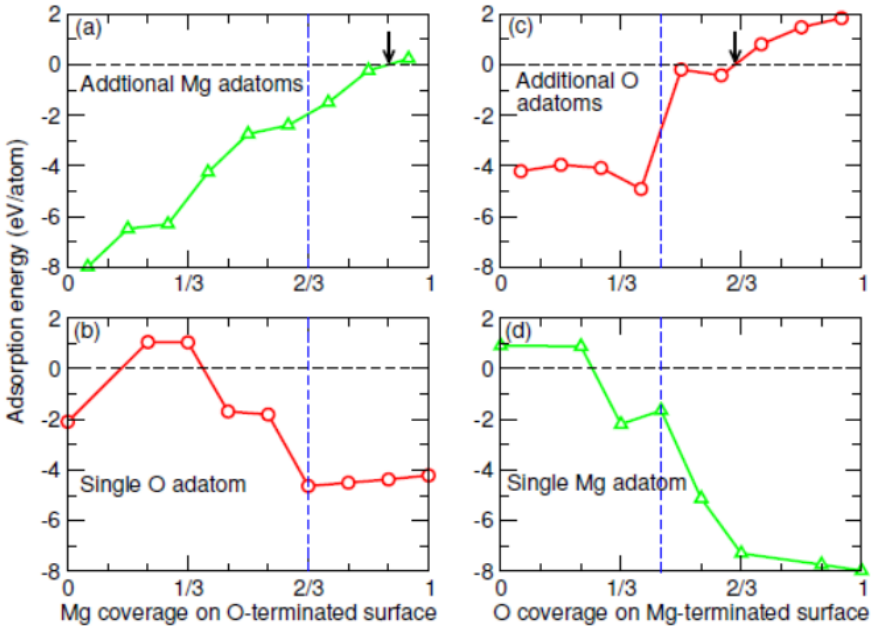

Figure 7.5: Simulated adsorption energies in eV/atom of (a) sequential Mg adatoms, and (b) single O adatom as a function of Mg coverage in (a); (c) sequential O adatoms, and (d) single Mg adatom as a function of O coverage in (c). Vertical dashed line in (a) and (b) shows Mg coverage at which O adatom becomes more binding (on the incomplete Mg layer) than Mg adatom. Similarly, vertical dashed line in (c) and (d) shows the O coverage at which Mg adsorption (on the incomplete O layer) is more favorable than O adsorption.

These results are illustrated in figure 7.5 showing adsorption energies for successive Mg and O adatoms for the lowest energy adsorption sites at T=0 as a function of the number of Mg and O atoms on the surface. Starting on a stoichiometric O-terminated surface Mg adsorption is energetically favorable till the surface has 8 out of 9 sites occupied. Starting on a completely Mg-terminated surface with only atomic oxygen in the environment the adsorption energy for O is found to be negative (i.e. O adsorption is favorable) till two-third O coverage on the surface.

Further simulations for MgO growth, wherein both Mg and O sources are simultaneously available in the growth chamber, are presented in figures 7.5(b) and (d). At two-third Mg coverage the next O layer starts forming in preference to further Mg growth, and analogously at almost one-half O coverage, formation of the next

Mg layer becomes more favorable than completion of the O layer. At the start of deposition of a Mg monolayer, the adsorption energy of both Mg and O adatoms at the same time is 3.8 eV/atom if O occupies one of the vacant Mg sites, and 2.7 eV/atom if O locates in to an ideal site in the layer above Mg, both of which are less than the adsorption energy of 8.0 eV/atom for only an Mg adatom as shown in figure 7.5.

As adatoms are added, they prefer to deposit close to the already formed cluster rather than at an isolated site from simulation. Considering continued growth of MgO on these adclusters, a polar stabilisation mechanism may be apparent whereby the clusters contribute to reducing the surface energy. The lowest energy surface of Mg) is the (100) surface. Formation of the LEED patterns in figure 7.4 due to (100) facet formation from this 3D growth mode is considered in figure 7.6.

Faceting of surfaces can be seen in LEED through the observation of specular reflections. For normal electron beam incidence a portion of electrons will be reflected straight back towards the electron gun, therefore when surfaces are tilted to be angled off normal incidence then these reflected electrons are observed as a spot on the screen. The spot generated by these reflections is independent of electron beam energy because it is not a diffracted beam and as a result the spot will remain in the same position on the screen, regardless of incident beam energy. The collection angle 2θ of the LEED screen on this system is $<50°$ from one side of the screen to the other. Predicting the angle that a specular reflection would leave a surface when reflected by (100) surface facets, relative to the (111) normal sample surface, results in a specular reflection at 40° from normal incidence. A LEED pattern recorded after rotating the sample to 40° from normal incidence is presented in figure 7.6(c). The pattern formed is square, characteristic of <100> surfaces.

The presence of facet formation on the surface is also predicted in growth simulations of adatom adsorption for different MgO structures during thin film nucleation, described in figure 7.7(b). A cross section view of the model shows triangular structures with non-polar <100> type faces. Figure 7.7(a) shows adsorption energies for magnesium (green) and oxygen (red) adatoms. The structure described in figure 7.7(b) is energetically favourable for oxygen adatom adsorption at $\frac{2}{3}$ Mg layer coverage. adsorption of an O atom in an ideal fcc site in the layer above the incomplete Mg layer (ΔE_O=4.63 eV) rather than further growth of the Mg layer (ΔE_{Mg}=1.5 eV).

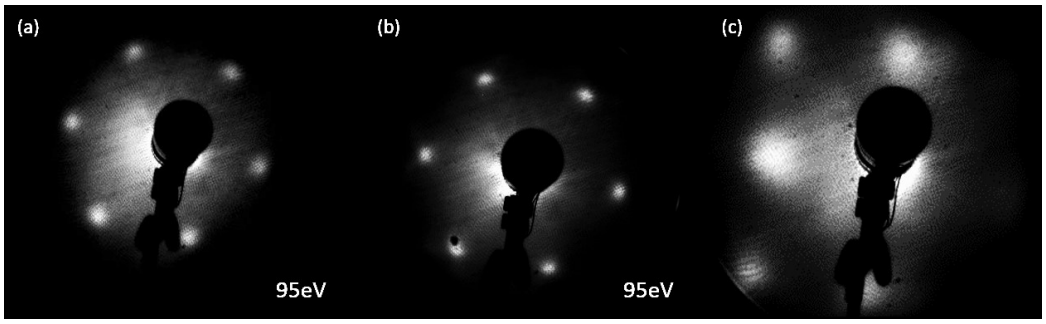

Figure 7.6: LEED patterns from (a) MgO(111) thin film surface grown at low temperature, (b) MgO(111) thin film surface grown at high temperature, (c) MgO(111) thin film surface grown at high temperature where the sample is tilted to 40° off normal electron beam incidence.

The films analysed by LEED and RHEED above were prepared for TEM and results from a high temperature MgO growth sample are shown in figure 7.8. Bright field TEM of the specimen at low magnifications, reveals that the film has adopted a 3D growth mode during deposition, shown in figure 7.8(c). The sharp interface of the MgO layer with SiC means that the growth mode of the film is not induced by preparation of the SiC surface. Coalescence of islands and incomplete layer formation, the latter of which is predicted in the simulations, leads to faceting of the film at the surface. This is shown in figures 7.8(a) and (b), wherein nanometre scale facets are observed. HRTEM of the MgO surface shows phase contrast of the crystal structure in figure 7.8(b). Measuring the angle between the faceted surface plane and the (111) plane results in the expected angle between (111) and (100) planes of 54.74°.

However, this system is inconsistent with results presented in the literature of defect free MgO(111) thin films. Further simulations were conducted to consider atomic position relaxation of Mg and O atoms within the layers during growth. Figure 7.9 shows the predicted relaxation amount for Mg and O atoms within the deposited film. At this point, layers within the film, i.e. below the surface, are considered to be in quasi-equilibrium with surrounding Mg and O atoms. In this model growth takes place by adsorption of atoms to the already existing cluster/island in preference to adsorption at isolated sites. For the an O terminated structure an Mg atom from a sub-layer moves completely through the surface O plane by a distance greater than the ideal interplanar distance of 1.21Å and continues this upward movement when the next O and Mg adatoms are added to the film. This relaxation is illustrated in figure 7.7(e). As growth continues the exact number of Mg atoms required to complete the

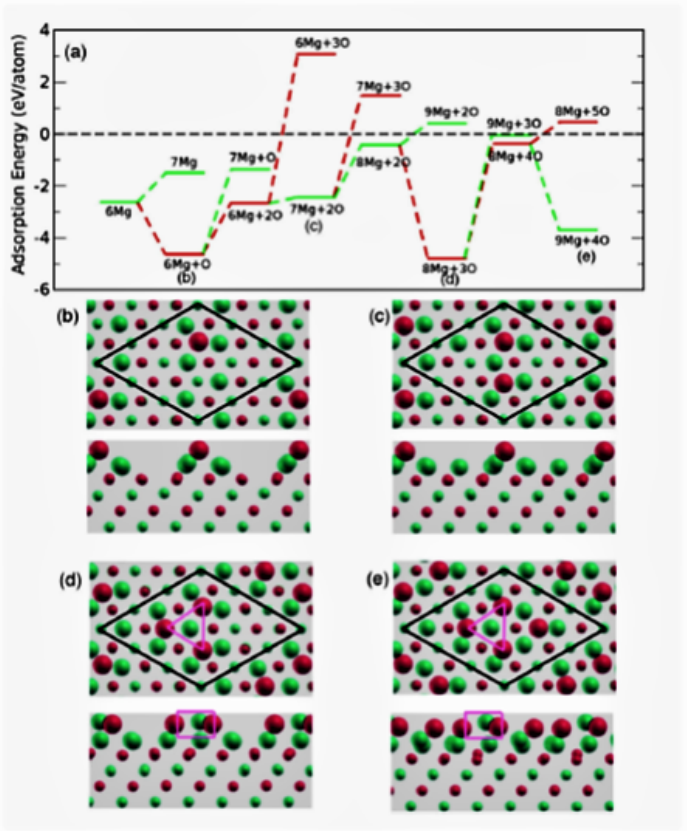

Figure 7.7: (a) Adsorption energy of Mg and O adatoms for different structures that form during the growth of a complete Mg layer on O-terminated (11) MgO(111). Top and side views of structures with (b) 7 Mg atoms in the Mg and 2 O atoms in the next O layer, (c) 8 Mg atoms in Mg layer and 3 O atoms in the next O layer, and (d) 9 Mg atoms in the Mg layer and 4 O atoms in the next O layer. Calculations are done for a (3×3) supercell as shown by the black outline. Green (light) and red (dark) spheres represent Mg and O, respectively. Mg atom at the center of the magenta triangle in (c) and (d) moves out of the Mg plane through the O layer upon structural relaxations.

Mg layer is satisfied, however outward displacement of an Mg atom through the O plane to the surface creates a vacancy in the Mg layer. As seen in figure 7.9, initiation of the next Mg layer triggers the displaced sub-surface Mg atom to move downward back into its ideal plane.

As the O and Mg adlayers continue to grow, an O atom in the sub-layer below the Mg terminating layer moves outward through the Mg plane to the surface of the film. A similar structure to that of the O terminated structure in figure 7.7 is also predicted for the Mg terminated structure. This displacement creates a vacancy

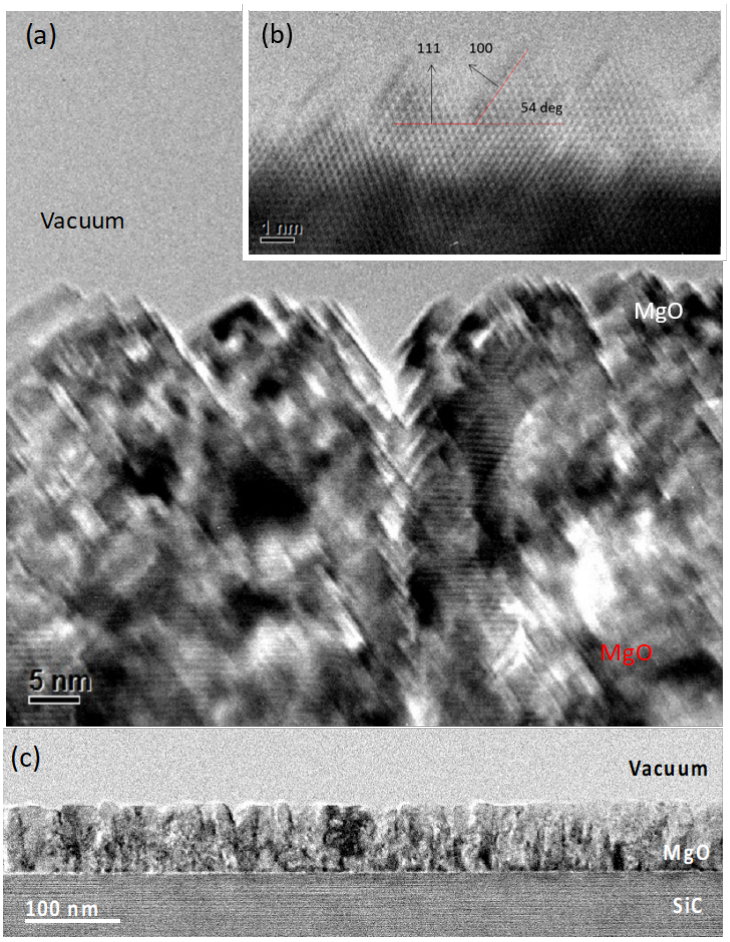

Figure 7.8: TEM images of a MgO(111) thin film grown at high substrate temperature, wherein (a) a bright field TEM image shows faceting of the film surface with nanometer scale features, (b) a HRTEM image of the faceted surface showing the angle between faceted planes and the (111) orientation and (c) a bright field TEMimage recorded at reduced magnification showing non-pillar like structures that extend to the interface showing 3D growth of the MgO(111) thin film.

in the O layer. This displaced O moves back into its ideal plane as the Mg layer coverage increases. It is evident from the magnitude of atomic displacements that the top three layers of the surface are neither atomically flat nor free of vacancies, however with progressive growth in the [111] direction the layers in the bulk of the film are approximately static and defect free.

The simulation results therefore describe layer-by-layer growth of MgO(111) thin films, applicable to results in the literature, however results shown in this work report 3D growth that is also supported by simulated results. Figures 7.6(a) and 7.10 show results from LEED and TEM of MgO(111) thin films grown at low temperature. Although the LEED pattern in figure 7.6(a) appears hexagonal like the faceted surface

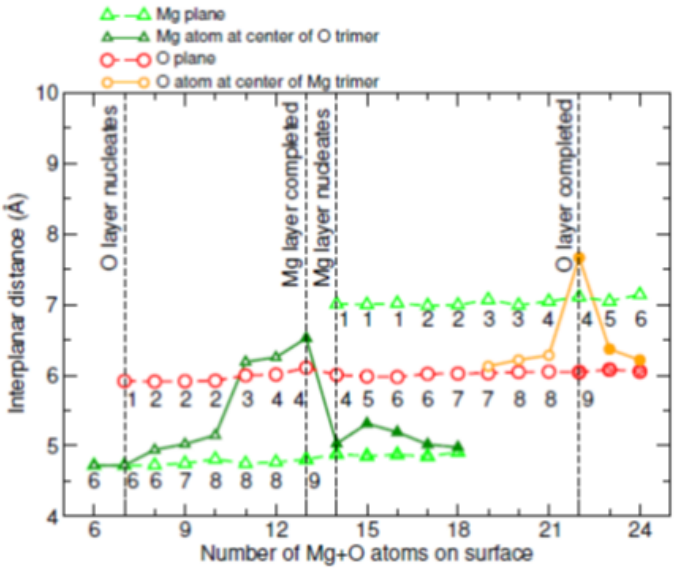

Figure 7.9: A graph of the Mg and O atom relaxations predicted in the MgO(111) growth simulations.

shown in figure 7.6(b), recorded at the same energy, the LEED pattern from the low temperature grown MgO thin film behaves as a LEED pattern would from a flat surface, wherein the spots move radially inwards with increasing beam energy. Although the spots are not sharp, indicating some surface roughness, features of faceting are not observed in the LEED of low temperature MgO(111) thin films. This is supported in figure 7.10 that shows bright field and HRTEM images of the MgO(111) thin film prepared at low temperature, similar to the growth conditions described in the literature [92, 138, 140]. The TEM images show that the MgO(111) films are epitaxial and a 2D growth mode was adopted during deposition, such as layer-by-layer growth. This result supports results from simulations wherein MgO film is defect free with some roughness observed at the surface.

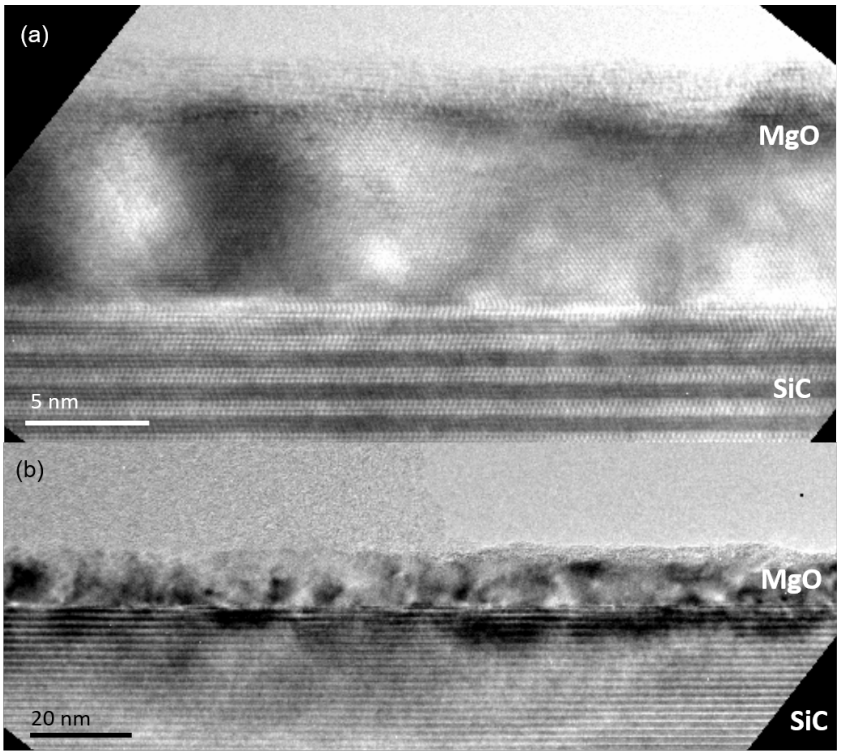

Figure 7.10: TEM images of a specimen prepared from MgO(111) thin film growth at low temperature. (a) HRTEM image of the MgO(111) thin film showing a defect free film and a sharp interface between the film and the SiC substrate. (b) Bright field TEM image acquired at reduced magnification showing the MgO(111) film over a longer range. This result shows that the film has uniform thickness and low surface roughness.

7.4 Conclusion

The results presented from simulations of MgO(111) growth show that a quasi-equilibrium model can explain the formation of defect free MgO(111) thin films by MBE growth, as reported in literature. The simulated results also support the formation process of MgO(111) by 3D growth.

Comparisons of the experimental results obtained for the different MgO(111) thin film growth conditions show that the growth mode adopted during deposition strongly depends on the substrate temperature. Results of high temperature MgO(111) growth conditions, wherein the substrate temperature is 500°C, show 3D growth resulting in faceted surfaces. These surface and structural defects in the 3D grown films would not be suitable for multi-layer device applications such as power MOSFETs or

spinFETs.

Comparing these results with the simulated results suggests that reduced substrate temperature during deposition may allow for Mg and O atomic relaxations to occur, establishing 2D layer-by-layer growth for low substrate temperature conditions. These relaxations are the possible migration of atoms through the film into vacancies as subsequent layers are deposited. The reduced substrate temperature reduces mobility of adsorbed atoms resulting in potential vacancies. It is noted that, for example, oxygen vacancies are likely to be present in MgO thin films. Such vacancies can be indirectly observed by eye during surface electron diffraction experiments of bulk MgO samples, wherein the sample emits blue light upon interacting with the electron beam. These experimental observations support the presence of vacancies and therefore, migration of atoms into said vacancies could be possible.

High substrate temperature growth conditions result in point defects and surface faceting, predicted in the simulations as incomplete layer growth. The simulations show that 3D growth in the form of pyramidal structures could be possible depending on the adsorption of Mg or O on the surface, as shown in Figure 7.7(b). Therefore, it would appear from experimental growth conditions that the possible adsorption paths shown in Figure 7.7 may in fact be dependent on substrate temperature. However, this has not been directly confirmed with further simulation.

Results presented in this chapter were prepared in collaboration with K. Pande, M. Gajdardziska-Josifovska, and M. Weinert of the Department of Physics and Laboratory for Surface Studies at the University of Wisconsin-Milwaukee. The results of their simulations have provided valuable insight into the process of MgO(111) thin film growth.

Chapter 8

Band alignment of MgO(111)/SiC(0001) interfaces

Research developments in high power electronic devices has created interest in wide band gap semiconductors, requiring research into new oxide-semiconductor heterostructures. MgO(111)/6h-SiC(0001) has been proposed for the development of high power electronic and spin-electronic devices as discussed in the introduction to this thesis. The low lattice mismatch between MgO and SiC minimises interfacial strain, ideal for reducing leakage currents in high power devices. This work analyses the interfacial structure and interface band alignment of MgO(111) thin films deposited on 6h-SiC(0001) by MBE growth. This work highlights the impact of atomic engineering on band alignment at the interface.

8.1 Introduction

The development of new devices for high power electronics and spin-electronics has promoted research interest in novel oxide-semiconductor hetero-structures. SiC has already demonstrated its performance in high power MOSFET devices using silica as a gate dielectric however silica is not suitable for the harsh processing and operating conditions of such devices [5, 22, 23, 143–145]. MgO has been proposed as a new candidate for oxide barriers in SiC based devices due to its high dielectric constant of k=10 [34, 43, 146], low lattice mismatch with SiC of only 3% and unique spin filtering properties [27–30, 147–149]. Research interest around MgO/SiC interfaces extends into physics of the polar catastrophe [45–50, 150, 151]. MgO deposition on SiC(0001), requires MgO to grow with (111) texture to minimise lattice mismatch.

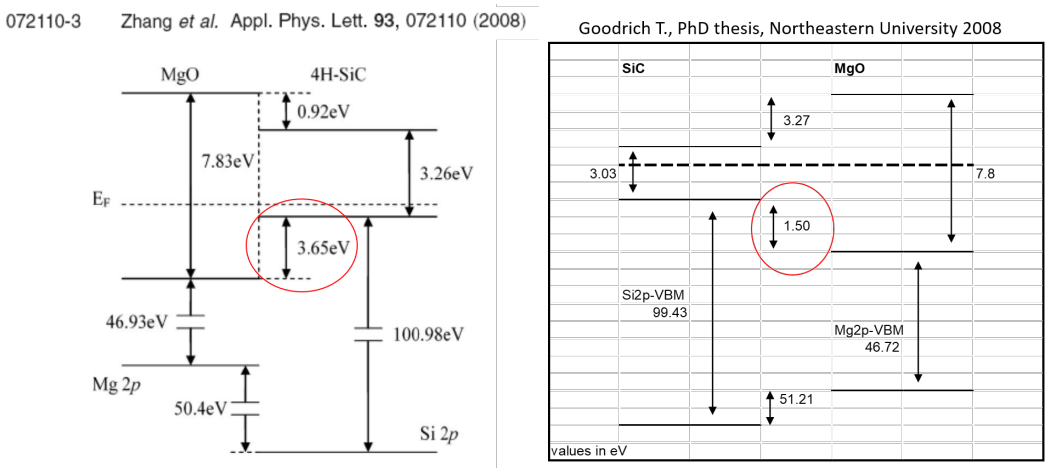

Figure 8.1: Energy band diagrams for the MgO/SiC interfaces reported in the literature. The experimentally determined valence band offset values are circled in red for (a) the MgO/4h-SiC interface and (b) the MgO/6h-SiC interface [152, 153].

Along this (111) orientation, MgO is polar with alternating anion-cation planes. An uncompensated electric dipole moment is established from this polar structure, which is unstable under frozen bulk termination. This unstable termination leads to large surface reconstructions or adsorption of atoms or molecules on the surface, as seen in Chapter 7 [151]. This property of MgO presents interesting research into effects of the polar catastrophe on interface band alignment, as considered in the introduction to this thesis. In this work, epitaxial growth of MgO(111) thin films with low surface roughness is demonstrated. A stabilisation mechanism for reducing surface roughness of the polar surface has been theorised by Lazarov et al. [142] and presented in chapter 7.

Results published in literature report valence band offsets for MgO(111)/GaN(0002), MgO(111)/4h-SiC(0001) and MgO/6h-SiC(0001) [41, 152, 153]. However, there are discrepancies between the valence band offset reported for MgO/4h-SiC(0001) and MgO/6h-SiC(0001). The 3.65eV valence band offset for the 4h-SiC interface is over double that reported for 6h-SiC, of 1.50eV. Results from the literature are presented in 8.1. The theoretical and experimental results presented in this chapter help to explain the origins of the inconsistent results in the literature.

Although the substrates are of different SiC polytypes i.e. 4h- and 6h- in the two interfaces reported above, the band structures of the two polytypes are almost identical as discussed in chapter 6. However it is unclear how the polytypes differ

in other properties such as doping concentration and detail on defect density in the substrates is not reported in the literature. Based on predictions reported in literature [77, 80] briefly discussed in the introduction, the difference in these values of the valence band offset may be expected from a difference in bonding due to strong polar characteristics in both film and substrate rather than properties such as interface gap states.

8.2 Experiment

SiC substrates were prepared by annealing in hydrogen gas under HV conditions. Substrates used are n-type 6h-SiC wafers with dopant concentration of 10^{17} cm^{-3}. Base pressure of the system is 2×10^{-10} mbar. For annealing, the SiC substrate sample was heated to 900°C under 5×10^{-8} mbar of molecular hydrogen. The gas pressure was measured using an ion gauge and a residual gas analyser. The samples were heated by DC resistive heating. The temperature was measured using an IR pyrometer, with emissivity at 0.65, although the exact temperature was outside the measurement range of the pyrometer, however substrate temperature during deposition was $\leq$200°C. Hydrogen was used to passivate the dangling bonds on the SiC surface as described in chapter 6. This method sharpens the step edges due to the saturation of dangling bonds at step edges, promoting formation of 200nm wide terraces [128]. Hydrogen adsorbed on the substrate surface is also proposed to act as a surfactant for layer-by-layer MgO growth [142] as described previously in this thesis.

MgO thin films were grown using plasma assisted molecular beam epitaxial growth. The deposition technique comprises exposure of the substrate to magnesium and oxygen simultaneously. Magnesium was deposited from a Createc low temperature effusion cell, set to 280°C. This provides a magnesium deposition rate of $\approx 2\mathring{A}$/min, determined using a calibrated quartz crystal microbalance. Oxygen is provided in plasma form from an Oxford Applied HD-25 plasma source operated at 90W. Oxygen pressure in the system is 1×10^{-6} mbar measured by an ion gauge. To minimise silica nucleation, the substrate is first exposed to magnesium flux while the oxygen plasma is prepared. Setup time for the oxygen plasma is difficult to control and results in inconsistent oxygen exposure between each experiment. Thin films prepared for analysis by XPS and TEM range in thickness from 2 - 20 nm.

The XP spectra were acquired using a monochromated Al Kα X-ray source with electron beam flood gun to minimise surface charging and enable reliable charge offset

correction. The spectra were charge corrected using a gold reference and Carbon 1s reference from SiC. The valence band maximum for the SiC and MgO were measured from a bulk SiC reference and 20nm MgO film grown on SiC. That way SiC would not be measured as the maximum depth profiling limit for the XPS technique is ≈6nm at normal surface X-ray incidence. The core energy levels for Mg 2p and Si 2p were measured from bulk references and compared to the core level values measured for the MgO/SiC thin film interface in order to calculate the valence band offset. The s-orbitals were measured as the bonding states used for the valence band offset calculations with equation 8.1. These states were chosen because the signal from the 2p states of Si and Mg is small, therefore to improve the energy resolution in the XP spectra the s-states were measured. It will become clear in this chapter that this difference does not impact on the conclusion drawn because the valence band maximum is measured independently in experiments. It should be noted that Si or C can be used as the anion in SiC, however this work considers the Si terminated surfaces and interfaces of 6h-SiC and therefore Si is chosen as the anion for equation 8.1.

STEM of specimens prepared from the samples measured by XPS was conducted at 100kV, applying an average stacked image technique to achieve atomic resolution at the interface. This method of image acquisition in STEM accounts for specimen drift during scanning of the beam and enhances image contrast by averaging out noise. The samples were prepared for STEM by conventional polishing methods followed by further thinning using ion milling [102] to achieve electron transparency. The work was conducted in collaboration with SuperSTEM in Daresbury, UK, where HAADF images have been acquired for this work. QSTEM simulations have also been conducted to compare model structures with the results reported. The parameters used of these simulations matched with recorded parameters used in the microscope, however the main source of error in the simulations is the exact specimen thickness as this is unknown. Furthermore, thermal factors have not been accurately simulated in the SuperSTEM simulations presented. This explains why contrast in the the simulation is greater than in the experimental image.

CASTEP simulations [154] were conducted to determine the interface atomic structure by comparing valence band offset calculations with empirical data. Using CASTEP, the eigenvalues for bulk MgO and SiC are calculated to determine the band positions and valence band maxima. To compensate for the electric dipole moment in the MgO structures modelled, hydroxyl terminations were used as the terminating

layer, shown in figure 8.4(d). Note that although theoretically corrected, electric dipole from the film is still present in the simulated result. This is, in part, due to the weak polar structure of SiC described in chapter 6. In order to analyse the position of the bands at the interface, the electrostatic potential of the bulk systems must be calculated. This is described as the mean inner potential and can be calculated for the bulk films, applied as a GW correction. This GW correction is a normalisation of the potential removed from the valence band maximum value calculated.

8.3 Results

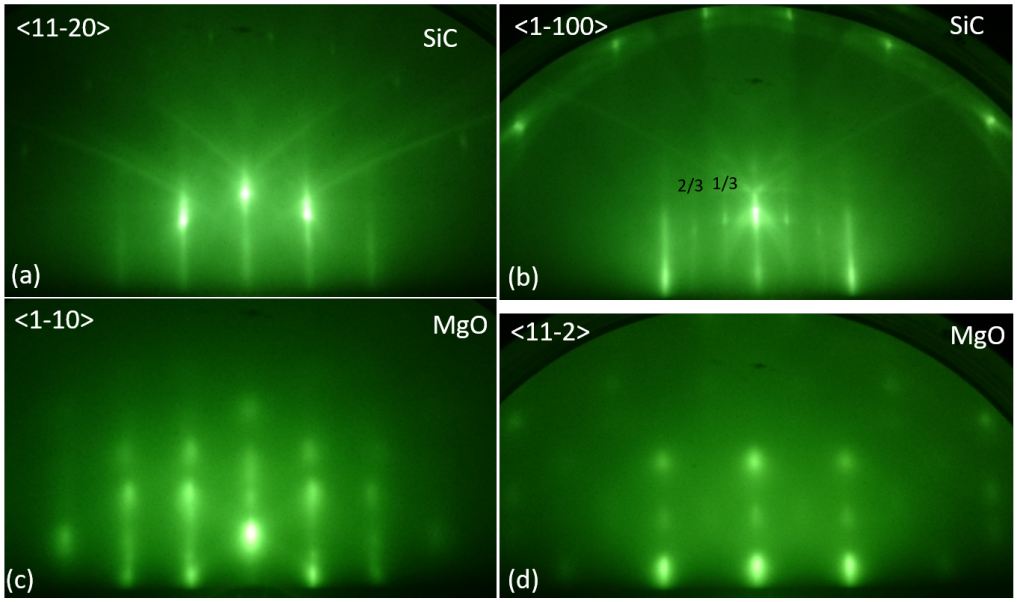

Figure 8.2: (a) RHEED pattern obtained from an in-situ prepared SiC substrate wherein the pattern has been recorded for an incident beam zone axis of $<11\bar{2}0>$. (b) RHEED pattern obtained from an in-situ prepared SiC substrate wherein the pattern has been recorded for an incident beam zone axis of $<1\bar{1}00>$. (c) RHEED pattern obtained from a MgO thin film wherein the pattern has been recorded for an incident beam zone axis of $<1\bar{1}0>$. (d) RHEED pattern obtained from a MgO thin film wherein the pattern has been recorded for an incident beam zone axis of $<11\bar{2}>$. All patterns were recorded under the same beam conditions meaning that variations in background intensity are due to the sample surface conditions.

Results of thin film preparation are shown in figure 8.2. This figure shows the RHEED patterns after SiC surface preparation and subsequent MgO deposition. The SiC surface reconstruction can be seen in figure 8.2 (b) indicating a $\sqrt{3} \times \sqrt{3}$-R30° surface, marked by the streaks positioned at $\frac{1}{3}$ spacings between the (00) and <10>

streaks. This reconstruction is not visible in RHEED pattern generated from beam incidence along a <1-100> zone axis pictured in figure 8.2(a) because the projection of the reconstruction overlaps with the SiC bulk lattice. Kikuchi diffraction and first order Laue zone are observed for figure 8.2 (a) and (b) indicating a flat surface based on the criteria described in chapter 2.

Figure 8.2(c) and (d) show RHEED patterns for flat MgO thin films. Although the streaks have variable intensity the surfaces have low roughness. This variation in topography can be attributed to steps and surface roughness induced by the polar stacking sequence. The roughness observed appears greater in the pattern generated from the diffraction from <110> planes, figure 8.2(d) than in the pattern recorded from diffraction from <112> planes in figure 8.2(c). The origin of this difference could possibly be from alignment of periodic MgO surface features such as nano-facets, however this is only speculation.

Figure 8.3 (a), (b) and (c) are XP spectra acquired to determine the valence and conduction band offsets. The dashed lines represent the fit applied to the data to accurately determine the energy values of core levels and valence band maxima. Core level data was fitted using a Split Pseudo-Voigt function, which is a modified Gaussian function that accounts for assymetry in the data peak due to the removal of the Shirley background. The valence band maximum is determined by the energy value at the intercept where the linear fit crosses the baseline signal. Figure 8.3(a) discloses results of the 2s core level measurements for both Si and Mg measured from the thin film specimen, of which the MgO film is 2.5nm thick. The binding energies measured from these peaks are in agreement with those on record in the NIST XPS database [94] for SiC and MgO.

Figure 8.3(b) details the data measured from the "bulk" MgO 20nm thick film. The binding energy measured for the peak fitted corresponds, as labelled, to the Mg 2s energy state in MgO. The valence band maximum was determined from interpolation of the spectra as spectrum approaches the valence bend edge. Figure 8.3(c) discloses the same information as (b) but for the SiC Si 2s and valence band maximum reference. Figure 8.3(d) describes the band structure at the interface of MgO and SiC illustrating the position of the band offsets ΔE_c and ΔE_v. The band gap energies of 6h-SiC and MgO are also enclosed in the diagram.

For MgO/SiC the calculation of the valence band offsets (VBO) from the XP

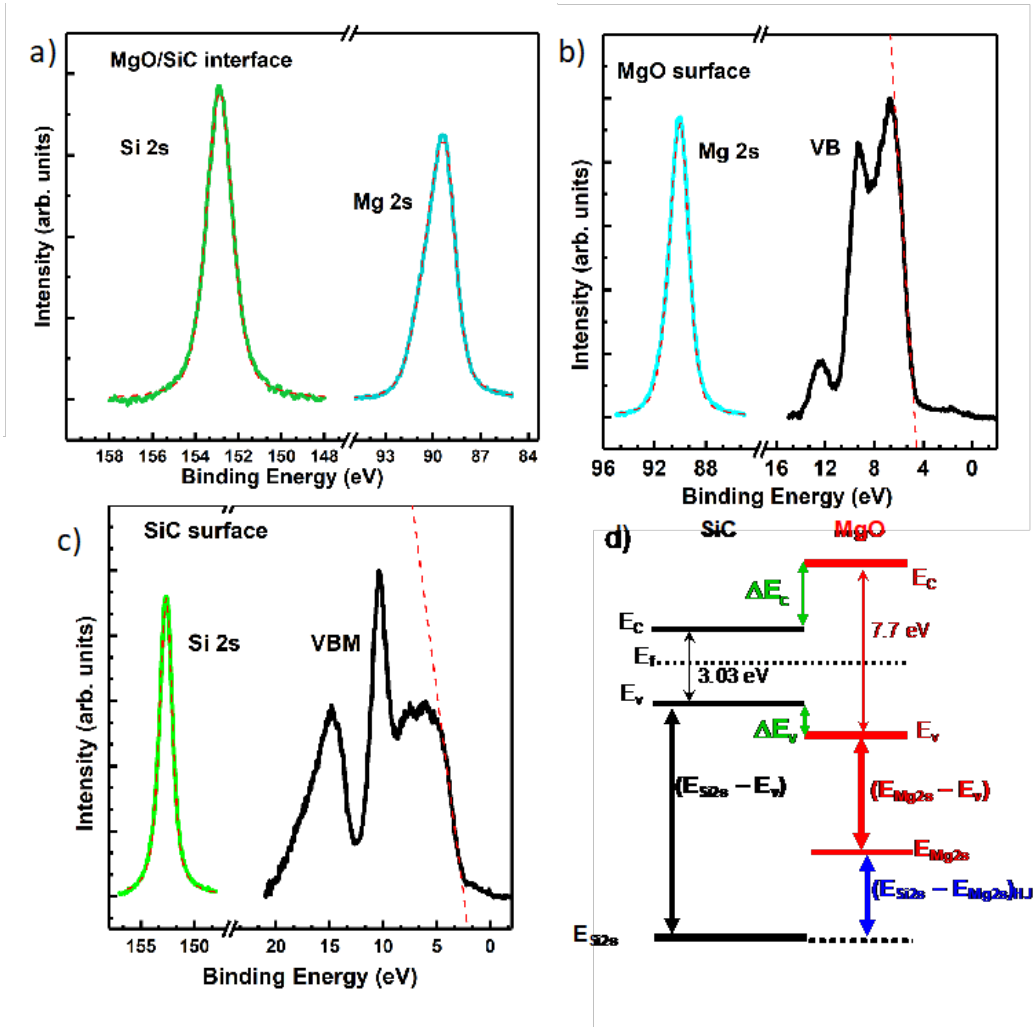

Figure 8.3: (a) XP spectrum acquired from the MgO/SiC thin film interface, from which the core level difference in equation 8.1 is calculated using binding energies of Mg 2s and Si 2s orbitals. (b) XP spectrum acquired from a thick 20nm MgO film on SiC, used a bulk reference for the Mg core levels and the valence band maximum. (c) XP spectrum acquired for SiC to determine the same properties as in (b). (d) An energy band diagram describing derivation of the band alignment of MgO and SiC from the XPS results.

spectra acquired requires modification of equation 3.2 to form:

$$E_{VBO} = (E_{Si^{2s}} - E_{Mg^{2s}})_{HJ} - (E_{Si^{2s}} - E_{Si^{VBM}})_{SiC} + (E_{Mg^{2s}} - E_{Mg^{VBM}})_{MgO} \quad (8.1)$$

Parameters for the calculation [98, 99] are outlined in the schematic in figure 8.3(d). The valence band offset from the XP spectra for the MgO/SiC interface was calculated from the measured energy positions of the Mg 2s, Si 2s and respective valence band maxima to be 1.62 eV. The calculation is shown below.

$$(E_{Si^{2s}} - E_{Mg^{2s}})_{HJ} = 152.93 - 89.73$$

$$(E_{Si^{2s}} - E_{Si^{VBM}})_{SiC} = 152.74 - 2.52$$

$$(E_{Mg^{2s}} - E_{Mg^{VBM}})_{MgO} = 90.3 - 4.9$$

$$E_{VBO} = 1.62\text{eV}$$

This value is not in agreement with that reported by Zhang [152]. However, the value is in reasonable agreement with that reported by Goodrich [153], indicating that valence band offset measurements acquired from s-orbital and p-orbital measurements are comparable and that the interface structure of these cases must be equivalent.

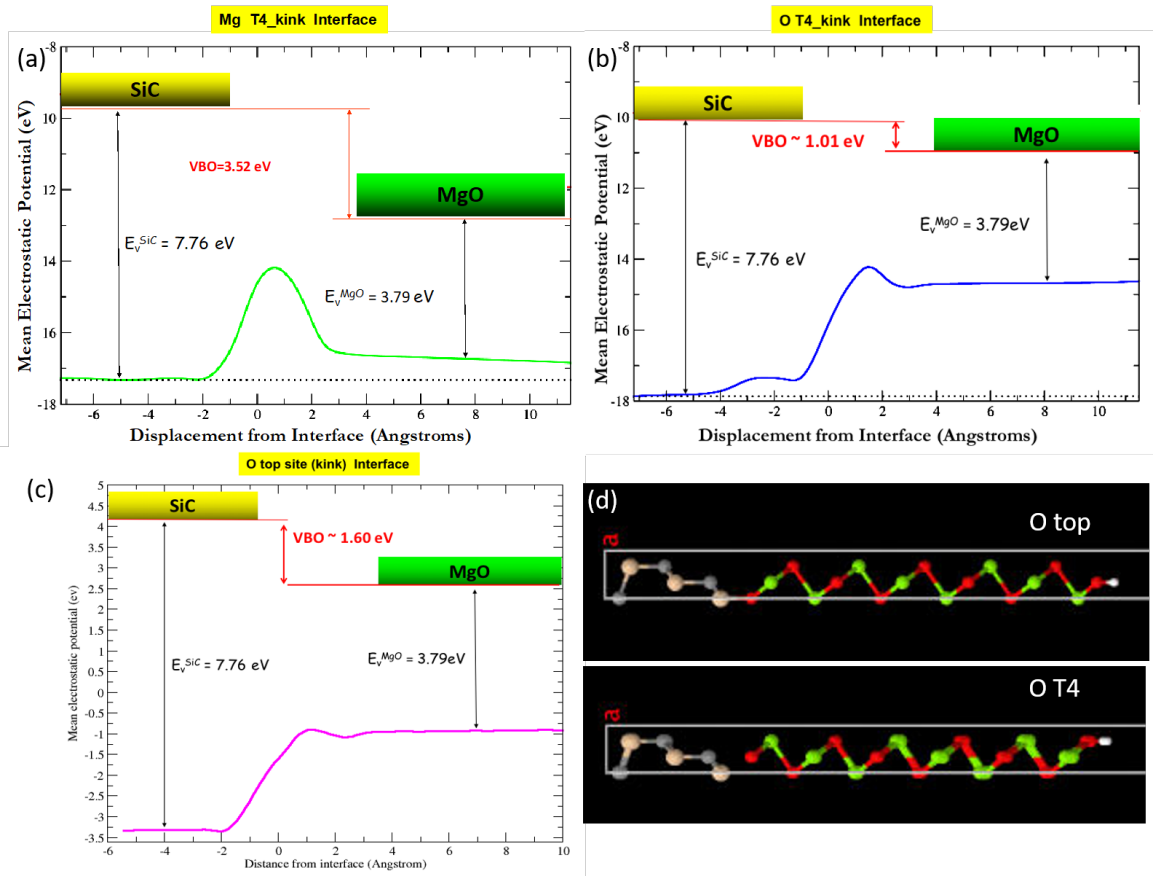

Figure 8.4: Graphs of the valence band position across the interface calculated with CASTEP. The interface terminations analysed are (a) the Mg interface termination with Mg in the T4 bonding site. (b) and (c) are calculated for the O termination with O in the T4 and top site respectively. (d) includes structural models for the O interface terminations used for the CASTEP calculations. Si atoms are represented in brown, C atoms in grey, O atoms in red and Mg atoms in green. The single white atom on the MgO surface is hydrogen.

To understand this discrepancy, CASTEP code has been used to predict the valence band offset for three different interface terminations. These interface terminations comprise a Magnesium terminated interface where the magnesium ion is positioned in the next tetragonal T4 site on the SiC surface, offset from where the next C atom would be positioned if the 6h structure were to continue. Equivalent calculations have been performed interchanging Magnesium for Oxygen in the T4 site. The position of the T4 site is illustrated in figure 8.4(d). For the third interface structure for which the valence band offset was simulated is oxygen in the top site position on the SiC surface, where the next C atom would sit if the 6h structure of SiC were to continue. The atomic position of this site is illustrated in cross-section in figure 8.4(d). The models used for the calculations are the same as those graphically modelled in figure 8.4(d). The value of the valence band offset calculated for the Magnesium terminated interface with Magnesium in the T4 site is 3.52eV. This in agreement with the value of the valence band offset reported by Zhang et al. shown in figure 8.1a. This interface structure also has the lowest formation energy, partially due to having the lowest remnant dipole in the MgO film of any of the simulated interface structures, described by the gradient of the line extending into the MgO film in figure 8.4. This data indicates that the valence band offset is dependent on the interface termination of the film.

Figure 8.5 explains the origin of this experimental and theoretical difference in the valence band structure at the interface. The figure presents a HAADF-STEM image 8.5(a) of a specimen prepared from the thin film measured by XPS for the band offset measurements presented herein. The MgO film is labelled in the top half of the image, where the intensity of electrons recorded by the detector is lower than the intensity for SiC, labelled in the bottom half of the image. Cloud like variations in the contrast across the image are due to contamination on the specimen from specimen preparation.

The image shows contrast of atomic columns, indicating that the film is epitaxial with the substrate surface, with a sharp interface and low defect density. There is no presence of amorphous silica within the region studied by STEM. However, looking more closely into the interface termination there is a row of atomic columns of reduced intensity at the interface, matching that of the intensity of the oxygen planes in the MgO film. To confirm the interpretation of the structure from the image, the QSTEM simulation package was used to simulate HAADF STEM images for the O top interface

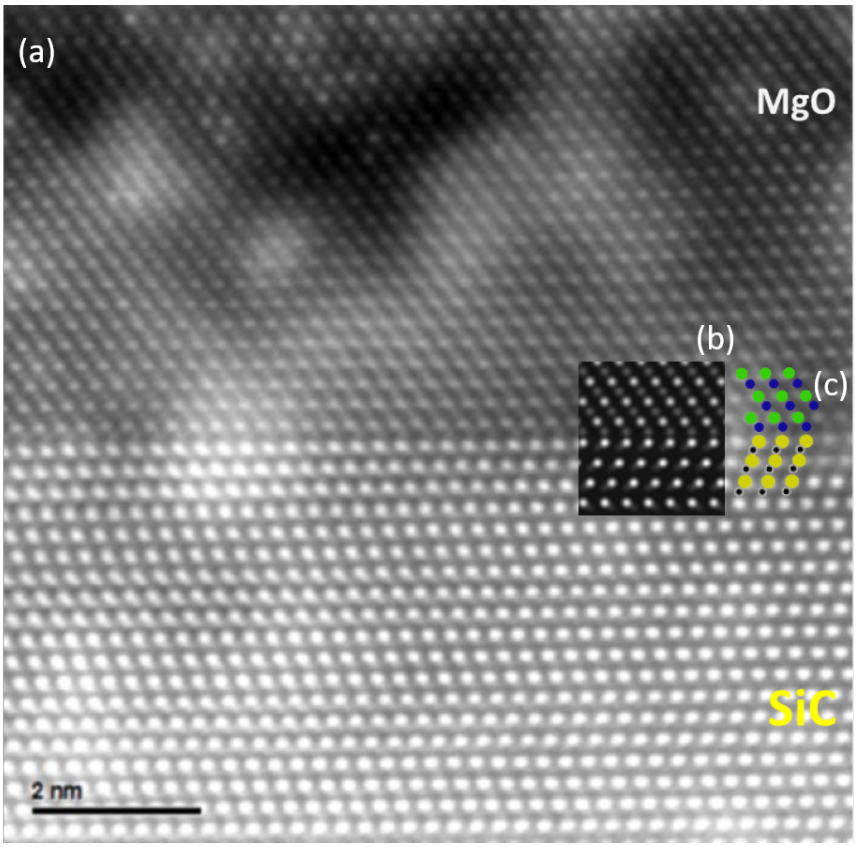

Figure 8.5: (a) A HAADF STEM image acquired at SuperSTEM, imaging a specimen prepared from the thin film sample from which XPS results were obtained in figure 8.3. The MgO film is positioned in the upper half of the image, while SiC has higher intensity in the image due to the Z^2 atomic number dependence of electron scattering through the specimen. Cloud like variations in contrast across the sample are a result of contamination from specimen preparation. (b) A HAADF STEM image simulated using QSTEM, wherein the structural model used for the simulation is the oxygen top site interface termination described in figure 8.4. (c) A schematic model of the interface structure, illustrating the kink at the interface due to the change in direction of the stacking sequence.

structure. This simulated image is shown in figure 8.5(b) [108]. A complimentary diagram of the structure accompanies the simulation as figure 8.5(c).

For the QSTEM simulation a model of the interface was generated using CrystalKit software and crystal parameters from the model used in the CASTEP simulations discussed above. Microscope conditions were simulated using 100kV beam energy and a detector covering 70-200 mrad scattering angles. The simulation was setup with multi-slicing with a single atomic plane per slice. Various sample thicknesses were modelled. The simulation displayed herein was setup as 40nm thickness.

Simulations of thicker specimens were difficult to setup due to possible misalignment of slices with atomic planes. Thermal Diffuse Scattering (TDS) was, in error, not simulated in this case, due to modification of the configuration file for computation with a 12 core computer. The model was setup for 100x100 pixels, which requires a lot of computing time, hence the use of a 12 core computer. Omission of TDS in the simulation may account for differences in the background contrast between the simulation and the recorded image.

Oxygen can access the SiC surface in three ways during the thin film preparation comprising; residual silicate after hydrogen annealing forming the reported $\sqrt{3} \times \sqrt{3}$-R30° silicate adlayer reconstruction [123–125], oxidation during film nucleation, or adjustment in stacking order due to step edges on the SiC. Formation of oxygen at the interface is also reported in post deposition annealing experiments, described in chapter 7. While the STEM result and simulation thereof presented indicate that oxygen may be present at the interface, carbon may also be present from annealing the sample. Columns of carbon atoms would also appear faint in a HAADF STEM image due to the dependence on atomic number in electron intensity in HAADF imaging. However, results for the valence band offset, both experimental and theoretical, support a trend in the results that suggests the valence band offset is significantly reduced by the presence of oxygen at the interface.

8.4 Conclusion

This work demonstrates that polar MgO growth is compatible with 6h-SiC. Epitaxial growth has been observed with sharp interface formation, single crystal quality observed with STEM, and qualitatively low surface roughness observed with RHEED. The low defect density observed in the HAADF STEM result indicates that strain in the MgO structure at the interface is low. The valence band offset from the 2s states in these films is in agreement with that reported in literature where 2p orbital states have been measured, indicating that the XPS valence band offset measurement technique is not sensitive to the orbital state measured for these materials. This is most likely due to the fact that the position of the valence band maximum is included in the band offset measurement, correcting for any differences in the p- and s-state contributions to the valence band maximum.

In addition, we have demonstrated through simulation that the interface electronic structure can be tuned by atomic engineering at the interface. The valence band offset for the oxygen top site termination is in excellent agreement with the experimental results presented herein and the results reported in the literature [153]. Inconsistencies in experimentally determined valence band offsets reported in literature have been explained using CASTEP simulations, identifying that the results reported by Zhang et al. for the MgO/4h-SiC valence band offset correspond to a Magnesium terminated interface while results reported from this work and by Goodrich are indicative of an Oxygen terminated interface. A probable cause of this oxygen layer at the interface comes from incomplete removal of oxide prior to deposition in the form of a silicate adlayer SiC surface reconstruction [123, 124, 140].

The band alignment between MgO and SiC has also been identified as a type-1 band alignment, with a valence band offset of 1.60eV and a conduction band offset of 3.1eV for the heterostructures measured in this work. This band alignment is a promising result for MgO/SiC device development. The ability to choose the terminating element at the interface introduces novel opportunities for MgO based electronics thanks to the large valence band offset difference between Mg and O interface terminations.

Results presented in this chapter were prepared in collaboration with P. Hasnip of the Department of Physics at the University of York, K. H. L. Zhang of the Department of Chemical and Biochemical Engineering at Xiamen University and SuperSTEM. The CASTEP simulation results shown were conducted by P. Hasnip and

these have been invaluable for understanding the relationship between the interface structure and the valence band offset. The XPS results provided for experimental determination of the valence band offset were acquired by K. H. L. Zhang and his team. STEM results presented were acquired at the UK national electron microscopy facility SuperSTEM.

Chapter 9

Summary of results and future work

The results presented in this work show successful growth of polar MgO(111) thin films by MBE confirmed by analysis of the thin films using surface electron diffraction, XPS, TEM and STEM techniques, described in chapters 2, 3 and 4 respectively. Preparation of flat 6h-SiC(0001) by hydrogen cleaning in the UHV chamber has been shown, resulting in a clean template for subsequent MgO(111) growth. RHEED patterns of the 6h-SiC(0001) surface after processing with hydrogen indicate ordered flat surfaces with a $\sqrt{3} \times \sqrt{3}$ - R30° surface reconstruction. This reconstruction is know in the literature to be terminated with either silicon or a silicate adlayer. Therefore, results presented for prepared 6h-SiC(0001) surfaces are in agreement with results reported in literature. It is also noted that preparation of SiC substrates by molecular hydrogen in medium to high vacuum conditions is not thoroughly reported in the literature.

This work has also shown that control of the substrate temperature during MBE growth of MgO(111) thin films results in different growth modes. High substrate temperature conditions of 500°C result in 3D MgO structures with faceted surfaces. Experimental results from TEM and LEED show that MgO surface facets are (100) surfaces, formation of which is supported in the simulation results presented wherein incomplete layer formation during growth is predicted. Although the simulation does not, and could not reliably, account for substrate temperature, it would suggest that possible growth mechanisms determined from simulation are dependent on the temperature of the substrate. While faceting of MgO surfaces is known from

literature, temperature dependence of 3D growth and facet formation has not been extensively studied.

Low substrate temperature growth results in layer-by-layer 2D growth of MgO (111) thin films, confirmed by TEM and STEM. These results are in agreement with those reported in literature for similar low substrate temperature MBE growth conditions. However, in both this work and literature, a variety of possible oxygen and magnesium conditions are reported. No source or substrate is identical and therefore discrepancies between groups are to be expected.

Further simulation of MgO(111) growth provides clarity on how the Mg and O atoms may overcome incomplete layer formation through atom position relaxation. Comparison of the simulated results with experimental data indicates that at low substrate temperature relaxation of atoms may occur to enable complete layer formation and subsequent 2D growth whereas at elevated substrate temperatures the growth dynamics follow a 3D growth mode complimentary to the incomplete layer growth simulations. While vacancies in low temperature MgO thin films were not observed with electron microscopy in this work, low temperature and therefore low mobility of atoms may lead to vacancies during growth, which theoretically could be relaxed by atoms filling them from other layers. These theoretical results could potentially be confirmed by chemical analysis in the microscope such as EELS however specimen conditions did not allow for detailed chemical analysis of MgO/SiC heterostructures. To my knowledge there are no reports of atomic relaxations for this material system.

The presence of vacancies in MgO films may also have an effect on the band structure at the interface. However, vacancy concentrations may be too low to determine this by electrical measurements. Interestingly, vacancy control through growth conditions may be able to provide a method for controlling electronic properties for device applications.

Successful growth of MgO(111) films as thin as a few nanometres has also been demonstrated. Structural characterisation of these films has been performed using RHEED and STEM, the results of which show epitaxial films that are defect free with low surface roughness. The electronic band alignment at the interface of these thin films with MgO has also been measured by XPS and determined a type-I band alignment across the interface. This band alignment type is ideal for MOSFET applications due to the ability to control the flow of charge for both electrons and holes across a junction, as discussed in the introduction to this thesis.

Discrepancies in the valence band offset reported in literature have also been clarified using STEM and CASTEP simulations. CASTEP predicts the 2eV difference in the valence band offsets reported originates from different interface structures. This result is confirmed with STEM showing the interface structure of MgO(111) on 6h-SiC heterostructures. QSTEM simulations of STEM images for this structure have been presented to confirm the structure observed in the experimental images. The results indicate that oxygen may terminate the MgO film at the interface with SiC however this has not been confirmed experimentally. For example, carbon may also be a candidate for a terminating layer due to annealing of SiC, however possible configurations of carbon at the interface in this heterostructure are not reported in literature.

Further research in this subject area should seek to clarify the magnesium terminated MgO/SiC interface structure. Atomic hydrogen processing of SiC surfaces could be sufficient to remove the silicate adlayer reconstruction providing a template for Mg-Si bonding at the interface. This would provide complete clarification of the difference in valence band offsets observed in the literature. Future research should also be directed towards measuring electrical properties of the SiC hetero-junctions for future device applications, such as those outlined in the introduction. Electrical characterisation of MOS capacitor structures from MgO/SiC hetero-junctions would be the first step to developing devices for this hetero-junction from successfully prepared samples.

Bibliography

[1] M. Bhatnagar and B. J. Baliga. Comparison of 6h-SiC, 3C-SiC, and Si for power devices. *IEEE Transactions on Electron Devices*, 40(3):645–655, 1993.

[2] H. Matsunami. Current SiC technology for power electronic devices beyond Si. *Microelectronic Engineering*, 83(1):2 – 4, 2006.

[3] M. H. Rashid. *Power electronics handbook*. Butterworth-Heinemann, 2017.

[4] H. Amano et al. The 2018 GaN power electronics roadmap. *Journal of Physics D: Applied Physics*, 51(16):163001, 2018.

[5] Y. Park, K. Kong, H. Chang, and M. Shin. Gate leakage current in double-gate MOSFETs with Si/SiO_2 interface model from first principle calculations. In *10th IEEE International Conference on Nanotechnology*, pages 1109–1112, 2010.

[6] Y. Yeo, T. King, and C. Hu. MOSFET gate leakage modeling and selection guide for alternative gate dielectrics based on leakage considerations. *IEEE Transactions on Electron Devices*, 50(4):1027–1035, 2003.

[7] J. Chen, W. Hsu, and C. Huang. Dielectric properties of magnesium oxide at microwave frequency. *Journal of Alloys and Compounds*, 504(1):284 – 287, 2010.

[8] S. S. P. Parkin, C. Kaiser, A. Panchula, P. M. Rice, B. Hughes, M. Samant, and S. Yang. Giant tunnelling magnetoresistance at room temperature with MgO (100) tunnel barriers. *Nature Materials*, 3:862–867, 2004.

[9] J. Mathon and A. Umerski. Theory of tunneling magnetoresistance of an epitaxial Fe/MgO/Fe (001) junction. *Physical Review B*, 63(22):220403, 2001.

[10] R. S. Ohl. Light-Sensitive Electric Device. U.S. patent 2402662, Filed on 27^{th} May 1941, Issued 25^{th} June 1946.

[11] Nobelprize.org. The Nobel Prize in Physics 1956. URL `http://www.nobelprize.org/nobel_prizes/physics/laureates/1956/`. accessed 06/06/2018.

[12] D. Kahng. Electric Field Controlled Semiconductor Device. U.S. patent 3102230, filed on 31^{st} May 1960, issued on 27^{th} August 1963.

[13] J. E. Lilienfeld. Method and apparatus for controlling electric currents. U.S. patent 1745175, Issued on 19^{th} July 1927.

[14] F. M. Wanlass. Low Stand-by Power Complementary Field Effect Circuitry. U.S. patent 3356858, filed on 18^th June 1963, issued on 5^{th} December 1967.

[15] X. Huang, W. Lee, C. Kuo, D. Hisamoto, L. Chang, J. Kedzierski, E. Anderson, H. Takeuchi, Y. Choi, K. Asano, V. Subramanian, T. King, J. Bokor, and C. Hu. Sub-50 nm p-channel finfet. *IEEE Transactions on Electron Devices*, 48(5):880–886, 2001.

[16] G. D. Wilk, R. M. Wallace, and J. M. Anthony. Hafnium and zirconium silicates for advanced gate dielectrics. *Journal of Applied Physics*, 87(1):484–492, 2000.

[17] A. Chatterjee, R. A. Chapman, K. Joyner, M. Otobe, S. Hattangady, M. Bevan, G. A. Brown, H. Yang, Q. He, and D. Rogers et al. Cmos metal replacement gate transistors using tantalum pentoxide gate insulator. In *Electron Devices Meeting, 1998. IEDM'98. Technical Digest., International*, pages 777–780. IEEE, 1998.

[18] J. Rabkowski, D. Peftitsis, and H. P. Nee. Silicon carbide power transistors: A new era in power electronics is initiated. *IEEE Industrial Electronics Magazine*, 6(2):17–26, 2012.

[19] Issa Batarseh. 4 - the power mosfet. In Muhammad H. Rashid, editor, *Power Electronics Handbook (Second Edition)*, pages 41 – 69. Academic Press, Burlington, second edition edition, 2007.

[20] A. Elasser and T. P. Chow. Silicon carbide benefits and advantages for power electronics circuits and systems. *Proceedings of the IEEE*, 90(6), 2002.

[21] W. J. Shatter, H. S. Kong, G. H. Negley, and J. W. Palmour. Carrier mobility model for simulation of SiC-based electronic devices. In *Institue of Physics Conference Series*, volume 137, page 155, 1994.

[22] Maciej Gutowski, John E Jaffe, Chun-Li Liu, Matt Stoker, Rama I Hegde, Raghaw S Rai, and Philip J Tobin. Thermodynamic stability of high-k dielectric metal oxides ZrO2 and HfO2 in contact with Si and SiO2. *Applied Physics Letters*, 80(11):1897–1899, 2002.

[23] EP Gusev, DA Buchanan, E Cartier, A Kumar, D DiMaria, S Guha, A Callegari, S Zafar, PC Jamison, DA Neumayer, et al. Ultrathin high-k gate stacks for advanced CMOS devices. In *Electron Devices Meeting, 2001. IEDM'01. Technical Digest. International*, pages 20–1. IEEE, 2001.

[24] T. Suzuki, Zhengang Zhang, A. K. Singh, Jinhua Yin, A. Perumal, and H. Osawa. High-density perpendicular magnetic recording media of granular-type (FePt/MgO)/soft underlayer. *IEEE Transactions on Magnetics*, 41(2):555–559, 2005.

[25] D. V. Dimitrov, Z. Gao, X. Wang, W. Jung, X. Lou, and O. Heinonen. Transport properties of MgO magnetic tunnel junctions. *Journal of Applied Physics*, 105(11):113905, 2009.

[26] B. D. Cullity and C. D. Graham. *Introduction to Magnetic Materials*. Wiley, 2011.

[27] P. J. Van Der Zaag, P. J. H. Bloemen, J. M. Gaines, R. M. Wolf, P. A. A. Van Der Heijden, R. J. M. Van de Veerdonk, and W. J. M. De Jonge. On the construction of an Fe3O4-based all-oxide spin valve. *Journal of magnetism and magnetic materials*, 211(1-3):301–308, 2000.

[28] S. Ikeda, J. Hayakawa, Y. Ashizawa, Y. M. Lee, K. Miura, H. Hasegawa, M. Tsunoda, F. Matsukura, and H. Ohno. Tunnel magnetoresistance of 604% at 300 k by suppression of ta diffusion in CoFeB/MgO/CoFeB pseudo-spin-valves annealed at high temperature. *Applied Physics Letters*, 93(8):082508, 2008.

[29] Y. M. Lee, J. Hayakawa, S. Ikeda, F. Matsukura, and H. Ohno. Effect of electrode composition on the tunnel magnetoresistance of pseudo-spin-valve magnetic tunnel junction with a MgO tunnel barrier. *Applied Physics Letters*, 90 (21):212507, 2007.

[30] R. Jansen. The spin-valve transistor: a review and outlook. *Journal of Physics D: Applied Physics*, 36(19):R289, 2003.

[31] C. J. Palmstrøm. Heusler compounds and spintronics. *Progress in Crystal Growth and Characterization of Materials*, 62(2):371–397, 2016.

[32] R. Jansen. Silicon spintronics. *Nature materials*, 11(5):400, 2012.

[33] T. Sasaki, T. Oikawa, T. Suzuki, M. Shiraishi, Y. Suzuki, and K. Noguchi. Temperature dependence of spin diffusion length in silicon by Hanle-type spin precession. *Applied Physics Letters*, 96(12):122101, 2010.

[34] C. Su, M. Frederick, M. Menghini, L. Dillemans, R. Lieten, T. Smets, J. W. Seo, and J. Locquet. Deposition and characterization of MgO/Si gate stacks grown by molecular beam epitaxy. *Thin Solid Films*, 520(14):4508 – 4511, 2012.

[35] R. O′Connor, G. Hughes, P. Casey, and S. B. Newcomb. Degradation and breakdown characteristics of thin MgO dielectric layers. *Journal of Applied Physics*, 107(2):024501, 2010.

[36] L. Kang, B. Lee, W. Qi, Y. Jeon, R. Nieh, S. Gopalan, K. Onishi, and J. Lee. Electrical characteristics of highly reliable ultrathin hafnium oxide gate dielectric. *Electron Device Letters, IEEE*, 21:181 – 183, 2000.

[37] J.H. Lim, N. Raghavan, S. Mei, K.H. Lee, S.M. Noh, J.H. Kwon, E. Quek, and K.L. Pey. Asymmetric dielectric breakdown behavior in MgO based magnetic tunnel junctions. *Microelectronic Engineering*, 178:308–312, 2017.

[38] K. Nagashima, T. Yanagida, H. Tanaka, and T. Kawai. Epitaxial growth of MgO nanowires by pulsed laser deposition. *Journal of Applied Physics*, 101, 2007.

[39] A. Marcu, T. Yanagida, K. Nagashima, H. Tanaka, and T. Kawai. Effect of ablated particle flux on MgO nanowire growth by pulsed laser deposition. *Journal of Applied Physics*, 102:016102, 2007.

[40] K. Matsuzaki, H. Hosono, and T. Susaki. Layer-by-layer epitaxial growth of polar MgO(111) thin films. *Physical Review B*, 82:033408, 2010.

[41] H. S. Craft, R. Collazo, M. D. Losego, S. Mita, Z. Sitar, and J. P. Maria. Band offsets and growth mode of molecular beam epitaxy grown MgO(111) on GaN(0002) by x-ray photoelectron spectroscopy. *Journal of Applied Physics*, 102(7):074104, 2007.

[42] N. Khalid, J.-Y. Kim, A. Ionescu, T. Hussain, F. Oehler, T. Zhu, R. A. Oliver, I. Farrer, R. Ahmad, and C. H. W. Barnes. Structure and magnetic properties of an epitaxial Fe(110)/MgO(111)/GaN(0001) heterostructure. *Journal of Applied Physics*, 123(10):103901, 2018.

[43] B.P. Gila, J. Kim, B. Luo, A. Onstine, W. Johnson, F. Ren, C.R. Abernathy, and S.J. Pearton. Advantages and limitations of MgO as a dielectric for GaN. *Solid-State Electronics*, 47(12):2139 – 2142, 2003. Proceedings of the 9th International Workshop on Oxide Electronics.

[44] P. W. Tasker. The stability of ionic crystal surfaces. *Journal of Physics C: Solid State Physics*, 12(22):4977, 1979.

[45] J. Goniakowksi, F. Finocchi, and C. Noguera. Polarity of oxide surfaces and nanostructures. *Reports on Progress in Physics*, 71:016501, 2008.

[46] J. Goniakowski, C. Noguera, and L. Giordano. Using Polarity for Engineering Oxide Nanostructures: Structural Phase Diagram in Free and Supported MgO(111) Ultrathin Films. *Physical Review Letters*, 93:215702, 2004.

[47] C. Noguera and J. Goniakowski. Polarity in Oxide Nano-objects. *Chemical Reviews*, 113(6):4073–4105, 2013.

[48] C. Noguera. Polar oxide surfaces. *Journal of Physics: Condensed Matter*, 12 (31):R367, 2000.

[49] J. Goniakowski and C. Noguera. Characteristics of Pd deposition on the MgO(111) surface. *Physical Review B*, 60:16120–16128, 1999.

[50] J. Goniakowski and C. Noguera. Polarization and rumpling in oxide monolayers deposited on metallic substrates. *Phys Rev. B*, 79:155433, 2009.

[51] D. P. Woodruff and T. A. Delchar. *Modern techniques of surface science, 2nd edition.* Cambridge University Press, Cambridge UK, 1994.

[52] D. Cappus, M. Hael, E. Neuhaus, M. Heber, F. Rohr, and H.-J. Freund. Polar surfaces of oxides: reactivity and reconstruction. *Surface Science*, 337(3):268 – 277, 1995.

[53] A. Barbier and G. Renaud. Structural investigation of the NiO(111) single crystal surface. *Surface Science*, 392(1):L15 – L20, 1997.

[54] N. Erdman, O. Warschkow, D. E. Ellis, and L. D. Marks. Solution of the $p(2\times2)NiO(111)surfacestructureusingdirectmethods$. *Surface Science*, 470 : $1 - -14, 2000$.

[55] S. Wang, S. Liu, J. Guo, K. Wu, and Q. Guo. Surface electronic structure of polar NiO(111) films. *Surface Science*, 606(3):378 – 382, 2012.

[56] F. Rohr, K. Wirth, J. Libuda, D. Cappus, M. Bumer, and H.-J. Freund.

[57] V. K. Lazarov, R. Plass, H-C. Poon, D. K. Saldin, M. Weinert, S. A. Chambers, and M. Gajdardziska-Josifovska. Structure of the hydrogen-stabilized MgO(111)$-(1\times1)$ polar surface: Integrated experimental and theoretical studies. *Physical Review B*, 71:115434, 2005.

[58] Z. L. Wang. Zinc oxide nanostructures: growth, properties and applications. *Journal of Physics: Condensed Matter*, 16(25):R829, 2004.

[59] S. Benedetti, N. Nilius, P. Torelli, G. Renaud, H.-J. Freund, and S. Valeri. Competition between Polar and Nonpolar Growth of MgO Thin Films on Au(111). *The Journal of Physical Chemistry C*, 115(46):23043–23049, 2011.

[60] K. Refson, R. A. Wogelius, D. G. Fraser, M. C. Payne, M. H. Lee, and V. Milman. Water chemisorption and reconstruction of the MgO surface. *Physical Review B*, 52:10823–10826, 1995.

[61] M. Kiguchi, S. Entani, K. Saiki, T. Goto, and A. Koma. Atomic and electronic structure of an unreconstructed polar Mgo(111) thin film on Ag(111). *Physical Review B*, 68:115402, 2003.

[62] R. Arita, Y. Tanida, S. Entani, M. Kiguchi, M. Saiki, and H. Aoki. Polar surface engineering in ultrathin MgO(111)Ag(111): Possibility of a metal-insulator transition and magnetism. *Physical Review B*, 69:235423, 2004.

[63] M. Xue and Q. Guo. Layer-by-layer growth of polar MgO(111) ultrathin films. *The Journal of Chemical Physics*, 127(5):054705, 2007.

[64] J. C. Costa et al. Barrier height variation in Al/GaAs Schottky diodes with a thin silicon interfacial layer. *Applied Physics Letters*, 58(4):382–384, 1991.

[65] S. N. Das, J. H. Choi, J. P. Kar, K. Moon, T. I. Lee, and J. M. Myoung. Junction properties of Au/ZnO single nanowire schottky diode. *Applied Physics Letters*, 96(9):092111, 2010.

[66] M. J. Mondry and H. Kroemer. Heterojunction bipolar transistor using a (Ga, In) P emitter on a GaAs base, grown by molecular beam epitaxy. *IEEE electron device letters*, 6(4):175–177, 1985.

[67] J. D. Cressler and G. Niu. *Silicon-Germanium heterojunction bipolar transistors*. Artech house, 2003.

[68] Y. Yeo, T. King, and C. Hu. Metal-dielectric band alignment and its implications for metal gate complementary metal-oxide-semiconductor technology. *Journal of applied physics*, 92(12):7266–7271, 2002.

[69] S. Oktyabrsky and D. Y. Peide. *Fundamentals of III-V semiconductor MOSFETs*. Springer, 2010.

[70] Hans Lüth. *Solid surfaces, interfaces and thin films*, volume 4. Springer, 2001.

[71] R. L. Anderson. Germanium-gallium arsenide heterojunctions. *IBM Journal of Research and Development*, 4:283–287, 1960.

[72] J. O. McCaldin, T. C. McGill, and C. A. Mead. Correlation for III-V and II-VI Semiconductors of the Au Schottky Barrier Energy with Anion Electronegativity. *Physical Review Letters*, 36:56–58, 1976.

[73] S. P. Kowalczyk., J. T. Cheung., A. E. Kraut, and R. W. Grant. CdTe-HgTe (111) Heterojunction Valence-Band Discontinuity: A Common-Anion-Rule Contradiction. *Physical Review Letters*, 56:1605–1608, 1986.

[74] W. A Harrison. *Electronic structure and the properties of solids: the physics of the chemical bond*. Courier Corporation, 2012.

[75] P. Vogl, H. P. Hjalmarson, and J. D. Dow. A semi-empirical tight-binding theory of the electronic structure of semiconductors? *Journal of physics and chemistry of solids*, 44(5):365–378, 1983.

[76] S. H. Wei and A. Zunger. Calculated natural band offsets of all IIVI and IIIV semiconductors: Chemical trends and the role of cation d orbitals. *Applied Physics Letters*, 72(16):2011, 1998.

[77] A. Klein. Energy band alignment at interfaces of semiconducting oxides: A review of experimental determination using photoelectron spectroscopy and comparison with theoretical predictions by the electron affinity rule, charge neutrality levels, and the common anion rule. *Thin Solid Films*, 520(10):3721 – 3728, 2012. 7th International Symposium on Transparent Oxide Thin Films for Electronics and Optics (TOEO-7).

[78] A. Franciosi and C. G. Van de Walle. Heterojunction band offset engineering. *Surface Science Reports*, 25(1):1 – 140, 1996.

[79] V. Heine. Theory of surface states. *Phys. Rev.*, 138:A1689–A1696, 1965.

[80] S. G. Louie, J. R. Chelikowsky, and M. L. Cohen. Ionicity and the theory of Schottky barriers. *Physical Review B*, 15:2154–2162, 1977.

[81] W. Hu and J. Yang. Two-dimensional van der Waals heterojunctions for functional materials and devices. *Journal of Materials Chemistry C*, 5:12289–12297, 2017.

[82] W. Umrath et al. *Fundamentals of Vacuum Technology.* Oerlikon Leybold Vacuum, Cologne, 2007.

[83] A. Chambers. *Basic vacuum technology.* CRC Press, 1998.

[84] R. M. Zabel and A. Elleth. The Pirani Gauge for the Measurement of Small Changes of Pressure. *Phys. Rev.*, 37:1102–1111, 1931.

[85] Oxford Applied Research. RF Atom Sources. URL `http://www.oaresearch.co.uk/oaresearch/brochures/HDSeries.pdf`. accessed 28/04/2018.

[86] G. G. Lister. Low-pressure gas discharge modelling. *J. Phys. D: Appl. Phys.*, 25:1649–1680, 1992.

[87] M. Ohring. *Materials Science of Thin Films (Second Edition)*. Academic Press, San Diego, 2002.

[88] K. Takayanagi and Y. Tanishiro. Dimer-chain model for the 7x7 and the 2x8 reconstructed surfaces of reconstructed surfaces of Si(111) and Ge(111). *Physical Review B*, 34:1034–1040, 1986.

[89] A. I. Ichimiya and P. Cohen. Reflection High-Energy Electron Diffraction. 2004.

[90] L. de Broglie. Recherches sur la Theorie des Quanta (Research on the Quantum Theory). *Ann. Phys.*, 3:22–128, 1925.

[91] F. Jona, J. A. Strozier Jr, and W. S. Yang. Low-energy electron diffraction for surface structure analysis. *Rep. Prog. Phys.*, 45:527, 1982.

[92] T.L. Goodrich, Z. Cai, and K.S. Ziemer. Stability of MgO(111) films grown on 6H-SiC(0001) by molecular beam epitaxy for two-step integration of functional oxides. *Applied Surface Science*, 254(10):3191 – 3199, 2008.

[93] D. Briggs and M. P. Seah. *Practical Surface Analysis, Auger and X-ray Photoelectron Spectroscopy*. Wiley, University of Michigan, USA, 1990.

[94] NIST X-ray Photoelectron Spectroscopy (XPS) Database, Version 3.5. `https://srdata.nist.gov/xps/main_search_menu.aspx`. accessed 27/05/2018.

[95] J. F. Watts and J. Wolstenholme. *An Introduction to Surface Analysis by XPS and AES*. TJ International Ltd, Padstow, Cornwall, 2003.

[96] E. A. Kraut, R. W. Grant, J. R. Waldrop, and S. P. Kowalczyk. Semiconductor core-level to valence-band maximum binding-energy differences: Precise determination by x-ray photoelectron spectroscopy. *Physical Review B*, 28: 1965–1977, 1983.

[97] V. V. Afanas'ev. Electron band alignment at interfaces of semiconductors with insulating oxides: an internal photoemission study. *Advances in Condensed Matter Physics*, 2014, 2014.

[98] P. F. Zhang, X. L. Liu, R. Q. Zhang, H. B. Fan, H. P. Song, H. Y. Wei, C. M. Jiao, S. Y. Yang, Q. S. Zhu, and Z. G. Wang. Valence band offset of MgoInN heterojunction measured by x-ray photoelectron spectroscopy. *Applied Physics Letters*, 92(4):042906, 2008.

[99] A. L. Yang, H. P. Song, X. L. Liu, H. Y. Wei, Y. Guo, G. L. Zheng, C. M. Jiao, S. Y. Yang, Q. S. Zhu, and Z. G. Wang. Determination of MgO/AlN heterojunction band offsets by x-ray photoelectron spectroscopy. *Applied Physics Letters*, 94(5):052101, 2009.

[100] W. Mönch. *Semiconductor Surfaces and Interfaces.* Springer-Verlag Berlin Heidelberg, Berlin, 2001.

[101] M. W. Wang, J. F. Swenberg, M. C. Phillips, E. T. Yu, J. 0. McCaldin, R. W. Grant, and T. C. McGill. X-ray photoelectron spectroscopy measurement of valence-band offsets for Mg-based semiconductor compounds. *Applied Physics Letters*, 61:3455–3457, 1994.

[102] L. Lari, S. Lea, C. Feeser, B. W. Wessels, and V. K. Lazarov. Ferromagnetic InMnSb multi-phase films study by aberration-corrected (scanning) transmission electron microscopy. *Journal of Applied Physics*, 111(7):07C311, 2012.

[103] J. Li, T. Malis, and S. Dionne. Recent advances in FIBTEM specimen preparation techniques. *Materials Characterization*, 57:64 – 70, 2006.

[104] L.A. Giannuzzi and F.A. Stevie. A review of focused ion beam milling techniques for TEM specimen preparation. *Micron*, 30(3):197 – 204, 1999.

[105] D. B. Williams and B. C. Carter. *Transmission Electron Microscopy.* Springer Science and Business Media, LLC, 233 Spring Street, New York, NY 10013, USA.

[106] S. J. Pennycook and L. A. Boatner. Chemically sensitive structure-imaging with a scanning transmission electron microscope. *Nature*, 336(6199):565, 1988.

[107] J. M. LeBeau, S. D. Findlay, L. J. Allen, and S. Stemmer. Quantitative Atomic Resolution Scanning Transmission Electron Microscopy. *Physical Review Letters*, 100:206101, 2008.

[108] C. T. Koch. Determination of core structure periodicity and point defect density along dislocations, 2002. PhD Thesis, Arizona State University.

[109] P. Hohenberg and W. Kohn. Inhomogeneous Electron Gas. *Phys. Rev.*, 136: B864–B871, 1964.

[110] O. Gunnarsson and B. Lundqvist. Exchange and correlation in atoms, molecules, and solids by the spin-density-functional formalism. *Phys. Rev. B*, 13: 4274–4298, 1976.

[111] J. P. Perdew, K. Burke, and M. Ernzerhof. Generalized gradient approximation made simple. *Physical review letters*, 77(18):3865, 1996.

[112] Richard M Martin. *Electronic structure: basic theory and practical methods*. Cambridge University Press, 2004.

[113] M. C. Payne, M. P. Teter, D. C. Allan, T. A. Arias, and J. D. Joannopoulos. Iterative minimization techniques for ab initio total-energy calculations: molecular dynamics and conjugate gradients. *Reviews of modern physics*, 64(4): 1045, 1992.

[114] CASTEP. URL `http://www.castep.org`.

[115] S. Blügel and G. Bihlmayer. Full-Potential Linearized Augmented Planewave Method. *NIC Series*, 31:85–129, 2006.

[116] M. Weinert. Solution of Poisson's equation: Beyond Ewald-type methods. *Journal of Mathematical Physics*, 22(11):2433–2439, 1981.

[117] M. Weinert, E. Wimmer, and A. J. Freeman. Total-energy all-electron density functional method for bulk solids and surfaces. *Physical Review B*, 26(8):4571, 1982.

[118] M. Weinert, G. Schneider, R. Podloucky, and J. Redinger. Flapw: applications and implementations. *Journal of Physics: Condensed Matter*, 21(8):084201, 2009. URL `http://www.uwm.edu/ weinert/flair.html`.

[119] E. Wimmer, H. Krakauer, M. Weinert, and A. J. Freeman. Full-potential self-consistent linearized-augmented-plane-wave method for calculating the electronic structure of molecules and surfaces: o_2 molecule. *Physical Review B*, 24(2):864, 1981.

[120] T. Fujino, T. Fuse, J. T. Ryu, K. Inudzuka, Y. Yamazaki, M. Katayama, and K. Oura. Structural Analysis of 6H–SiC (0001) 3× 3 Reconstructed Surface. *Japanese Journal of Applied Physics*, 39(11R):6410, 2000.

[121] J. E. Northrup and J. Neugebauer. Theory of the adatom-induced reconstruction of the SiC (0001) $\sqrt{3} \times \sqrt{3}$ surface. *Physical Review B*, 52(24):R17001, 1995.

[122] L. Li and I. S. T. Tsong. Atomic structures of 6h-sic (0001) and (000$\bar{1}$) surfaces. *Surface science*, 351(1-3):141–148, 1996.

[123] W. Lu, P. Krüger, and J. Pollmann. Atomic and electronic structure of silicate adlayers on polar hexagonal SiC surfaces. *Physical Review B*, 61(20):13737, 2000.

[124] N. Sieber, M. Hollering, J. Ristein, and L. Ley. Photoemission study of the silicate adlayer reconstruction on Si-terminated 6H-SiC (0001). *Materials Science Forum*, 338:391–394, 2000.

[125] J. Bernhardt, J. Schardt, U. Starke, and K. Heinz. Epitaxially ideal oxidesemiconductor interfaces: Silicate adlayers on hexagonal (0001) and (000$\bar{1}$)) SiC surfaces. *Applied Physics Letters*, 74(8):1084–1086, 1999.

[126] D. M. Knotter. Etching mechanism of vitreous silicon dioxide in hf-based solutions. *Journal of the American Chemical Society*, 122(18):4345–4351, 2000.

[127] U. Starke and C. Riedl. Epitaxial graphene on sic (0001) and: from surface reconstructions to carbon electronics. *Journal of Physics: Condensed Matter*, 21(13):134016, 2009.

[128] V. Ramachandran, M. F. Brady, A. R. Smith, R. M. Feenstra, and D. W. Greve. Preparation of atomically flat surfaces on silicon carbide using hydrogen etching. *Journal of Electronic Materials*, 27(4):308–312, 1998.

[129] A. Sagar, C. D. Lee, R. M. Feenstra, C. K. Inoki, and T. S. Kuan. Morphology and effects of hydrogen etching of porous SiC. *Journal of Applied Physics*, 92 (7):4070–4074, 2002.

[130] T. L. Chu and R. B. Campbell. Chemical etching of silicon carbide with hydrogen. *Journal of the Electrochemical Society*, 112(9):955–956, 1965.

[131] C. D. Lee, R. M. Feenstra, O. Shigiltchoff, R. P. Devaty, and W. J. Choyke. Structural properties of gan films grown by molecular beam epitaxy on singular and vicinal 6h-sic (0001). *Materials Research Society Internet Journal of Nitride Semiconductor Research*, 7, 2002.

[132] D. Sander et al. Preferential carbon etching by hydrogen inside hexagonal voids of 6H-SiC (0001). *Applied Physics Letters*, 81(19):3570–3572, 2002.

[133] K. G. Tschersich. Intensity of a source of atomic hydrogen based on a hot capillary. *Journal of Applied Physics*, 87(5):2565–2573, 2000.

[134] N. H. Golshan. Understanding electrically active interface formation on wide bandgap semiconductors through molecular beam epitaxy using fe_3o_4 for spintronics as a base case, 2014. URL `https://repository.library.northeastern.edu/files/neu:cj82r5126/fulltext.pdf`. PhD Thesis accessed from Northeastern University Digital Repository Service.

[135] D. Gilks, L. Lari, K. Matsuzaki, H. Hosono, T. Susaki, and V. K. Lazarov. Structural study of Fe3O4(111) thin films with bulk like magnetic and magnetotransport behaviour. *Journal of Applied Physics*, 115(17):17C107, 2014.

[136] K. Matsuzaki, V. K. Lazarov, L. Lari, H. Hosono, and T. Susaki. Fe3o4 (111) thin films with bulk-like properties: growth and atomic characterization. *Journal of Physics D: Applied Physics*, 46(2):022001, 2012.

[137] T. Susaki, S. Kumada, T. Katase, K. Matsuzaki, M. Miyakawa, and H. Hosono. Fabrication of flat mgo (111) films on al2o3 (0001) substrates by pulsed laser deposition. *Applied Physics Express*, 2(9):091403, 2009.

[138] Trevor L Goodrich, J Parisi, Zhuhua Cai, and Katherine S Ziemer. Low temperature growth of crystalline magnesium oxide on hexagonal silicon carbide (0001) by molecular beam epitaxy. *Applied physics letters*, 90(4):042910, 2007.

[139] Z. Cai, T. L. Goodrich, B. Sun, Z. Chen, VG Harris, and K. S. Ziemer. Epitaxial growth of barium hexaferrite film on wide bandgap semiconductor 6H-SiC by molecular beam epitaxy. *Journal of Physics D: Applied Physics*, 43(9):095002, 2010.

[140] A Posadas, FJ Walker, CH Ahn, TL Goodrich, Z Cai, and KS Ziemer. Epitaxial mgo as an alternative gate dielectric for sic transistor applications. *Applied Physics Letters*, 92(23):233511, 2008.

[141] Zhoahui Chen, Aria Yang, SD Yoon, Katherine Ziemer, Carmine Vittoria, and VG Harris. Growth of ba-hexaferrite films on single crystal 6-h sic. *Journal of magnetism and magnetic materials*, 301(1):166–170, 2006.

[142] V. K. Lazarov, Z. Cai, K. Yoshida, H. H. L. Zhang, M. Weinert, K. S. Ziemer, and P. J. Hasnip. Dynamically stabilized growth of polar oxides: the case of MgO (111). *Physical Review Letters*, 107(5):056101, 2011.

[143] D. T. Clark et al. High temperature silicon carbide cmos integrated circuits. In *Materials Science Forum*, volume 679, pages 726–729, 2011.

[144] C. E. Weitzel, J. W. Palmour, C. H. Carter, K. Moore, K. K. Nordquist, S. Allen, C. Thero, and M. Bhatnagar. Silicon carbide high-power devices. *IEEE Transactions on Electron Devices*, 43(10):1732–1741, 1996.

[145] A. I. Kingon, J. P. Maria, and S. K. Streiffer. Alternative dielectrics to silicon dioxide for memory and logic devices. *Nature*, 406(6799):1032, 2000.

[146] B. Brennan, S. McDonnell, and G. Hughes. Photoemission studies of the interface formation of ultrathin MgO dielectric layers on the oxidised Si (111) surface. In *Journal of Physics: Conference Series*, volume 100, page 042047, 2008.

[147] A. Tsukazaki, A. Ohtomo, T. Kita, Y. Ohno, H. Ohno, and M. Kawasaki. Quantum Hall Effect in Polar Oxide Heterostructures. *Science*, 315(5817):1388–1391, 2007.

[148] A. A. Baker, A. I. Figueroa, D. Pingstone, V. K. Lazarov, G. Van Der Laan, and T. Hesjedal. Spin pumping in magnetic trilayer structures with an MgO barrier. *Scientific Reports*, 6:35582, 2016.

[149] S. Yuasa, T. Nagahama, A. Fukushima, Y. Suzuki, and K. Ando. Giant room-temperature magnetoresistance in single-crystal Fe/MgO/Fe magnetic tunnel junctions. *Nature Materials*, 3(12):868, 2004.

[150] C. Noguera and J. Goniakowski. Polarity in oxide ultrathin films. *Journal of Physics: Condensed Matter*, 20(26):264003, 2008.

[151] N. C. Bristowe, P. B. Littlewood, and E. Artacho. Surface defects and conduction in polar oxide heterostructures. *Physical Review B*, 83(20):205405, 2011.

[152] B. L. Zhang, F. F. Cai, G. S. Sun, H. B. Fan, P. F. Zhang, H. Y. Wei, X. L. Liu, S. Y. Yang, Q. S. Zhu, and Z. G. Wang. Valence band offset of MgO/4H-SiC heterojunction measured by x-ray photoelectron spectroscopy. *Applied Physics Letters*, 93(7):072110, 2008.

[153] T. L. Goodrich. Atomistic investigation into the interface engineering and heteroepitaxy of functional oxides on hexagonal silicon carbide through the use of a magnesium oxide template layer for the development of a multifunctional heterostructure, 2008. URL `http://hdl.handle.net/2047/d10017239`. PhD Thesis accessed from Northeastern University Digital Repository Service.

[154] S. J. Clark, M. D. Segall, C. J. Pickard, P. J. Hasnip, M. I. J. Probert, K. Refson, and M. C. Payne. First principles methods using CASTEP. *Zeitschrift für Kristallographie-Crystalline Materials*, 220(5/6):567–570, 2005.